

Resilient Hybrid Steel-Timber Structural Systems for Seismic Applications

by

Ahmed Gamal Abdelnaser Mohamed Mowafy Saad

A thesis submitted in partial fulfillment of the requirements for the degree of

Doctor of Philosophy

in

Structural Engineering

Department of Civil and Environmental Engineering
University of Alberta

© Ahmed Gamal Abdelnaser Mohamed Mowafy Saad, 2023

Abstract

The Black Swan events of the 1994 Northridge and the 2010-2011 Christchurch earthquakes brought seismic design philosophy under scrutiny, emphasizing need for resilient structure that prioritize life safety and facilitate rapid post-earthquake recovery with minimal repair costs. Hybrid steel-timber structures offer resilient option and improved structural performance by combining steel's ductility with timber's lightness. This thesis presents a practical guideline to design a resilient hybrid steel-timber rocking braced frame. To achieve this, a novel connection system featuring U-shaped steel seismic fuses was developed to connect between a gravity load-resisting timber frame and a steel concentrically braced frame acting as the lateral load-resisting system with self-centring capability.

This research study comprises three interconnected components that utilize extensive experimental testing, numerical modelling, and design optimization methods. The first component introduces a novel U-shaped steel seismic fuse employing a unique scissor-bending mechanism. Comprehensive experimental and numerical analyses highlight its potential for diverse applications, offering notable strength, stiffness, ductility, and energy dissipation capacity. The second component explores an innovative hybrid timber beam-to-steel column connection system, incorporating the proposed U-shaped steel seismic fuses. Comprehensive testing led to significant improvements in the initial joint design, yielding a connection system that demonstrated enhanced cyclic load resistance and stable load-displacement cycles, facilitating rapid post-earthquake recovery. Building on these results, the third component introduces a new low-damage, self-centring hybrid steel-timber rocking braced frame. The proposed design methodology was

validated through in-depth numerical analyses, demonstrating the system's desired seismic performance with minimal post-earthquake residual deformations.

This research has generated significant advances in understanding of the seismic resilience of hybrid steel-timber structures. The findings revealed that the U-shaped steel seismic fuse can safely dissipate seismic loads through a scissor bending mechanism. Further, an innovative hybrid timber beam-to-steel column connection system demonstrated improved ductile behaviour and no strength degradation in glulam beam member, opening the door to more retrofitting options. In addition, replaceable fuses, validated in the study, offer opportunities for flexible and effective structural upgrades post-earthquake. The novel hybrid steel-timber rocking braced frame effectively resisted seismic-induced demands, demonstrating self-centring capabilities, and staying within the code-specified drift limit. Significantly, the system remained elastic under design-level hazards, proving its resilience. These collective findings found practical application in the design of a five-storey prototype building, where a self-centring, chevron-type steel frame served as an effective lateral load-resisting system.

This body of work substantially contributes to seismic design standards and promotes the broader use of timber in hybrid steel-timber structures.

Preface

This thesis, an original work by Ahmed Mowafy, has been conducted under the guidance of Dr. Ali Imanpour and Dr. Ying Hei Chui. It forms part of a collaborative research project between the Advanced Research in Building Systems (ARTS) and the Steel Centre at the University of Alberta. The thesis is formatted in a paper style and comprises six chapters:

Chapter 1 provides an introduction, covering the background and motivation for the study. It outlines the research objectives and scope, describes the methodology employed, and outlines the thesis structure.

Chapter 2 presents a comprehensive literature review, focusing on hybrid steel-timber structures and the need for resilience in seismic design as informed by lessons from past earthquakes. It provides a deep dive into connection and fuse mechanisms in hybrid structures, explores self-centring systems, and offers a detailed review of the potential of wood in this context. This chapter concludes by identifying research gaps and potential contributions.

Chapters 3 to 6 form the core of this thesis:

Chapter 3 is currently being prepared as a journal manuscript.

Chapter 4 is currently being prepared as a journal manuscript.

Chapter 5 has been submitted as a journal manuscript: under review. Mowafy A, Imanpour A, Chui YH. A New Hybrid Steel-Timber Rocking Seismic Force Resisting System Equipped with U-shaped Fuse Connections. [Manuscript submitted for publication]. CJCE 2023 – Mass Timber special issue.

Chapter 6 concludes the thesis, summarizing the main contributions and emphasizing the importance of this research for rapid recovery and repair after seismic events. It also provides recommendations for further research and development of new connection types and calls for validating design guidelines in real-world applications.

Throughout the research, I was responsible for the experimental program, data analysis, computational modelling, and manuscript composition. Drs. Ali Imanpour and Ying Hei Chui contributed significantly to concept formation, data analysis, and manuscript composition. Dr. Hossein Daneshvar aided in manuscript edits for Chapters 3 and 4, and Dr. Abolfazl Ashrafi provided valuable ground motion data utilized in Chapter 5.

I also contributed to the following publications:

- ✓ Mowafy, A., Imanpour, A., & Chui, Y.H. (2021). Evaluation of the Seismic Response of an Innovative Hybrid Steel-Timber Structure. *Ce/Papers*, 4(2–4), 1864–1873. <https://doi.org/10.1002/cepa.1497>
- ✓ Mowafy, A., Imanpour, A., Chui, Y.H., & Daneshvar, H. (2023). Experimental investigation of an innovative beam-to-column connection under cyclic loading. In *WCTE 2023* (pp. 3127-3133). Oslo. <https://doi.org/10.52202/069179-0407>.

Dedication

First and foremost, I am deeply grateful to God for always being by my side. His unwavering guidance has always led me toward good deeds and accomplishments.

To my mother, Amany Hamza, whose discerning eyes recognized my early childhood affinity for Math and Geometry. She taught me the importance of understanding the roots of problems, a lesson I carry with me today.

My father, Gamal Mowafy, a beacon of support, instilled in me the values of professional ethics and decision-making. He gifted me the freedom to choose my career and has always stood by my choices.

My spouse, Aisha Elgarhy, and our child, Fares, deserve special thanks. Aisha has been a pillar of support, accompanying me through the highs and lows of my career and weathering challenges alongside me during my graduate studies.

To my siblings, Ashraf, Ibrahim, and Alyaa. Ashraf's accomplishments as a young project manager in civil engineering, leading several national projects in Aldabaa, inspire me greatly.

My gratitude extends to my relatives, who consistently provided encouragement and guidance. My Uncle Hany Honora, a civil engineer, has been a great source of inspiration in my industry work. My Uncle Prof. Alim Hanoura, through his successful contributions to academia and the field of hydraulic engineering, has always inspired me.

My Uncles, Ahmed, Ashraf, and Nagy have been my guiding lights in professional ethics and successful business practice. My Uncle Ali Hanoura, for his bravery and dedication in defending his homeland, inspired me with his courage.

To my mentors: Dr. Ahmed Shamel, my MSc supervisor who guided me in academia; Prof. Abdelaziz Mahmoud, who bridged the gap between theory and industry for me; and Dr. Maysara Eltahan, my partner at the CMC Consultant office, who believed in my strengths and encouraged me to pursue my Ph.D.

To my friends: Mohamed Essam, a companion since childhood who has consistently guided and encouraged me through difficult times. Ahmed Hussein's support and experience in Ph.D. and academic writing have been invaluable.

Finally, I dedicate this work to the memory of my grandparents, Mohammed Mowafy and Hamza Hanoura, and grandmothers Aziza Elattar and Rizka Mowafy. They found immense joy and pride in my accomplishments. My grandfather Hamza's proud welcome when I was admitted to the Faculty of Engineering will forever remain in my heart, guiding me through hardships. Their spirits continue to inspire and drive me toward success.

Their love, support, and wisdom have been my beacon, illuminating the path that led to the completion of this journey. I am forever grateful.

Acknowledgements

This journey, though taken in solitude, was hardly a solo expedition. I am fortunate and humbled by the many individuals and organizations who contributed to this thesis in many capacities.

Funding was provided by the Natural Sciences and Engineering Research Council (NSERC) of Canada, via the Industrial Research Chair and the Discovery Grant Programs, and the industrial partners of ARTS and Steel Centre. Financial support was also received from the Canadian Institute of Steel Construction through the 2021 Kulak. These financial contributions are gratefully acknowledged.

Special thanks are due to PAALID ENG, Western Archrib, Alberta Innovates, and C-FER Technologies for material provision, specimen preparation, and testing facilities. I extend my gratitude to Dr. Hossein Danshaver for their support in lab work, and to Dr. Jan Niederwestberg for his help in reviewing the connection design. Dr. Abolfazl Ashrafi's contribution to ground motion data was particularly invaluable.

I owe profound thanks to my supervisors, Dr. Ali Imanpour and Dr. Ying Hei Chui, for their unwavering support and mentorship. Their trust in my abilities has been greatly empowering, even when pushing boundaries with novel concepts. Their belief in me and support, even when my ideas ventured into uncharted territories, has been a source of strength and inspiration.

Table of Contents

Abstract..... ii

Preface..... iv

Dedication vi

Acknowledgements viii

List of Tables xiii

List of Figures..... xiv

1. Introduction..... 1

 1.1. Background and motivation 1

 1.2. Research scope and objectives 2

 1.3. Methodology 4

 1.4. Thesis outline 5

2. Literature review 9

 2.1. Needs for resilience in seismic design: Lessons from past earthquakes 11

 2.2. Self-centring systems 13

 2.3. Connection development in mass timber 15

 2.4. Structural fuses and dampers in seismic resilience 17

 2.5. U-shaped steel plates as seismic fuses 19

 2.6. Research gaps and contributions of this study 20

3. Cyclic Behaviour and Plastic Mechanism of a U-shaped Steel Seismic Fuse.....	22
3.1.Introduction.....	22
3.2.U-shape steel plate mechanism.....	23
3.3.Test specimens and setup.....	26
3.3.1 Test specimens.....	26
3.3.2 Test setup and instrumentation.....	27
3.3.3 Loading procedures.....	28
3.4.Experimental results.....	29
3.4.1 Hysteresis response.....	29
3.4.2 Plastic mechanism.....	30
3.4.3 Stiffness degradation and ductility.....	32
3.4.4 Energy dissipation capacity.....	33
3.5.Numerical modelling of USP plastic mechanism.....	34
3.5.1 Finite element model.....	34
3.5.2 Model validation.....	35
3.5.3 USP yielding capacity and stiffness.....	37
3.6.Summary and conclusion.....	38
Notation.....	40
4. Development and cyclic testing of a hybrid timber-steel beam-to-column connection with replaceable U-shaped fuses *	61
4.1.Introduction.....	61
4.2.Proposed Connection.....	62
4.2.1 Connection Components.....	62

4.2.2	Design Philosophy	64
4.2.3	Yielding and probable capacities	64
4.2.4	Moment capacity.....	65
4.2.5	Potential Applications in Seismic Design	69
4.3.	Experimental Program	69
4.3.1	Test Matrix.....	70
4.3.2	Specimens	70
4.3.3	Test Setup.....	71
4.3.4	Loading Scheme.....	72
4.4.	Experimental results.....	73
4.4.1	Hysteresis response.....	74
4.4.2	Failure Modes	75
4.4.3	Connection performance characteristics	77
4.4.4	Energy dissipation capacity	78
4.4.5	Evaluation of moment capacity prediction	79
4.5.	Conclusions.....	79
	Notation	82
5.An Innovative Hybrid Steel-Timber Rocking Seismic Force Resisting System Equipped with U-shaped Fuse Connections*		109
5.1.	Introduction.....	109
5.2.	Proposed hybrid steel-timber rocking braced frame	111
5.2.1	System components.....	111
5.2.2	Design methodology and performance objectives	112
5.3.	Prototype building design	116

5.3.1	Geometry and seismic design parameters	116
5.3.2	Seismic design of prototype STRBF	118
5.4.	Verification of the design method.....	125
5.4.1	Numerical model development	125
5.4.2	Seismic response of STRBF	127
5.5.	Limitations	131
5.6.	Conclusions.....	131
	Notation	133
6.	Conclusions and recommendations	145
6.1.	Conclusions.....	145
6.2.	Recommendations for future work	148
	Bibliography	151
	Appendices.....	169
	Appendix A – Coupon Test	170
	Appendix B – U-shaped Fuses Bending Process	172
	Appendix C – Self Drilling Dowels Installation.....	173
	Appendix D – Structural Drawings of The Glulam Beam Specimens.....	175

List of Tables

Table 3-1 Test specimens monotonic response parameters.	43
Table 3-2 Voce-Chaboche material model input parameters.....	44
Table 4-1. Test Matrix	86
Table 4-2. Summary of failure modes of specimens.....	87
Table 4-3. Summary of connection performance characteristics.....	88
Table A1. Coupon Tensile Test results.....	171

List of Figures

Figure 1-1: a) Proposed hybrid steel-timber frame building system; b) U-shaped connection.	7
Figure 1-2 Flow chart of major activities and methodology employed in the doctoral thesis.	8
Figure 3-1 U-shaped Steel Plate: a) components; b) rolling bending mechanism; c) scissors bending mechanism.	45
Figure 3-2. Scissor bending mechanism: a) USP geometrical properties; b) simplified analysis model; c) full USP; d) half unit.	46
Figure 3-3. USP effective span (l'): a) welded connection; b) bolted connection; c) Analytical model in tension; d) Analytical model in compression.	47
Figure 3-4. Typical geometry of USP specimens (dimensions in mm).	48
Figure 3-5. USP bending process: a) custom-developed bender; b) bending mechanism; c) blank profile; d) plate bending process; e) final USP products.	49
Figure 3-6. a) Test specimen and setup; b) LVDT positions (back of the specimen); c) strain gauge locations on East Specimen.	50
Figure 3-7. Loading protocol adapted from FEMA 461 (FEMA; & ATC, 2007).	51
Figure 3-8. Force-displacement response: a-d) Specimens S1 – S4.	52
Figure 3-9. USP hysteresis response at 20%D displacement cycle and respective von Misses strains.	53
Figure 3-10. USP plastic mechanism at maximum (final) tension and compression cycles.	54
Figure 3-11. USP force-displacement (backbone) curves.	55
Figure 3-12. Fuse energy dissipation capacity: a) cumulative energy; b) cyclic energy.	56
Figure 3-13. Finite element model: a) boundary conditions; b) contact areas between the fuse and the test setup.	57
Figure 3-14. Hysteresis responses - experimental testing vs. numerical simulation: a-d) S1 – S4.	58
Figure 3-15. Deformed-shape and principal strain distributions at 20%D displacement cycle (FEM on the left and test results on the right): a-c) points a-c; g) point g.	59

Figure 3-16. Numerical and analytical method predictions versus experimental test results: a-b) USP yielding capacities in compression and tension; c-d) UPS initial stiffness in compression and tension. ...	60
Figure 4-1. a) U-shaped steel fuse mechanisms (Mowafy et al., 2023); b) Connection components.....	89
Figure 4-2. a) Flexural deformation under seismic loading; b) Free body diagram of the glulam beam under seismic loading.	90
Figure 4-3. Fuse structural modelling: a) Open-Fuse connection; b) Closed-Fuse connection.	91
Figure 4-4. Analytical model of Open-Fuse Connection: a) Connection FBD; b) Deformation under flexural bending; c-e) Fuse analytical models: ideal, equivalent, and simplified.	92
Figure 4-5. Analytical model of Closed-Fuse Connection: a) Connection FBD; b) Deformation under flexural bending; c-e) Fuse analytical models: idea and equivalent.	93
Figure 4-6. Potential applications: a) Timber Moment Resisting Frame; b) Control Rocking Concentrically Braced frames (CR-CBF).	94
Figure 4-7. Specimens: a-c) GB1-3; d-e) GB4.	95
Figure 4-8. U-shaped fuses: a) 13 mm-thick fuse; b) 16 mm-thick fuse; c) 19 mm-thick fuse; d) 22 mm-thick fuse; e) Side view of the fuse.	96
Figure 4-9. Test setup: a) Three-dimensional view; b) Front view; c) Back view; d) Instrumentation plan; e) Fuse instrumentation.	97
Figure 4-10. Loading protocols: a) FEMA 461 loading protocol proceeded with 10 additional cycles; b) Seismic loading obtained under under the Miyagi, Japan 2011 earthquake proceeded with 4 additional cycles.	98
Figure 4-11: Test setup simplified model: a) at rest; b) during actuator push; c) during the actuator pull.	99
Figure 4-12. Normalized moment-chord rotation responses: a-b) Group I; c-d) Group II; e-f) Group III; g-h) Group IV	100
Figure 4-13. Specimen 16OF-SR (Group I): a) 35th cycle of moment-rotation response; b) Positive 15% rotation; c) Negative 15% rotation.	101

Figure 4-14. Specimen 22OF-DR (Group II): a) 35th cycle of moment-rotation response; b) Specimen deformed-shape at 15% rotation; c) Plastic hinge locations at 15% rotation.....	102
Figure 4-15. Comparison between principal strains: a) Specimen 13OF-SR with single STS reinforcement; b) Specimen 22OF-DR with double STS reinforcement.....	103
Figure 4-16. Specimen R19CF-DR: a) Fuse yielding and initiation of first splitting crack; b) Initiation of second splitting crack; c) Increase in flexural capacity.	104
Figure 4-17. Specimen R19CF-DR: a) Crack propagation in the middle SDDs adjacent to the pin connector; b) Global splitting failure at the end of the test.....	105
Figure 4-18. Specimen moment-rotation backbone curves.....	106
Figure 4-19. Connection energy dissipation: a) Cumulative energy dissipation capacity; b) In-cyclic energy dissipation capacity.	107
Figure 4-20. Connection yield moment: predicted versus experimental.	108
Figure 5-1: a) Proposed hybrid steel-timber frame building system; b) U-shaped connection; and c) Moment-rotation response of the U-shaped connection under cyclic loading.....	137
Figure 5-2: Lateral response of hybrid steel-timber rocking braced frame: a) For equilibrium of the STRBF upon rocking; b) Column uplift θ and fuse connection rotations upon rocking; c) Free body diagram of glulam beam with rocking and counter rocking joints; d) Moment versus uplift angle of the STRBF.	138
Figure 5-3. Design steps for the STRBF.....	139
Figure 5-4: a) U-shaped fuse connection design parameters; b) PT strands inelastic behaviour; c) U-shaped connection inelastic behaviour.....	140
Figure 5-5: a) STRBF fibre-based numerical model; b) U-shaped fuse moment – rotation response: numerical prediction vs. experimental data; c) PT truss element; d) Compression gap element.....	141
Figure 5-6: Seismic response of the prototype STRBF under 2014 Iquique, Chile earthquake record: a) History of frame uplift; b) Overturning moment vs. uplift; c) Fuse connection moment vs. connection rotation; d) PT strand force vs. uplift.....	142

Figure 5-7: Profile of peak response parameters from NLRHA: a) Interstorey drift; b) Fuse connection bending moment; c) Uplift; d) PT strand axial force.	143
Figure 5-8 Profile of peak response parameters from NLRH analyses: a) Storey shear; b) Steel-brace axial forces; c) Steel-column forces; d) Steel-beam forces.	144
Figure 1 1: a) Proposed hybrid steel-timber frame building system; b) U-shaped connection.....	7
Figure 1 2 Flow chart of major activities and methodology employed in the doctoral thesis.	8
Figure 3 1 U-shaped Steel Plate: a) components; b) rolling bending mechanism; c) scissors bending mechanism.	45
Figure 3 2. Scissor bending mechanism: a) USP geometrical properties; b) simplified analysis model; c) full USP; d) half unit.....	46
Figure 3 3. USP effective span (l'): a) welded connection; b) bolted connection; c) Analytical model in tension; d) Analytical model in compression.....	47
Figure 3 4. Typical geometry of USP specimens (dimensions in mm).....	48
Figure 3 5. USP bending process: a) custom-developed bender; b) bending mechanism; c) blank profile; d) plate bending process; e) final USP products.	49
Figure 3 6. a) Test specimen and setup; b) LVDT positions (back of the specimen); c) strain gauge locations on East Specimen.	50
Figure 3 7. Loading protocol adapted from FEMA 461 (FEMA; & ATC, 2007).	51
Figure 3 8. Force-displacement response: a-d) Specimens S1 – S4.....	52
Figure 3 9. USP hysteresis response at 20%D displacement cycle and respective von Misses strains.	53
Figure 3 10. USP plastic mechanism at maximum (final) tension and compression cycles.....	54
Figure 3 11. USP force-displacement (backbone) curves.....	55
Figure 3 12. Fuse energy dissipation capacity: a) cumulative energy; b) cyclic energy.....	56
Figure 3 13. Finite element model: a) boundary conditions; b) contact areas between the fuse and the test setup.	57

Figure 3 14. Hysteresis responses - experimental testing vs. numerical simulation: a-d) S1 – S4.	58
Figure 3 15. Deformed-shape and principal strain distributions at 20%D displacement cycle (FEM on the left and test results on the right): a-c) points a-c; g) point g.	59
Figure 3 16. Numerical and analytical method predictions versus experimental test results: a-b) USP yielding capacities in compression and tension; c-d) UPS initial stiffness in compression and tension. ...	60
Figure 4 1. a) U-shaped steel fuse mechanisms (Mowafy et al., 2023); b) Connection components	89
Figure 4 2. a) Flexural deformation under seismic loading; b) Free body diagram of the glulam beam under seismic loading.	90
Figure 4 3. Fuse structural modelling: a) Open-Fuse connection; b) Closed-Fuse connection.	91
Figure 4 4. Analytical model of Open-Fuse Connection: a) Connection FBD; b) Deformation under flexural bending; c-e) Fuse analytical models: ideal, equivalent, and simplified.	92
Figure 4 5. Analytical model of Closed-Fuse Connection: a) Connection FBD; b) Deformation under flexural bending; c-e) Fuse analytical models: idea and equivalent.	93
Figure 4 6. Potential applications: a) Timber Moment Resisting Frame; b) Control Rocking Concentrically Braced frames (CR-CBF).	94
Figure 4 7. Specimens: a-c) GB1-3; d-e) GB4.....	95
Figure 4 8. U-shaped fuses: a) 13 mm-thick fuse; b) 16 mm-thick fuse; c) 19 mm-thick fuse; d) 22 mm-thick fuse; e) Side view of the fuse.	96
Figure 4 9. Test setup: a) Three-dimensional view; b) Front view; c) Back view; d) Instrumentation plan; e) Fuse instrumentation.	97
Figure 4 10. Loading protocols: a) FEMA 461 loading protocol proceeded with 10 additional cycles; b) Seismic loading obtained under the Miyagi, Japan 2011 earthquake proceeded with 4 additional cycles.	98
Figure 4 11: Test setup simplified model: a) at rest; b) during actuator push; c) during the actuator pull.	99
Figure 4 12. Normalized moment-chord rotation responses: a-b) Group I; c-d) Group II; e-f) Group III; g-h) Group IV	100

Figure 4 13. Specimen 16OF-SR (Group I): a) 35th cycle of moment-rotation response; b) Positive 15% rotation; c) Negative 15% rotation.....	101
Figure 4 14. Specimen 22OF-DR (Group II): a) 35th cycle of moment-rotation response; b) Specimen deformed-shape at 15% rotation; c) Plastic hinge locations at 15% rotation.....	102
Figure 4 15. Comparison between principal strains: a) Specimen 13OF-SR with single STS reinforcement; b) Specimen 22OF-DR with double STS reinforcement.	103
Figure 4 16. Specimen R19CF-DR: a) Fuse yielding and initiation of first splitting crack; b) Initiation of second splitting crack; c) Increase in flexural capacity.	104
Figure 4 17. Specimen R19CF-DR: a) Crack propagation in the middle SDDs adjacent to the pin connector; b) Global splitting failure at the end of the test.....	105
Figure 4 18. Specimen moment-rotation backbone curves.	106
Figure 4 19. Connection energy dissipation: a) Cumulative energy dissipation capacity; b) In-cyclic energy dissipation capacity.	107
Figure 4 20. Connection yield moment: predicted versus experimental.....	108
Figure 5 1: a) Proposed hybrid steel-timber frame building system; b) U-shaped connection; and c) Moment-rotation response of the U-shaped connection under cyclic loading.....	137
Figure 5 2: Lateral response of hybrid steel-timber rocking braced frame: a) For equilibrium of the STRBF upon rocking; b) Column uplift θ and fuse connection rotations upon rocking; c) Free body diagram of glulam beam with rocking and counter rocking joints; d) Moment versus uplift angle of the STRBF.	138
Figure 5 3. Design steps for the STRBF.	139
Figure 5 4: a) U-shaped fuse connection design parameters; b) PT strands inelastic behaviour; c) U-shaped connection inelastic behaviour.....	140
Figure 5 5: a) STRBF fibre-based numerical model; b) U-shaped fuse moment – rotation response: numerical prediction vs. experimental data; c) PT truss element; d) Compression gap element.....	141

Figure 5 6: Seismic response of the prototype STRBF under 2014 Iquique, Chile earthquake record: a) History of frame uplift; b) Overturning moment vs. uplift; c) Fuse connection moment vs. connection rotation; d) PT strand force vs. uplift.	142
Figure 5 7: Profile of peak response parameters from NLRHA: a) Interstorey drift; b) Fuse connection bending moment; c) Uplift; d) PT strand axial force.	143
Figure 5 8 Profile of peak response parameters from NLRH analyses: a) Storey shear; b) Steel-brace axial forces; c) Steel-column forces; d) Steel-beam forces.	144
Figure A1. a) Coupons Specimens; b) Coupons failure shape; c) Yielding Stress for each specimen; d) Sample stress-strain curve for specimen 1	170
Figure B2. Bending Process: a) Blank Profile; b) Bending Mechanism; c) Plate during Bending; d) Final Product.	172
Figure C2. SDDs installation Process: a) Temporary Guided plate; b) Damage in the SDD self-perforating tip; c) Radio Pressing Machine at InnoTech Alberta; d) partially installation of the SDDs.	174
Figure D1. Glulam Beam 1 Specimen Dimensions	175
Figure D2. Glulam Beam 2 Specimen Dimensions	176
Figure D3. Glulam Beam 3 Specimen Dimensions	177
Figure D4. Glulam Beam 4 Specimen Dimensions	178

1. Introduction

1.1 Background and motivation

The hybridization of structural systems, specifically hybrid steel-timber structures, forms a progressive research avenue in structural engineering. This study aims to capitalize on the unique advantages of each material while addressing their limitations. Timber, despite being readily available, cost-effective, lightweight, and easy to erect (Foliente, 2000; Verna et al., 1984), often fails in a brittle manner, which limits its ability to absorb seismic energy effectively (Jorissen & Fragiacomio, 2011). Conversely, steel is known for its high strength-to-weight ratio, which provides significant stiffness and post-yield deflection capacity. These attributes make steel an ideal material for resisting seismic loads and ensuring desirable structural behaviour during major earthquakes. This research focuses on creating and investigating hybrid steel-timber structures that enhance seismic performance and construction efficiency.

The increasing frequency and severity of seismic events around the globe highlight the need for more resilient design solutions. The 1994 Northridge earthquake underlined the importance of SFRSs for life safety and exposed the challenges of dealing with extensive damage and rehabilitation costs (Uang & Bruneau, 2018). More recently, the 2010-2011 Christchurch earthquakes underscored the necessity for rapid recovery and cost-effective building solutions in seismic-prone regions (Goldsworthy, 2012). Therefore, the demand is increasing for structures that ensure safety during seismic events and minimize service disruptions in their aftermath.

In response to the growing demand for resilience, an innovative solution has been proposed: a rocking braced frame system equipped with replaceable fuse connections. This system is built on

two main strategies. First, it incorporates an innovative replaceable fuse connection that dissipates seismic energy and can be easily replaced after an earthquake, significantly accelerating recovery efforts. Second, it employs a self-centring braced frame that allows for rocking at its base and uses post-tensioned strands to bring the structure back to its original position. This method aims to minimize both structural and non-structural damage, typically confining it to the replaceable elements, thereby reducing the overall impact of significant seismic events.

This research project proposes an in-depth examination of the seismic behaviour of a new hybrid steel-timber structure, integrating these resilient design principles. This investigation involves numerical simulations and experimental work, focusing on seismic-induced forces in the members and connections. The study also introduces a self-centring system with rocking capability in the steel-braced frames to achieve superior seismic performance. The ultimate goal is to contribute to a paradigm shift in the adoption of hybrid structures that capitalize on the strengths of respective materials to achieve efficient resilient buildings. The outcomes from this project will contribute significantly to the current body of knowledge and further support the case for wider application of hybrid steel-timber structures in seismic-prone regions.

1.2 Research scope and objectives

This doctoral thesis explores hybrid steel-timber systems where a steel braced frame handles lateral loads, and a mass timber frame carries gravity loads (Figure 1-1a). Steel is preferred for its predictable and ductile behaviour, higher response modification factor, and enhanced stiffness. The major challenge is creating an efficient connection between the two systems to prevent excessive moments in the timber frame during seismic events. To address this, a new connection has developed that withstands gravity loads in mid-rise buildings, absorbs seismic energy, and

accommodates extensive rotational demands during large lateral displacements. As shown in Figure 1-1b, this connection features a U-shaped joint, including a mild steel pin connector and two cold-bent U-shaped steel fuses to resist shear and flexural bending. These components are secured to a glulam beam using structural bolts, an end T-plate, and self-drilling dowels (SDD).

The key objectives of this research are as follows:

- To conceptualize, design, and test beam-to-column joints that can act between steel and mass timber systems. This involves:
 - a. Evaluating the replaceable U-shaped fuses employed in the connections independently. The aim is to understand the cyclic behaviour of the fuses and determine the probable maximum yielding force, which in turn helps to protect the capacity of the other connection components.
 - b. Assessing the overall hysteresis response of the developed connection and testing the capacity-protected members and connections under cyclic loading.
- To develop a comprehensive seismic design procedure specifically tailored for steel-timber hybrid structural systems.
- To evaluate the proposed steel-timber hybrid system's seismic response, considering its inherent structural attributes and the innovative connections proposed.

The findings from this research are expected to contribute significantly to the current understanding and application of hybrid steel-timber systems in seismic-prone areas. They

should provide valuable insights and practical solutions to designers and engineers working in the field.

1.3 Methodology

This research utilizes a structured methodology that combines experimental testing, numerical modelling, and design optimization methods to thoroughly investigate the proposed hybrid steel-timber systems, as depicted in the methodology flow chart (Figure 1-2).

The first stage, 'I. Literature Review', examines existing literature and methodologies within the field, laying the foundation for the subsequent studies. The second stage, 'II. Connection development', is divided into two sub-studies. The first, 'a) Fuse testing program,' focuses on the design and evaluation of U-shaped fuses that are critical to the hybrid system, assessing their cyclic behaviour and maximum yielding force. The second sub-study, 'b) Connection testing,' integrates these U-shaped steel seismic fuses into a hybrid timber beam-to-steel column connection system and tests multiple configurations under cyclic load to investigate its cyclic properties, failure modes, design parameters, and capacity-protected items. The final stage, 'III. Design guidelines', develops a comprehensive seismic design procedure that is unique to the hybrid system. This procedure is validated through detailed numerical analyses, with the final hybrid steel-timber rocking braced frame system.

Overall, this research employs a systematic and iterative approach, as illustrated in the methodology flow chart, allowing for a detailed evaluation and continuous improvement of each component of the system. The outcome is an optimized hybrid steel-timber system with high seismic performance.

1.4 Thesis outline

The thesis is structured into six comprehensive chapters that collectively build a substantial argument for advancing seismic resilience in hybrid steel-timber structures.

Chapter 1, the present chapter, introduces the study by outlining the background, motivation, research objectives, scope, and methodology. It sets the tone for the thesis by framing the research problem and detailing the methods used to address it.

Chapter 2, the Literature Review, provides a comprehensive review of existing research on hybrid steel-timber structures, seismic design, and connection technologies. It includes an examination of resilient design needs stemming from past earthquakes and a discussion of the roles of various connections and fuses in hybrid structures. Moreover, it explores the potential of self-centring systems and discusses the use of wood in these contexts. The chapter concludes by identifying research gaps and how the current research contributes to the field.

Chapters 3 to 5 serve as the core of this thesis, presenting the research conducted to enhance the seismic resilience of hybrid steel-timber structures. Chapter 3 discusses the novel U-shaped steel seismic fuse and its unique scissor-bending mechanism. Chapter 4 details development of an innovative hybrid timber beam-to-steel column connection system. Chapter 5 introduces a new low-damage, self-centring hybrid steel-timber rocking braced frame. Each of these chapters is in the process of being submitted for publication in refereed journals.

Chapter 6, the final chapter, wraps up the thesis with conclusions drawn from the research and provides recommendations for future study. It summarises the main contributions of the research and emphasizes the importance of such advancements in the face of seismic events. It also

outlines proposed further research, including developing new connection types and validating design guidelines in real-world applications.

Throughout the journey of this thesis, from chapters 1 to 6, we delved deeper into the potential of hybrid steel-timber structure as an efficient resilient system. This journey is not merely an academic exercise; rather, it signifies a practical quest toward creating resilient, safe, and sustainable built environments.

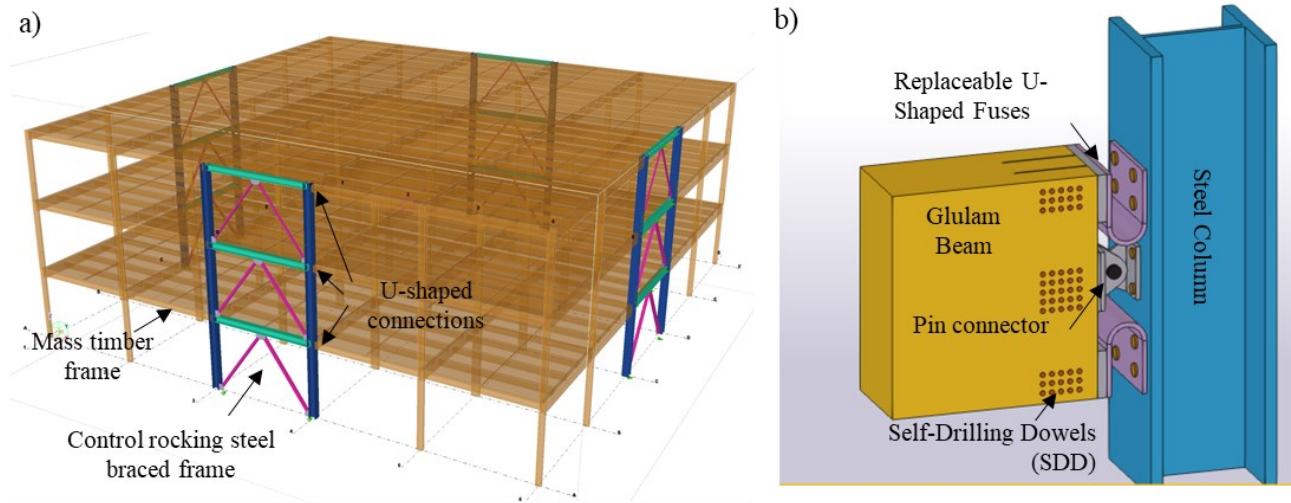


Figure 1-1: a) Proposed hybrid steel-timber frame building system; b) U-shaped connection.

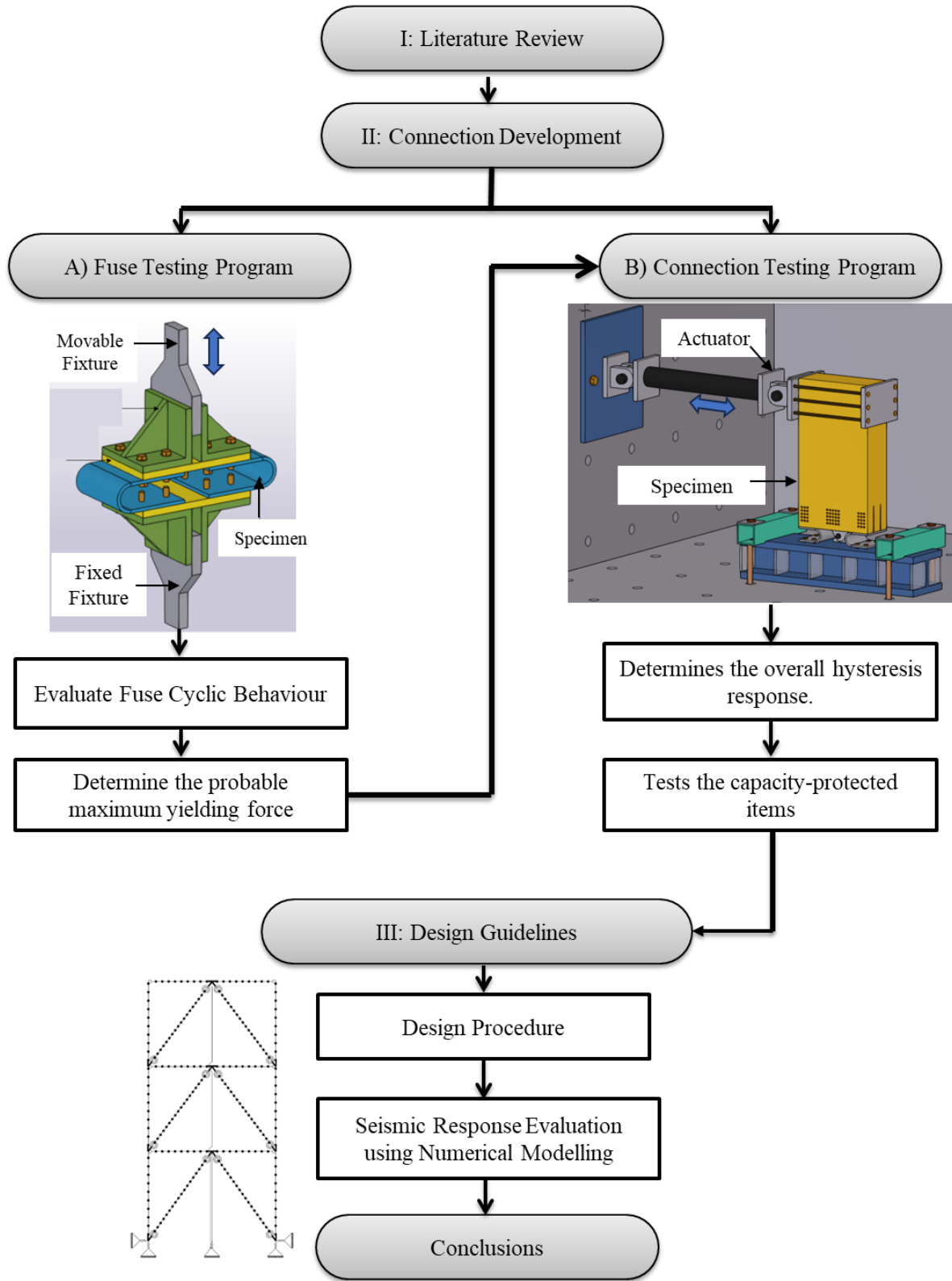


Figure 1-2 Flow chart of major activities and methodology employed in the doctoral thesis.

2. Literature review

Several hybrid steel-timber structural systems have been increasingly developed during the past two decades. They combine the benefits of both materials, resulting in efficient and durable structures. Based on the degree of steel and timber combination, these systems are generally divided into three categories: 1) At the connection level, 2) At the component level, and 3) At the building system level.

At the connection level, steel is used in connectors to provide ductility in the hybrid structure, an essential characteristic of seismic resilience. This strategy manifests in the use of steel connectors such as angle brackets and hold-downs in mass timber braced frames (MTBF) and cross-laminated timber (CLT) shear walls (Gavric et al., 2015; Popovski & Gavric, 2016). Another example includes the implementation of high-capacity hold-downs in CLT structures (X. Zhang et al., 2018). Furthermore, some designs feature the use of perforated steel plates in CLT and MTBF structures (Daneshvar et al., 2022) or U-shaped steel plates in laminated veneer lumber (A. Iqbal et al., 2015). A particularly innovative application from New Zealand involves a pre-stressed timber connection with self-centring capability, thereby augmenting the structure's seismic resilience (A. Buchanan et al., 2008).

The second category of hybrid steel-timber structures involves steel and timber in a lateral load-resisting system (LLRS). This category has seen various innovative solutions. For example, the use of steel moment-resisting frames paired with infill CLT walls (Tefamariam et al., 2014b) or infill wood-frame shear wall panels (M. He et al., 2014). A unique strategy known as the Finding the Forest in the Trees (FFTT) integrates steel beams amidst CLT shear walls to boost structural performance (X. Zhang et al., 2016). Additional developments within this classification include

the Controlled Rocking Heavy Timber Walls (CRHTW) (Kovacs & Wiebe, 2016) and hybrid self-centring steel-timber rocking core walls featuring slip friction connections (Hashemi et al., 2016). These examples demonstrate the effective utilization of the strengths of both steel and timber in hybrid systems.

The third category distinguishes itself by employing steel and timber independently. Here, steel system serves as the lateral load resisting system (LLRS), while timber frame performs the role of the gravity load resisting system (GRLS). This classification is exemplified by several structural systems, including steel moment-resisting frames (Xinxian et al., 2016), steel friction braces (Gilbert & Erochko, 2016), and steel buckling-restrained braced frames (BRBFs) (Gilbert & Erochko, 2019). Moreover, conventional steel braced frames further underline the broad spectrum of possibilities within this third category of hybrid steel-timber structures (Mowafy et al., 2021).

Upon discussing the diverse hybrid steel-timber structures, the literature review dives deeper into resilient design needs in seismic design, drawing crucial lessons from significant past earthquakes. Thus, an emphasis is placed on the role of self-centring systems, their advantages, and their critical importance in enhancing a structure's capability to withstand and recover from seismic events. Connection strategies specific to mass timber are thoroughly analyzed, presenting their strengths and challenges. The narrative then turns to an in-depth exploration of structural fuses, with a unique focus on U-shaped steel plates utilized in this research. The review concludes in identifying and addressing gaps in the current body of research, thereby clarifying the unique contributions of this study.

2.1 Needs for resilience in seismic design: Lessons from past earthquakes

After the 1994 Northridge earthquake that caused considerable economic losses, revolutionary modifications were made to North America's seismic design regulations (Uang & Bruneau, 2018). New seismic design approaches were introduced, such as ductility and capacity design (Canadian Standards Association, 2014b). The ductility design approach depends on dissipating the energy that affects the building during seismic excitation through plastic deformations. These plastic deformations should be limited to specific structural elements known as seismic fuses since it may be costly to ensure ductility in all structural components (Landolfo et al., 2017). Therefore, the capacity design concept ensures that the failure is only localized in the dissipative elements. This concept is achieved by considering their measured material properties and structural overstrength while designing capacity-protected components.

The performance-based seismic design approach has fostered multiple applications over the past two decades. Steel moment-resisting frames (MRFs) are an example of this approach. MRFs provide open-space floors for architectural flexibility. However, their adoption is tempered by relatively higher construction costs and lower lateral stiffness (Bruneau et al., 2011; Paul et al., 2000; Uang & Bruneau, 2018). The flexibility inherent to MRFs can be a limiting factor in high-rise buildings, where design often must conform to strict drift criteria.

The steel concentrically braced frames (CBFs), on the other hand, use the buckling and tensile yielding of diagonal braces as primary sources of energy dissipation (KHATIB et al., 1988). Efforts have been made to improve the energy dissipation characteristics of the bracing members, increase system redundancy, and prevent brittle failure in braces or connections under cyclic load

(Tremblay, 2001). Due to their sufficient lateral stiffness, high strength, and aesthetic appeal, they have become a popular option for seismic design.

The steel eccentrically braced frames (EBFs) merge the high ductility of MRFs with the high stiffness of CBFs (Popov & Engelhardt, 1988), offering flexibility in architectural design with large openings and walkways. Similarly, Buckling Restrained Braced Frames (BRBFs) are a variant of the CBFs, with specific detailing to prevent global buckling of the braces, allowing ductility to develop through yielding in tension and compression (Xie, 2005). Lastly, steel shear walls involve columns that act as flanges and steel infill plates that act as the web (Bruneau et al., 2011).

Despite the reliability of lateral load-resisting systems in most conventional designs shown previously, significant residual deformations can still occur following seismic events (Hwang & Lignos, 2017). This often results in complex rehabilitation tasks, such as replacing fuses or reinforcing the compromised parts of a building, causing issues including extended downtime, the requirement for specialized labour, and high material costs. These challenges have encouraged research initiatives to develop systems that limit the extent of damage to a smaller, manageable portion of the structure, reducing both the complexity of repair efforts and the associated costs.

The seismic design has recently experienced a notable transformation, focusing on economic strategies that can lower repair costs and expedite recovery following major earthquakes. The 2010-2011 Christchurch earthquake series highlighted the necessity for such a paradigm shift in approach (Chancellor et al., 2014; Pampanin, 2012; Uang & Bruneau, 2018). This evolution in design philosophy has stimulated the development of seismically resilient systems that contain and manage damage, thereby improving seismic performance by limiting structural vulnerability and

shortening the time required for post-seismic repairs. In the following sections, the focus will be on how researchers are addressing this issue from both system and connection perspectives, specifically by employing self-centring systems to increase structural resilience.

2.2 Self-centring systems

The study of self-centring systems has advanced over the years, deepening the field's understanding of their function and benefits. Initial investigations centred on the advantages of rocking (Clough & Huckelbridge, 1977), the influence of uplifting and vertical forces (Housner, 1963; Pollino & Bruneau, 2004), and the three-dimensional impacts of uplifting elements on floor framing (Lu, 2004). As the field evolved, innovative solutions such as yielding base plates (Azuhata, T. et al., 2006) and hydraulic dampers at column bases (Tremblay et al., 2008) were developed. An effort was done to ensure the probabilistic mechanisms reducing residual drifts in systems with minimal restoring force (Eatherton & Hajjar, 2011). Concurrently, multiple studies were conducted including those that investigated steel-braced frames with several uplifting points forming control rocking joints in order to mitigate higher mode effects (Panagiotou & Jos'e I. Restrepo, 2007; Wiebe et al., 2012). Simultaneously, three different frame configurations for rocking-braced frames were introduced and examined (Roke et al., 2009b). These combined efforts have significantly enriched the understanding and usability of rocking systems.

Large-scale experiments have validated the efficacy of self-centring systems, with their global applications reinforcing their importance in seismic-resilient structural design (Eatherton, 2010; Eatherton, Ma, Krawinkler, Deierlein, et al., 2014; Sause et al., 2010). This understanding has led to the development of guidelines for key limit states and replaceable fuse elements for damage concentration (Eatherton, Ma, Krawinkler, Mar, et al., 2014; Ma, 2010). Design methodologies

have been developed to account for elastic forces and prioritize maximum member forces, especially in base rocking joints (Wiebe & Christopoulos, 2015b, 2015a), accompanied by performance-based design methodologies to ensure these systems return structures to their original position post-severe earthquakes with minimal damage (Dyanati et al., 2015).

Past research has helped categorize self-centring frame systems with rocking capabilities based on the configuration of the primary components: the rocking frame, post-tensioning (PT), and the energy-dissipating (ED) fuse. These categories include:

- Gravitation self-centring system: This type leverages gravity load affecting the frame columns, providing self-centring without the need for post-tensioning bars. Past applications focused on enhancing seismic performance in existing buildings (Mottier et al., 2018, 2019; Pollino, 2015).
- Bottom fuse systems: These systems are characterized by the absence of lateral deformation at the base, making it an ideal location for shear fuses (Eatherton, 2010; Ma et al., 2010). Various arrangements of fuses and post-tensioning bases centred or at the column base have been explored.
- Dual frame system: This type features yielding shear elements situated between two rocking frames (Eatherton & Hajjar, 2011).
- Multiple hinges system: This system incorporates multiple hinges to mitigate the effect of higher modes and reduce the elastic shear and moment demands on the intermediate floors (Wiebe & Christopoulos, 2009).

- Floor fuses system: This system utilizes fuses at each floor level, aiming to increase energy dissipation in the higher modes of vibration (Roke et al., 2009b).

Self-centring systems have been effectively employed in mass timber structures. One such application involves integrating U-shaped flexural plates with Laminated Veneer Lumber (LVL) or Cross-Laminated Timber (CLT) walls to create controlled rocking heavy timber walls that enhance seismic resilience (A. Iqbal et al., 2015; Kovacs & Wiebe, 2016). An approach utilizing resilient slip friction joints as energy dissipaters was employed to enhance the overall stability of the structures (Hashemi et al., 2020). A self-centring steel-timber hybrid shear wall was proposed to combine a Post-Tensioned (PT) steel frame with a light wood frame shear using slip friction dampers as energy dissipaters (Cui et al., 2020).

2.3 Connection development in mass timber

Mass timber structures are increasingly used in earthquake-prone areas because of wood's advantages in lower mass, sustainability, and prefabrication. The combination of wood with other materials, such as steel, can result in improved structural efficiency. Developing efficient connections that can provide a secure load path during earthquakes, particularly with moment-resisting capability, is a significant challenge facing the timber construction industry. Therefore, researchers have focused on developing these connections in recent years. Based on published literature, these connections can be categorized into four distinctive groups: 1) Traditional connections, which exhibit limited ductility and lean towards a brittle failure mode; 2) Connections possessing energy dissipation capabilities yet with a brittle failure mode; 3) Connections demonstrating a ductile failure mode; 4) Connections with replaceable fuses.

Timber connections falling under the traditional category exhibit limited ductility and a tendency towards a brittle failure mode. Examples of these include nailed moment joints (Bryant et al., 1981) and bolted slotted-in steel plate connections (Cao et al., 2022; M. He et al., 2017). These connections are characterized by a limited capacity to deform plastically before breaking, potentially leading to sudden and catastrophic failure during seismic events.

The second category includes connections that possess energy dissipation capabilities, albeit coupled with a brittle failure mode. Efforts have been made to improve the ductility of traditional connections and the overall performance by using rods glued parallel to the grain in end-roof and multi-storey connections (A. H. Buchanan & Fairweather, 1993). Ductility can also be introduced by applying self-tapping screws to bolted slotted-in steel plate connections, which reduces splitting (Lam et al., 2010). Further, bolted beam-to-column glulam connections have been reinforced with locally cross-laminated glulam members, increasing the maximum moment, deformability ratio, and energy dissipation of the connections (Wang et al., 2015). A proposed hybrid timber beam-to-steel column joint employing steel angles connected to the glulam beam through long steel bolts for energy dissipation displayed brittle failure modes, including splitting, plug shear, and crushing, further solidifying its placement in this category (Sirumbal-Zapata et al., 2019). Nevertheless, despite these modifications, the failure mode of these connections remains largely brittle, keeping them within this category.

The third category entails connections that exhibit a ductile failure mode. Key advancements in this category originated with the development of prestressed timber beam-column connections, which exhibit minimal residual deformations and damage, contributing to enhanced seismic performance (a Iqbal et al., 2010). Following this, additional strides were made with the introduction of wooden elements connected to a steel stub with an end plate and glued-in steel rods

(Andreolli et al., 2011). Another enhancement was discovered when dowel-type fasteners were employed as reinforcement in bolted connections, effectively shifting the failure mode from brittle to ductile. This alteration improves lateral resistance and lessens the likelihood of wood splitting (M. J. He & Liu, 2015). Building on this, a novel connection design was proposed that involves three separate steel box sections linked with glued-in rods to a glulam beam end and connected with bolts to a glulam column (Yang et al., 2016). More recent developments include the utilization of self-taping screws (STS) in glulam beam-column moment connections with self-drilling dowels (SDDs). This technique has been found to reduce timber splitting and promotes full yielding of the SDDs (Dong et al., 2021a).

Finally, the fourth category encompasses connections designed for replaceability. These connections feature replaceable sacrificial elements that can be promptly replaced after a seismic event, thereby reducing structural downtime and rehabilitation costs. A key example of this is the hybrid moment-resisting frame connection with replaceable steel links, a groundbreaking proposal by Gohlich et al. (Gohlich et al., 2018). Despite the clear potential, such advanced replaceable-fuse connections remain limited in their deployment and application (Ottenhaus et al., 2021). Therefore, the development and implementation of replaceable connections represent a significant gap in the current body of knowledge that warrants further research focus.

2.4 Structural fuses and dampers in seismic resilience

One approach to enhancing seismic resilience in building structures is the use of structural fuses or dampers. These devices are designed to absorb and dissipate energy, reducing the impact of seismic activity on the primary structure. The use of steel triangular plates has been demonstrated to be effective, with these structures capable of sustaining numerous yielding reversals without

suffering degradation in stiffness or strength (Tasi et al., 1993). Additionally, the application of plate-based dampers, such as U-shaped steel dampers, has been widely recognized in Japan for their utility in disaster prevention bases following earthquakes (Suzuki et al., 2005).

The development of more sophisticated devices, such as shear panel dampers crafted from low-yield steel (Nakashima et al., 1994), dual function metallic dampers (DFMDs) (Li & Li, 2007), Perforated Yielding Shear Panel Devices (PYSPDs) (Chan et al., 2013), and dual-pipe dampers (DPDs) (Maleki & Mahjoubi, 2013) has further improved seismic resilience capabilities. DFMDs, for instance, provide not just additional structural stiffness, but also have considerable seismic energy-dissipation capabilities. Similarly, shear panels made of low-yield steel exhibit a large energy dissipation capacity, as do the PYSPDs, which employ plastic shear deformation of a perforated diaphragm plate to achieve a stable force-displacement hysteresis. The DPDs introduced by Maleki and Mahjoubi (2013) not only provide superior strength, stiffness and energy dissipation compared to single pipe dampers, but are also economical, lightweight, and easy to fabricate. The continued development and application of such innovative dampers symbolize the significant progress made in the field of seismic resilience.

Enhancing seismic resilience in structures encompasses the utilization of a variety of advanced damper designs. Hybrid-shaped dampers, like j-dampers, reduce earthquake-induced forces in structures, demonstrating their resilience against large deformations during severe seismic activities (Kato et al., 2005). Crawler dampers, with their unique design of U-shaped steel plates, are engineered for high strength and deformation, which is critical for certain structures such as bridges (Deng et al., 2013). Buckling restrained dampers use a core material that buckles while a covering material eliminates global buckling, effectively absorbing seismic energy (Dongbin et al., 2016). The economical Bar-Fuse Dampers use round steel bars as replaceable energy absorbers

(Aghlara & Tahir, 2018), and Accordion Dampers employ corrugated thin-walled tubes as repairable hysteretic fuses to augment structural resilience (Motamedi & Nateghi-A., 2018). Each of these dampening solutions contributes to improving seismic resilience in modern infrastructures.

These damping techniques have been creatively integrated into timber construction as well. From as early as the use of steel energy dissipation devices in timber shear walls (Kelly et al., 1972), such methods have continuously evolved. They have been adapted to include more intricate solutions like glulam beam-to-column connections that employ steel angles for energy dissipation, providing an extra layer of structural resilience (Sirumbal-Zapata et al., 2019). With the primary objective of reducing seismic damage, these damping systems have even been applied in more complex ways, such as the introduction of perforated steel plates in Cross Laminated Timber (CLT) and mass timber braced frames (Daneshvar et al., 2022). Despite their complexity, these applications aim to improve structural performance during seismic events and further popularize sustainable construction practices.

2.5 U-shaped steel plates as seismic fuses

Building on the exploration of structural fuses and dampers in seismic resilience, this study specifically focuses on the application of U-shaped Steel Plates (USP) as seismic fuses. Initially developed by Kelly et al. (Kelly et al., 1972), USPs are integral components of seismic energy dissipation systems. The plates allow relative motion parallel and perpendicular to their legs, initiating appropriate rolling bending and tension-compression mechanism respectively that efficiently dissipates seismic-induced energy. These elements have been chosen for our connection development due to their various advantages. Bent U-shaped steel plates are attractive due to their

cost-effective fabrication, ease of installation and replacement, and their excellent inelastic characteristics, including high energy dissipation capability and robust resistance to fatigue (Baird et al., 2014; Priestley, 1996). They are particularly suited for the purpose of isolating lateral load resisting system from gravity load resisting system due to their ability to undergo large elastic and in-elastic deformations. This potent combination of practical and performance benefits makes USPs an optimal choice for enhancing seismic resilience.

U-shaped Steel Plates (USP) have been implemented in a diverse array of structural systems. They have found applications in precast concrete (Priestley, 1996), post-tensioned timber coupling shear walls (A. Iqbal, 2016; A. Iqbal et al., 2007; Newcombe et al., 2010), column-wall-column timber systems (Sarti et al., 2014), and in steel structures to create new seismic dampers (Mashal et al., 2019; Qu et al., 2019), energy dissipative braces (Taiyari et al., 2019), and cross-bracing connections (Bagheri et al., 2015; Henriques et al., 2019a; Jensen et al., 2012). The majority of these applications involve the plates undergoing rolling deformation, a phenomenon thoroughly studied (Baird et al., 2014; Deng et al., 2013). However, one intriguing exception is the work of Henriques et al. (2019), which investigated USP under transverse loads. The application of USP in seismic applications in which USP experiences scissor bending, i.e., plate bending that occurs due to loads applied perpendicular to fuse legs, has not yet been studied. Moreover, the nonlinear plastic mechanism of USP under such loading conditions has not been formulated yet.

2.6 Research gaps and contributions of this study

This thesis recognizes several distinct knowledge gaps, which shape the focus of our research. Firstly, the performance and application of U-shaped Steel Plates (USP) as seismic fuses under scissor bending conditions, where loads are applied perpendicular to the legs, remain largely

unexplored. The nonlinear plastic behaviour of USPs under these conditions is also an uncharted territory. Addressing these areas will enhance our understanding of the USP's performance under different load conditions, leading to more reliable and efficient use of these devices in seismic design.

Secondly, the design and implementation of replaceable connections, particularly in timber structures, have not been sufficiently explored. This research gap calls for dedicated investigations to develop novel replaceable connection designs, thereby enhancing the resilience of our built environment against seismic events.

Lastly, the utilization of steel in the development of self-centring braced frames in mass timber structures is a relatively unexplored strategy. This approach offers promising potential for enhancing the seismic resilience of timber structures but requires additional research for effective realization. These identified research gaps shape the thrust of our investigation in this thesis.

3. Cyclic Behaviour and Plastic Mechanism of a U-shaped Steel Seismic Fuse

3.1 Introduction

The lessons from the 1994 Northridge earthquake led to substantial advancements in the seismic design of building structures around the world, emphasizing on structural safety (Uang & Bruneau, 2018). In recent years, seismic design has undergone a paradigm shift, with a growing emphasis on cost-efficient solutions that can minimize repair costs and business downtime to ensure quick recovery, even after major earthquakes. This shift in performance objectives is particularly evident in the wake of the 2010-2011 Christchurch earthquake series (Chancellor et al., 2014; Pampanin, 2012; Uang & Bruneau, 2018). This design methodology has also motivated the development of seismically resilient systems with limited and controlled damage, improving seismic performance by reducing the tolerance to damage and delaying repair, especially after major seismic events. For instance, steel dampers, including plate-based dampers (Li & Li, 2007; Suzuki et al., 2005; Tasi et al., 1993), shear panel dampers (Chan et al., 2013; Nakashima et al., 1994), tube-based dampers (Maleki & Mahjoubi, 2013), buckling restrained dampers (Dongbin et al., 2016), hybrid-shaped dampers like j-dampers (Kato et al., 2005), crawler dampers (Deng et al., 2013), bar-fuse damper (Aghlara & Tahir, 2018), accordion damper (Motamedi & Nateghi-A., 2018), and perforated steel plates (Daneshvar et al., 2022), are among the most popular applications of such systems. Other applications, for example in mass timber structures, include glulam beam-to-column connections with steel angle (Sirumbal-Zapata et al., 2019) and timber shear walls equipped with steel energy dissipation devices (Kelly et al., 1972).

* The content of this chapter is being prepared and will be submitted as a journal manuscript.

U-shaped Steel Plates (USP) (Figure 3-1a) initially developed by Kelly et al. (Kelly et al., 1972) have been used in seismic energy dissipation systems where relative motion is applied parallel to the legs, elongating one of the legs while the other one is expected to shorten to transfer shear between adjacent members. This mechanism would allow USP to dissipate seismic-induced energy through rolling bending, as shown in Figure 3-1b. USP has been used in precast concrete (Priestley, 1996), post-tensioned timber coupling shear walls (A. Iqbal et al., 2007; Newcombe et al., 2010), post-tensioned timber walls, and column-wall-column timber systems (Sarti et al., 2014) where relative motion parallel to the legs of USP is allowed to engage the rolling bending mechanism. In steel structures, USP has been used to develop new seismic dampers (Mashal et al., 2019; Qu et al., 2019), energy dissipative braces (Taiyari et al., 2019), and cross-bracing connections (Bagheri et al., 2015; Henriques et al., 2019a; Jensen et al., 2012).

Extensive research has been carried out to understand the plastic mechanism and cyclic response of USP undergoing rolling deformation where the load acts parallel to USP legs (Figure 3-1b). Furthermore, analysis and design methods have been developed for structural systems involving USP (Baird et al., 2014; Deng et al., 2013). Henriques et al. (Henriques et al., 2019a) investigated the cyclic response of steel brace connections with USP under transverse loads. However, the application of USP in seismic applications in which USP experiences scissor bending, i.e., plate bending that occurs due to loads applied perpendicular to the legs (Figure 3-1c), has not yet been studied. Moreover, the nonlinear plastic mechanism of USP under such loading conditions has not been formulated yet. This paper aims to formulate the plastic mechanism of USP under transverse loading and evaluate its cyclic behaviour as a seismic fuse.

3.2 U-shape steel plate mechanism

The plastic mechanism of a USP under transverse loads can be described via a scissor analogy (Figure 3-1c), where plate bending involves closing and opening the legs, similar to a scissor. This type of plate bending is referred to as scissor bending and is analytically simulated using the bent and part of the legs involved in scissor bending with guided supports, as shown in Figure 3-2. Figure 3-2a illustrates USP used in the scissor bending mechanism with bent centreline radius, R_{cl} , and leg length, L , which is typically connected to a plate through a contact leg, L_c , and has a free length, L_f . A smaller free length, L_f , leads to greater scissor bending stiffness, which in turn, increases the force required to open or close the scissor, P .

The deformed-shape of USP under the force P , which causes a scissor displacement of Δ in the vertical direction, is shown in Figure 3-2c. Assuming symmetry with respect to point A , only half of USP can be analyzed, as shown in Figure 3-2d. Using the free body diagram of the half unit shown in Figure 3-2d, the equilibrium of forces in the vertical direction and moments are established. Moments M_A , at point A , and M_B , at point B , are obtained using the Virtual Work Method (VWM):

$$M_A = M_B = P \cdot l' / 2 \quad \text{(Equation 3-1)}$$

where l' is the horizontal distance between points A and B , or the effective span of USP. To calculate the flexural stiffness of the fuse, K , the VWM is applied again, assuming that deflection at point B is half of the scissor displacement, Δ , due to symmetry, which results in USP flexural stiffness as follows:

$$K = P / \Delta = (6/5)(EI / l'^3) \quad \text{(Equation 3-2)}$$

The ultimate limit state of the plate, i.e., full plastic mechanism, is obtained assuming three flexural Plastic Hinges (PHs) forming at points A , B and C (Figure 3-2c) under the combined effect of an

axial force and flexural bending. The compressive yielding capacity of USP, P_{cy} , is therefore determined as follows:

$$P_{cy} = wtF_y\xi \quad \text{where } \xi = \frac{2}{1 + 4(l'/t)} \quad \text{(Equation 3-3)}$$

in which w is the width of the fuse out-of-plane, t is the plate thickness, and F_y is the yield stress of the steel material. ξ is defined as an eccentricity factor.

The same equations can be used for calculating the tensile yielding capacity, P_{ty} , of the fuse using the respective effective span, l' , which varies depending on the contact length, L_c (Figure 3-2a). The contact length, in turn, is influenced by the method used to connect the fuse leg to the connection plates (Figure 3-3), which can be welded or bolted to USP. In a welded connection (Figure 3-3a), welds cover the entire contact area between the plate and the fuse leg, creating an identical contact length in both tension and compression loading. When a bolted connection is used to connect USP to other components of the system, the contact length in tension, $L_{c,ten}$, extends from the free end of the fuse leg to the end of the second bolt edge (Figure 3-3b), whereas, in compression, $L_{c,comp}$ stretches up to the end of the plate (Figure 3-3) since the compression force closes the gap from the bolt edge to the end of the connection plate. Figure 3-3c and Figure 3-3d show USP analytical models for tension and compression loading, respectively. Note that the free length of the fuse in tension, $L_{f,ten}$ exceeds that in compression, $L_{f,comp}$, resulting in a longer effective span in tension, l'_{ten} , compared to that when USP is subjected to compression, l'_{comp} .

The employed analytical model in this study assumes a restrained rotation between the fuse leg and the horizontal plate of the testing fixture. This approach was adopted as the development of

pure scissor bending poses significant challenges in tests of this nature. The discrepancy observed arises from the deviation between the theoretical scissor bending mechanism and the constraints of the experimental setup, leading to the formation of three plastic hinges as opposed to one. The test configuration aligns with using fuses in a closed-shape orientation. While this variation does not compromise the integrity of the core findings, it underscores the complexities of simulating idealized conditions in a laboratory setting.

3.3 Test specimens and setup

An experimental program was designed to investigate USP's plastic mechanism and cyclic response. This section presents the design and manufacturing of four pairs of U-shaped specimens, the experimental setup, and the cyclic loading protocol used to perform the tests.

3.3.1 Test specimens

Plate thickness was the primary variable changed among U-shaped specimens tested here. The dimensions were chosen using the analytical model described in section 3.2 to achieve yielding capacities ranging from 100 to 400 kN, which are deemed to be practical for typical use in seismic force-resisting systems, such as beam-to-column connections of steel-timber hybrid seismic force-resisting systems (SFRSs), beam-to-column connections of timber moment-resisting frames, and braces in timber braced frames. Four pairs of U-shaped specimens were designed, each with a unique thickness as follows: 13 mm, 16 mm, 19mm, and 22 mm, which are associated with Specimens 1 to 4 (S1 to S4), respectively. The remaining geometrical properties of the specimens were kept identical, as shown in Figure 3-4.

Specimens were made of flat steel plates conforming to CSA G40.21 300W (CSA & Association, 2013) with a specified yield strength of 300 MPa. Due to the relatively large thickness to be bent to form the U-shaped plates, a custom bender with a triple-shaft system was manufactured, as shown in Figure 3-5a. The plate was positioned on the two stationary shafts, and the central shaft applied the load through a hydraulic jack (Figure 3-5b). The blank profile therefore deformed gradually into a V shape as shown in Figure 3-5c and then it was extruded as a U-shape (Figure 3-5d) off the open end of the machine. The bending load applied was 250 kN for the thinnest specimen and 700 kN for the thickest one. The specimens were bent without heat treatment. Standard tensile tests were conducted on eight coupon specimens (two per each plate thickness) taken from flat plates to obtain the stress-strain relationship, including yield stress (F_y) and tensile strength (F_u). The average values of yield and tensile strengths are as follows: $F_y = 347$ and $F_u = 595$ MPa for 13mm-thick plate, $F_y = 349$ and $F_u = 575$ MPa for 16mm-thick plate, $F_y = 345$ and $F_u = 589$ MPa for 19mm-thick plate, and $F_y = 333$ and $F_u = 611$ MPa for 22mm-thick plate.

3.3.2 Test setup and instrumentation

The experimental setup is shown in Figure 3-6. The setup was designed to test a pair of identical UPS specimens assuming a symmetric response between the left and right fuses. The test setup consists of two identical testing fixtures attached to the uniaxial testing machine through its grips. Each fixture has two back-to-back angles welded to a 50-mm thick intermediate plate, which itself is attached to the machine's arm. Upper and lower distributing horizontal plates were sandwiched between the horizontal legs of angles and the legs of U-shaped plates using structural bolts to evenly distribute the applied load between fuse legs. The orientation of the fuses in the test was deliberately chosen to be the "Closed-fuse orientation" to prevent contact between the bent part and the horizontal plates. Four 19-mm ASTM A490 high-strength steel bolts that are pre-tensioned

were used to connect the specimens to the horizontal distributing plate and eventually to the horizontal legs of angles (ASTM International, 2020). The specimens were subjected to cyclic displacement using the FEMA 461 loading protocol (FEMA; & ATC, 2007). The displacement was applied through the upper arm while the lower arm remained fixed. The displacement increased progressively, reaching a maximum of 6 mm between the legs before advancing to 20 mm. The maximum displacement and load were limited to 25 mm and 1000 kN, respectively, due to laboratory constraints.

Four Linear Variable Differential Transformers (LVDTs) were positioned in the back of the specimen along with the outer and inner bolts to measure the relative displacement of the legs, i.e., scissor displacement (Figure 3-6b). Vertical displacement was applied to USP via the upper testing fixture using a hydraulic operating system in the displacement-controlled mode by controlling the displacement of LVDT 3 (Figure 3-6b). The displacement of LVDT 3 was gradually increased at a rate of 5 mm/min to ensure that strain rate would not affect the mechanical properties of the USP material (Bruneau et al., 2011). To measure the strain where the first PH is expected to develop, two Strain Gauges (SG) were placed on outer and inner surfaces of the east specimen (Figure 3-6c), precisely at the midpoint of the bent. Non-contact strain field measurements using Digital Image Correlation (DIC) system were also employed to monitor the left specimen on its front face and outer curved surface (correlatedsolutions, 2018).

3.3.3 Loading procedures

Figure 3-7 illustrates the loading protocol created as a function of the scissor displacement Δ , normalized to the inner fuse diameter, D . The specimens were tested by imposing the cyclic displacement history prescribed by FEMA 461 (FEMA; & ATC, 2007), which consisted of 26

progressively increasing cycles to achieve a maximum displacement of 6 mm measured between the legs, which corresponds to a 3% storey drift angle in a three-storey hybrid steel-timber structure consisting of chevron steel braced frame as the SFRS and CLT panels, glulam beams and columns as the gravity load-resisting system (Mowafy et al., 2021). USP specimens would act as seismic fuses in glulam beam-to-steel column joints in the prototype structure selected to develop the loading protocol. The FEMA 461 displacement history proceeded with 10 additional displacement cycles to attain a maximum normalized scissor displacement of 20%, equivalent to a net displacement of 20 mm between the legs. This displacement corresponds to a 10% storey drift angle in the same prototype structure. Note that the maximum displacement that could be applied due to laboratory constraints was 25 mm, as the bolts used to connect the specimen would touch each other beyond this displacement.

3.4 Experimental results

The results of four cyclic quasi-static tests, including hysteresis response, plastic mechanism, stiffness degradation, ductility, and energy dissipation capacity, are discussed in this section to provide understanding on the seismic behaviour of U-shaped steel specimens. In particular, hysteresis response and backbone curves shed light on energy dissipation and deformation capacities. Stiffness degradation provides insight into how failure modes affect specimen behaviour, while the plastic mechanism helps understand the yielding and post-yielding behaviour of UPS. Residual deformation manifests the post-earthquake response of the specimen. Finally, the energy dissipation capacity indicates how well the specimen can absorb energy during seismic events.

3.4.1 Hysteresis response

Normalized force-displacement responses of Specimens S1 to S4 are shown in Figure 3-8. The left vertical axis is the force normalized by the yielding capacity in compression, which is computed based on the specimen bilinear backbone curve obtained using the equivalent energy method (Council, 1996).

All specimens reached a maximum normalized displacement of $\pm 20\%$ (Figure 3-8) without exhibiting fracture or instability. As shown in Figure 3-8, all four specimens reached approximately 120% to 130% of their yielding capacity in compression and tension, respectively, mainly due to material strain hardening. The behaviour of the specimens in compression is different from that in tension due to the difference between the effective span and boundary conditions generated under compression and tension loading conditions. The overall hysteresis responses of all specimens were identical except for S4 for which slippage and bending of the edge bolts were observed in the edge bolts during testing. This behaviour was a clear indication of the large prying action that occurred at the edge bolts as the fuse with the greatest thickness underwent excessive inelastic deformation tilting the bolt position at the maximum compression or tension load. As expected, S1 having 12.7 mm thickness, exhibited the lowest yielding capacity, while S4, with 22.2 mm thickness, reached the largest yielding capacity. S2 and S3 showed an intermediate response between S1 and S4.

3.4.2 Plastic mechanism

Figure 3-9 shows a bird-like disaggregated force-displacement response of S1 at the point where the maximum displacement reached 20 mm (loading cycle 35). Eight critical points, *a* to *h*, along the curve, were chosen to evaluate the local strain and stress responses. During each cycle, the specimen was first loaded in compression and then loaded in tension.

Referring to Figure 3-9, at point *a*, a gap developed between the load-distributing plate and the leg of the fuse due to residual deformations accumulated from previous plastic cycles. As the specimen approached point *b*, this gap started to close, and complete contact was reached between the test fixture and the fuse leg, which increased the scissor stiffness between points *b* and *c*. At point *c*, three PHs (see Figure 3-9a) formed in each USP, creating a full-yielding mechanism. The path between points *c* and *d* was dominated by material strain hardening. Beyond point *d*, unloading began, which consisted of two paths, *d-e* and *e-f*. The former path exhibited a higher stiffness because of the full contact between the specimen and loading plates. However, the stiffness started to decrease gradually as we approach point *f*, where a noticeable gap was observed between the fuse leg and the test fixture. As the specimen started to pick up tension loads (path *f-g*), PHs formed at slightly different locations due to the same nonlinear plastic mechanism (i.e., flexural yielding). PHs in the legs moved toward the anchorage bolts owing to the fact that the load transfer in tension is through the bolts and not plate bearing. Noticeable strain hardening occurred within paths *f-g*. Unloading in tension started at point *g* and ended at *h* at which a relatively large residual deformation occurred in the specimen. Similar disaggregated hysteresis response was extracted for the remaining specimens, S2, S3, and S4, which confirmed an almost identical hysteresis response and plastic mechanisms in tension and compression cycles as those described for S1. Note that the hysteresis response of S4 was affected by bolt slippage that took place when testing this specimen.

To investigate the sequence of PH formations in tension and compression, we examined photographs of the specimens before testing and at the end of the test as shown in Figure 3-10. Testing S1 and S3 involved the loading protocol that ended after reaching the maximum displacement in tension. However, an additional half cycle was applied in S2 and S4 to reach the

maximum displacement in compression. We then unloaded the specimens to observe residual deformations.

Referring to Figure 3-10, the deformed shapes of S2 and S4 show in-plane rotations at points 2 and 3, representing the location of active PHs when the distributing horizontal plate is engaged under compression. Similarly, in-plane rotations at points 4 and 5 were observed in S1 and S3, which indicate the location of active PHs when the bolts near the plate edge effectively secured the terminal portion of the fuse leg, thereby preventing it from detaching from the distributing horizontal plate.

3.4.3 Stiffness degradation and ductility

Stiffness degradation and ductility of the specimens are analyzed here through the specimens' backbone curves. The force and displacement values at yield were first determined. Figure 3-11 shows the backbone curves of S1 – S4 presented as the normalized force – normalized displacement response, which were generated by connecting the peaks of the hysteresis curves in Figure 3-8. All four specimens exhibited almost identical behaviour. Yielding occurred at approximately $5\%D$ during compression loading. The specimens reached 120% to 130% of the compressive yielding capacity at the maximum normalized scissors displacement ($20\%D$), suggesting the influence of material strain hardening on the post-yield response of the fuse. In tension, the nonlinear response of the specimens was slightly different than that observed in compression, creating asymmetric force-deformation response (Figure 3-11), in particular, in the initial elastic region. The specimens reach their tensile yielding capacity at approximately $5\%D$, on average and experienced 130% to 140% of their tensile yielding capacity at the maximum normalized scissors displacement ($20\%D$).

Table 3-1 summarizes the quantitative response parameters, as obtained from the backbone curves of Figure 3-11 for the USP specimens. A consistent yield at around 5% displacement relative to the inner diameter of the U-shaped fuse was observed in all specimens, both in compression and tension. In compression loading, the yielding load ranged from 114 to 350 kN, while the ultimate load, influenced by strain hardening, ranged from 143 to 453 kN. Under tension, the yielding and ultimate loads varied between 78 and 263 kN, and between 105 to 356 kN, respectively. Furthermore, the specimens exhibited higher stiffness in compression due to engagement of distributing plates.

3.4.4 Energy dissipation capacity

The amount of hysteretic damping used here as a measure of the energy dissipation capacity of USP fuse is determined by calculating the area underneath force-displacement hysteresis loops. The cumulative energy as a function of the cumulative displacement of each specimen is plotted in Figure 3-12a. As shown, the energy dissipation capacity of the specimens is increased as the fuse thickness increases, e.g., 60% increase in energy dissipation capacity per 3 mm increase in thickness, except for S4. Bolt slippage observed when testing S4 affected the energy dissipation capacity of this specimen, e.g., only a 10% increase was observed for S4 (with 22 mm thickness) at large displacement demands ($20\%D$) as compared to S3 (with 19 mm thickness).

The amount of energy dissipated per cycle in the specimen is presented in Figure 3-13b. Limited energy dissipation capacity was observed during the early cycles, e.g., displacement cycles below 6% cycle, but the energy dissipation capacity exponentially increased beyond yielding as expected. Notably, relatively smaller energy dissipation capacity was achieved in the second cycle of each set of identical inelastic cycles, mainly due to the permanent deformations introduced in the first cycle.

3.5 Numerical modelling of USP plastic mechanism

Finite element analysis was used to evaluate the nonlinear plastic mechanism of USP fuse. The development and validation of the finite element model are first described, followed by the evaluation of the plastic mechanism of USP in conjunction with the proposed analytical model described in Section 3.2, which can be used to size USP in practice.

3.5.1 Finite element model

A two-dimensional (2-D) finite element model (FEM) of USP specimens was developed using the COMSOL Multiphysics software package (Multiphysics, 2015). Only one-half of the specimen pairs were simulated, assuming full symmetry with respect to Y-axis, as shown in Figure 3-13a. The 2-D plain strain modelling technique was selected in this study because the deformation of the specimens out-of-plane is deemed to be negligible, as confirmed by experiments. Moreover, this technique yields a computationally-efficient numerical simulation. To mimic the boundary conditions considered in the test setup, the lower plate was fixed while the upper one was free to move. The guided support on the right was added along the right edge of all elements to represent a symmetric boundary condition.

The fuse specimens were modelled using eight-node quadratic quadrilateral elements. The Voce-Chaboche (de Castro e Sousa et al., 2020) constitutive model was used to properly capture the nonlinear cyclic response of the fuse material. Material plasticity was defined using parameters including the initial yield stress (σ_{y0}), isotropic saturation hardening (Q_{∞}), isotropic hardening rate (b), dynamic recovery strength (c_1), and dynamic recovery exponent (γ_1). These parameters were obtained following the approach proposed by Sousa et al. (Castro e Sousa et al., 2021) using

the monotonic coupon test data. The modulus of elasticity (E) along with material plasticity parameters are given in Table 3-2 for the four specimens.

Six-node quadratic triangular elements were used to simulate the test fixture plates with linear elastic isotropic material. Based on sensitivity analyses performed prior to the analysis, the appropriate mesh size for the model was found to be approximately 1/8 times the plate thickness. The mesh size for the contact areas between the fuse and distributing horizontal loading plates as well as the fuse and bolts (Figure 3-13b) was selected to minimize strain concentration while avoiding numerical convergence issues. Contact interaction was modelled between the legs of the U-shaped fuse and either of the testing fixtures and the bolt nuts at all surfaces where contact is possible using penalty method. To reproduce the actual stiffness of the bolts, an effective area of the bolt, with a diameter equal to the nominal diameter of the bolt and a thickness equal to that of the distributing horizontal plate, was modelled. A full contact surface was used between the upper and lower sides of the bolt head and nut, whereas bolts are free to move in the vertical direction.

The residual stresses developed in USP fuses during the bending process were introduced in the numerical model using the distribution proposed by Moen et al. (Moen et al., 2008) and apply it among the fuse bent and the fuse legs. The proposed distribution considers both the built-in stresses produced during plate manufacturing and those induced due to cold-working, which agrees well with the history of residual stress development in USP specimens. Geometric nonlinearity was considered in the analysis using large displacement theory, which accounts for the changes in stiffness and load amplification due to $P-\Delta$ effects (Ted Belytschko et al., 2014).

3.5.2 Model validation

To validate the numerical model of the fuse, particularly the asymmetric hysteresis response observed in the tests, the force-displacement response of each specimen from the test was compared to that predicted by the FEM developed here. Figure 3-14a – 14d compares the cyclic response obtained from the numerical simulation against the findings from experimental testing for S1, S2, S3 and S4, respectively. An excellent agreement was achieved between the numerical and experimental hysteresis responses. In particular, the elastic and post-yield stiffness, stiffness degradation, ultimate compressive and tensile forces are appropriately reproduced. Moreover, the proposed numerical model can predict the asymmetric response observed in the test.

Minor differences between the numerical simulation and test results can be attributed to the steel plasticity model assumptions, e.g., maximum number of backstresses (Castro e Sousa et al., 2021), assumed residual stress distribution, variations in boundary conditions, three-dimensional effects and the limitations associated with the plain strain modelling technique. Overall, the numerical model of the specimens can appropriately predict their nonlinear cyclic response. In addition to the force-displacement response, cumulative energy at the end of the test (associated with 20%*D*) was compared. Cumulative energy of S1, S2, S3 and S4 from the test are 72, 127, 188, and 211 kJ, respectively, which agree well with those predicted by the FEM, 84, 141, 204, and 247 kJ, respectively.

The local response of the second specimen at the 20% normalized displacement cycle, as obtained from the test and numerical simulation, is shown in Figure 3-15. In this Figure, the vertical strains of the front face of S2 obtained during the test using the DIC system were visually compared to the first principal strain computed using the FEM at critical points associated with the hysteresis response, *a*, *b*, *d*, and *g*. Despite a very complex stress and strain distributions in USP under cyclic

loading, a very good correlation was found concerning the overall fuse deformed shape and the locations of PHs.

3.5.3 USP yielding capacity and stiffness

The yielding capacity of USP obtained from the finite element analysis and the proposed analytical model are evaluated in Figure 3-16a and 3-16b when the USP is in compression and tension, respectively. Both models demonstrated a good agreement versus the experimental data, with the numerical model offering slightly higher predictions in both compression and tension loading cycles. The proposed analytical model predicted relatively lower yielding capacity, likely due to concentrated plasticity assumption and neglecting nonlinear cyclic hardening. When comparing the stiffness of USP (Figure 3-16c and 3-16d), the results of numerical simulation match well the test results, while the proposed analytical model showed appreciably higher predictions, particularly when the fuse is subjected to compression. The discrepancy observed in compression between the analytical model and the test is primarily due to residual stresses, which is expected to negatively affect the stiffness of USP in compression due to high compressive residual stresses present in the bent USP. Hence, a reduction factor has been introduced into Equation 3-2 to consider the influence of residual stresses on the compressive stiffness of the fuse. The modified equation is given as follows:

$$K = (6/5)R_F(EI/l^3) \quad \text{(Equation 3-4)}$$

Where R_F represents the reduction factor, which has been determined through the assessment of average discrepancies between the analytical model and experimental results, and it is set at a value of 0.383.

3.6 Summary and conclusion

The cyclic behaviour and plastic mechanism of U-shaped steel plate fuses undergoing scissor bending were evaluated in this paper through an experimental program and numerical simulation. USP fuse was first introduced. Four specimens, each with a unique thickness, were tested experimentally under cyclic loading. An analytical model to determine the stiffness and plastic capacity of USP was proposed. Moreover, a plane strain finite element model of USP was constructed to simulate its nonlinear cyclic response and examine its plastic mechanism. The key findings of this paper are summarized as follows:

- Scissor bending, a deformation process where the load is transferred perpendicularly to the fuse leg, was identified as a key indicator of inelastic response of U-shaped steel plate under transverse loads. The degree of scissor bending was found to be largely influenced by compression or expansion of the bent sections of the plate.
- USP specimens yielded on average at 5% scissor displacement (D) of the inter diameter of the USP, where scissor displacement refers to the change in distance between the legs of the U-shaped steel plate under load. The specimens sustained a deformation demand of $20\%D$, which corresponds to a storey drift of 10% in a three-storey hybrid steel-timber structure, without unsatisfactory limit states (e.g., instability or fracture), which confirms their potential to safely dissipate seismic loads.
- The cyclic behaviour of USP specimens in compression and tension presents a noticeable asymmetry due to uneven effective spans and contact lengths present under compression loading. This asymmetry is largely attributed to the lower stiffness observed under tension

loading. The tension yielding capacity averages to about 70% of the compression yielding capacity. Influenced by material strain hardening, specimens reached 120-130% of their initial compression yielding capacity and 130-140% of their initial tension-yielding capacity at 20%*D* deformation demand.

- The proposed finite element model can well reproduce the nonlinear cyclic behaviour of USP and can be used in future for developing design guidelines for seismic force-resisting systems benefiting from the proposed USP.
- The proposed analytical model, effectively predicting yielding capacity (e.g., 88% of the actual capacity) and stiffness of USP, offers a practical tool to determine the preliminary geometry of USP in design.

This study demonstrated the potential of USP with scissor bending to be used in steel, timber, or hybrid seismic force-resisting systems, such as beam-to-column connections of steel-timber hybrid SFRSs, beam-to-column connections of timber moment-resisting frames, and braces in steel or timber braced frames. Future research should prioritize exploring residual stress distribution and devising strategies to mitigate their impact, thereby enhancing the fuse stiffness in compression. Additionally, refining the proposed analytical model for more accurate stiffness prediction is key. Finally, additional experimental testing should be conducted to examine the influence of USP dimensions on its cyclic behaviour.

Notation

The following symbols are used in this chapter:

USP = U-shaped Steel Plates

VWM = Virtual Work Method

PH = Plastic Hinge

SFRS = Steel-timber hybrid seismic force-resisting system

LVDT = Linear Variable Differential Transformer

DIC = Digital Image Correlation

SG = Strain Gauge

R_{cl} = Bent centerline radius of the USP

L = Leg length of the USP

L_c = Contact leg length of the USP

L_f = Free length of the USP

P = Force required to open or close the scissor mechanism

Δ = Scissor displacement in the vertical direction

M_A, M_B = Moments at points A and B, respectively

l' = Horizontal distance between points A and B (effective span of USP)

K = Flexural stiffness of the fuse

E = Modulus of elasticity

EI = Product of the modulus of elasticity (E) and the moment of inertia (I) of the USP

P_{cy} = Compressive yielding capacity of USP

w = Width of the fuse out-of-plane

t = Plate thickness of the USP

F_y = Yield stress of the steel material

F_u = Tensile strength

ξ = Eccentricity factor

P_{ty} = Tensile yielding capacity of the fuse

$L_{c,ten}$ = Contact length in tension

$L_{c,comp}$ = Contact length in compression

$L_{f,ten}$ = Free length of the fuse in tension

$L_{f,comp}$ = Free length of the fuse in compression

l'_{ten} = Effective span in tension

l'_{comp} = Effective span in compression

σ_{y0} = Initial yield stress

Q_{∞} = Isotropic saturation hardening

b = Isotropic hardening rate

c_1 = Dynamic recovery strength

γ_1 = Dynamic recovery exponent

Table 3-1 Test specimens monotonic response parameters.

Specimen	Elastic stiffness [kN/mm]	Displacement at Yield / D [%][*]	Yield Load [kN]	Ultimate load [kN]^{**}	Ultimate Load / Yielding Capacity [%]
Loading in Compression					
S1	22	5.2	114	143	125
S2	37	5.0	188	231	122
S3	58	5.0	290	352	121
S4	70	4.9	350	453	129
Loading in Tension					
S1	16	4.8	78	105	135
S2	20	5.1	132	173	131
S3	39	4.8	192	251	131
S4	53	4.9	263	356	141

*D is the inner diameter of the U-shaped fuse bent.

**Ultimate load is the maximum load recorded at the last cycle of the test.

Table 3-2 Voce-Chaboche material model input parameters.

	S1	S2	S3	S4
E [GPa]	187	190	205	182
σ_{y0} [MPa]	368	328	350	326
Q_{∞} [MPa]	58	28	29	33
b	0.51	0.42	0.36	0.66

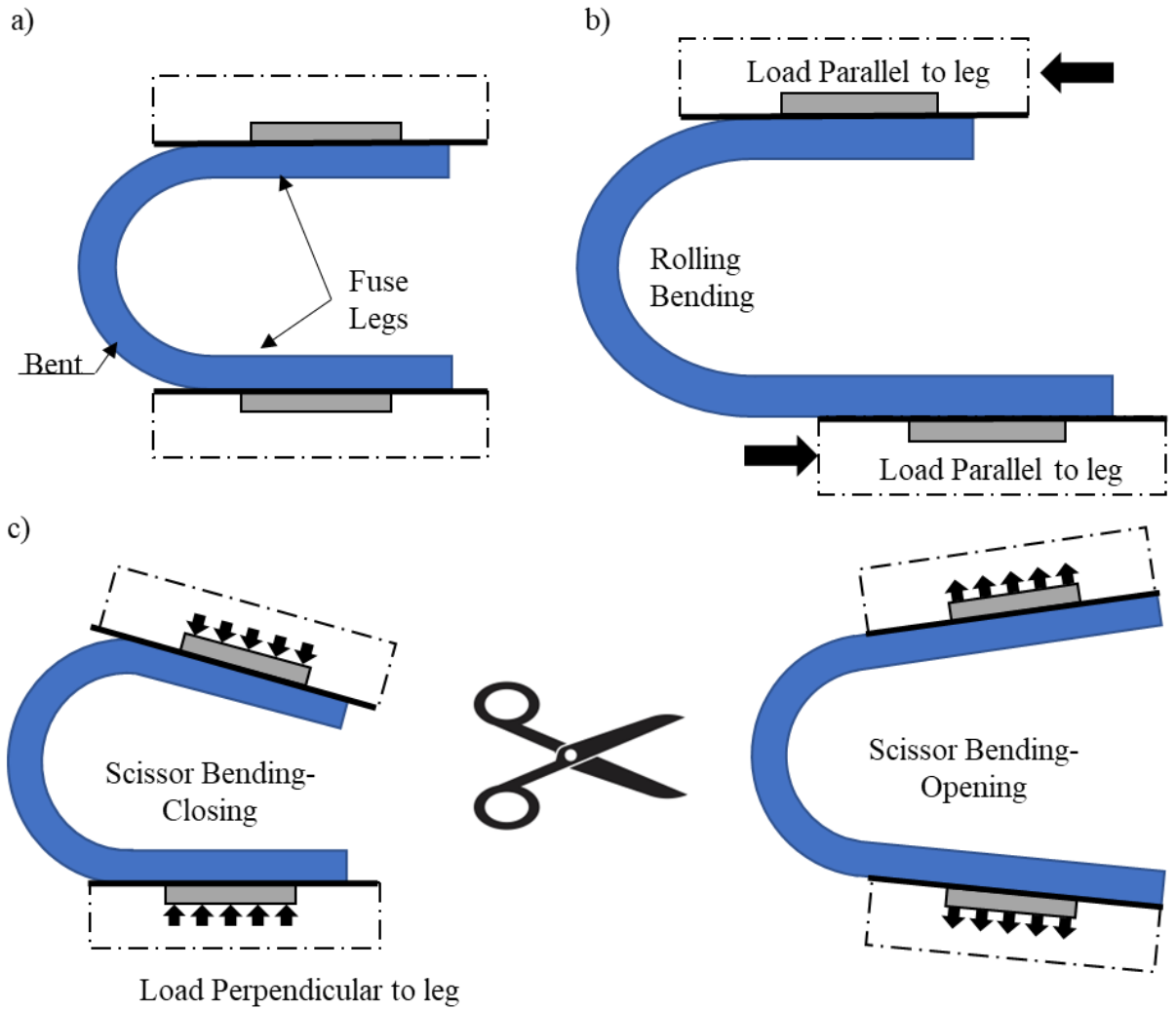


Figure 3-1 U-shaped Steel Plate: a) components; b) rolling bending mechanism; c) scissors bending mechanism.

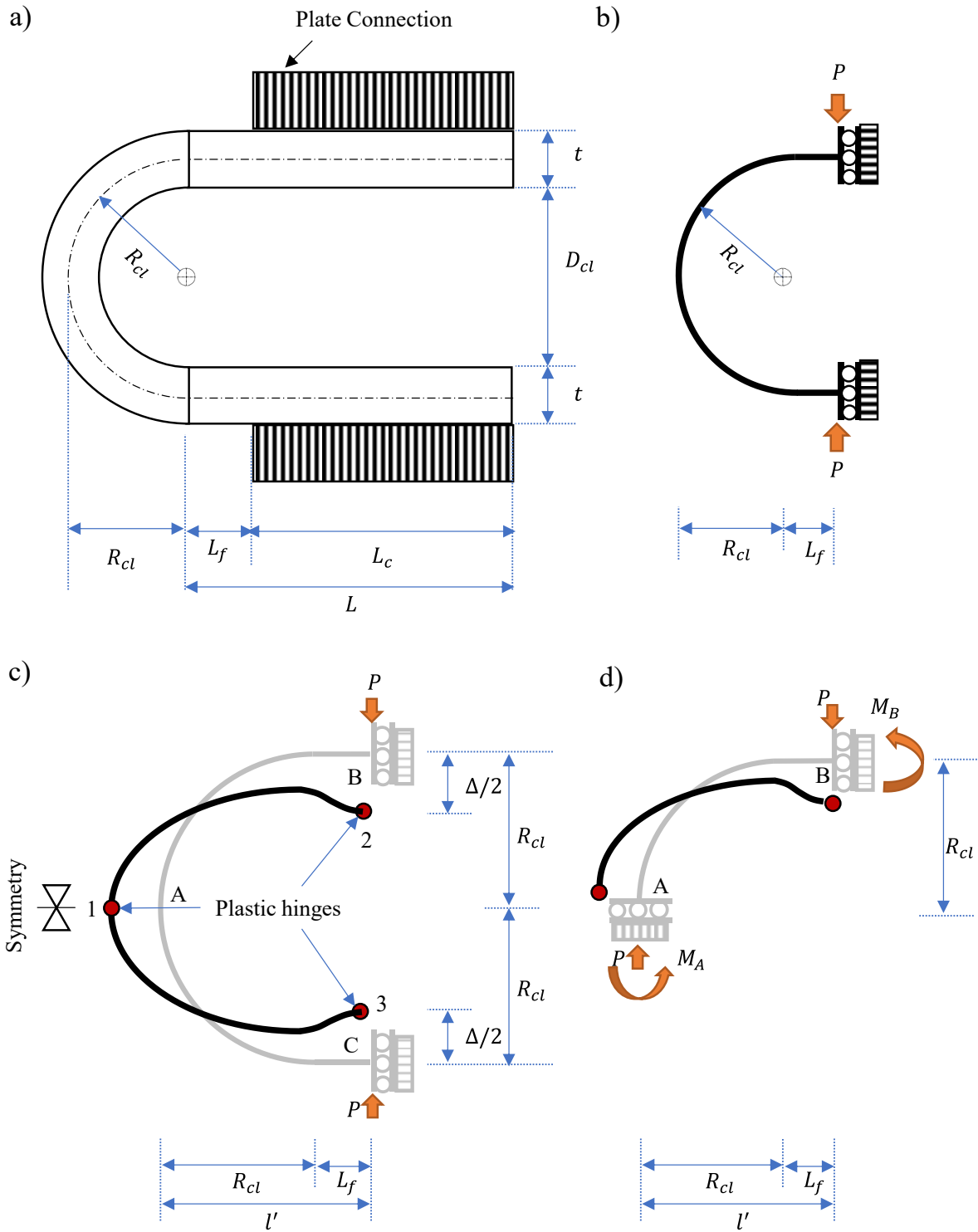


Figure 3-2. Scissor bending mechanism: a) USP geometrical properties; b) simplified analysis model; c) full USP; d) half unit.

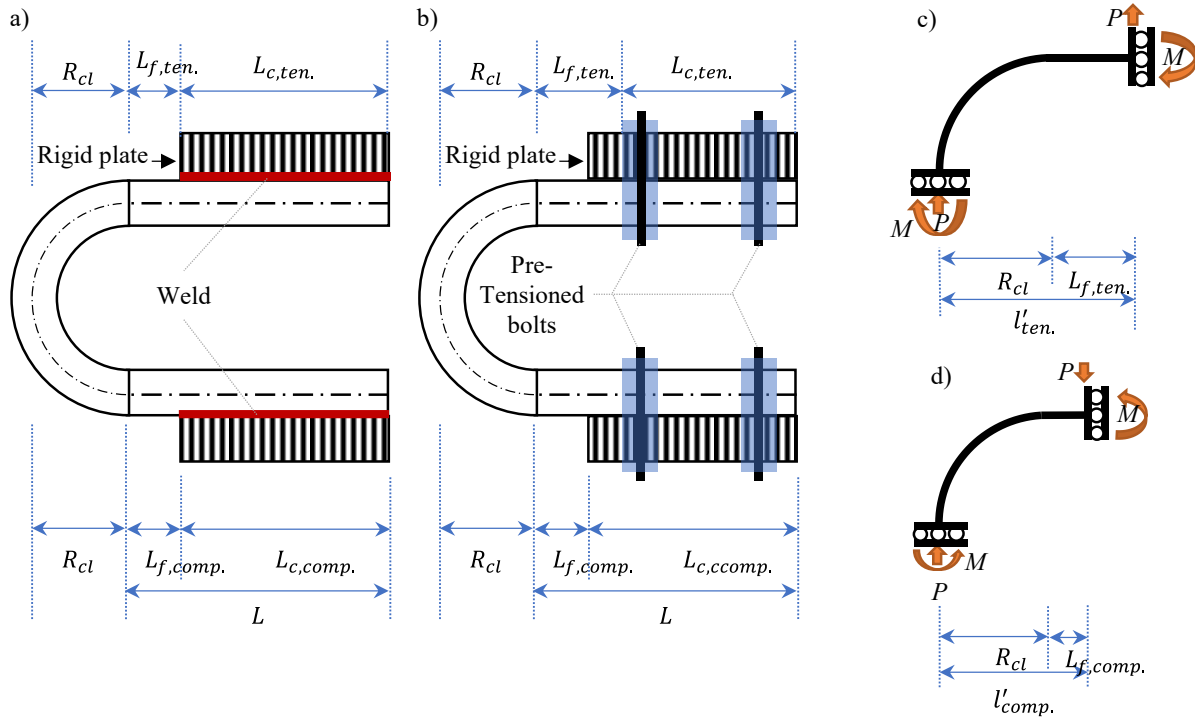


Figure 3-3. USP effective span (l'): a) welded connection; b) bolted connection; c) Analytical model in tension; d) Analytical model in compression.

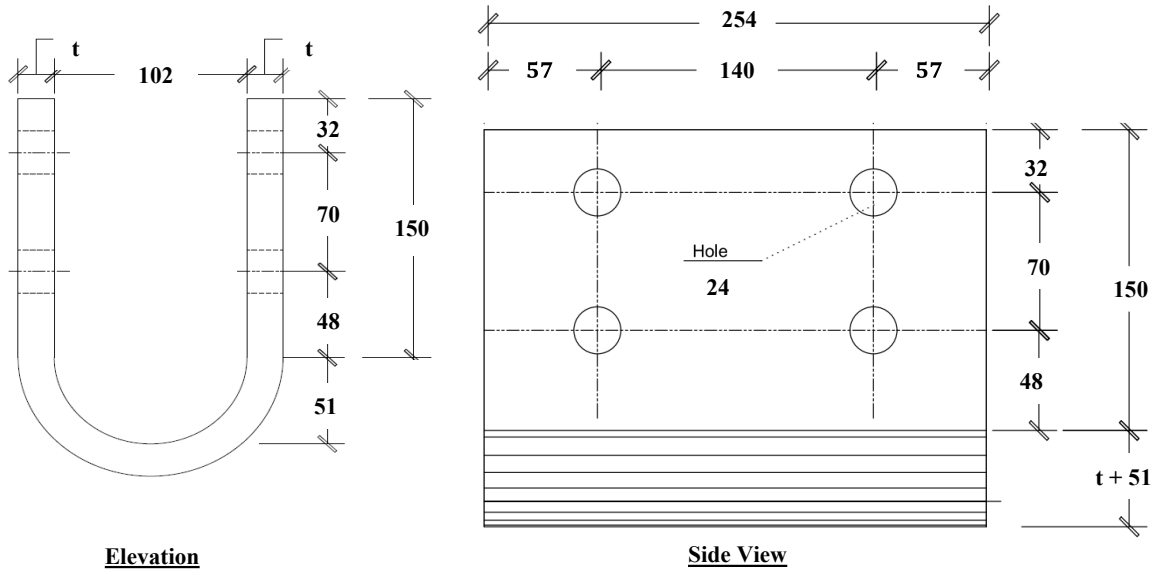


Figure 3-4. Typical geometry of USP specimens (dimensions in mm).

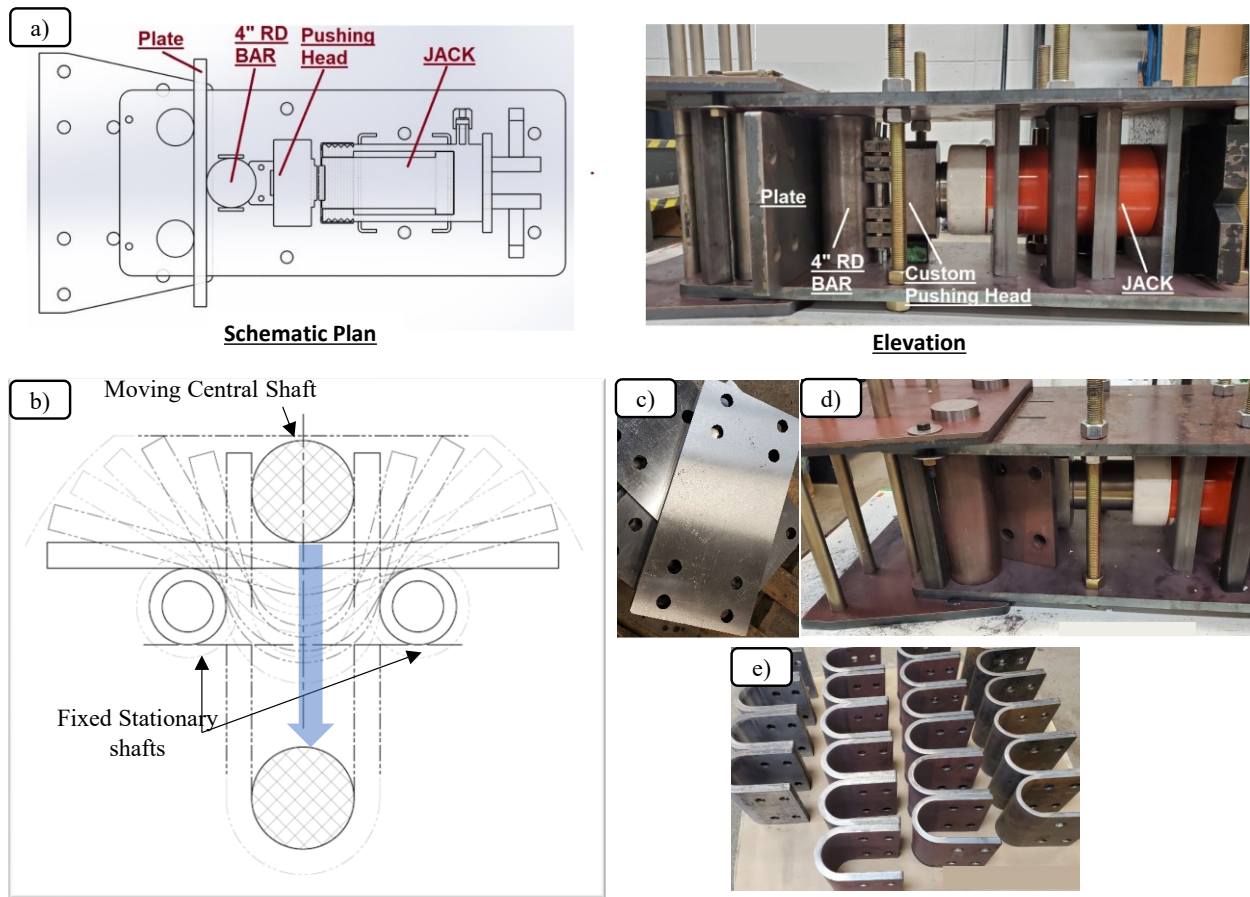


Figure 3-5. USP bending process: a) custom-developed bender; b) bending mechanism; c) blank profile; d) plate bending process; e) final USP products.

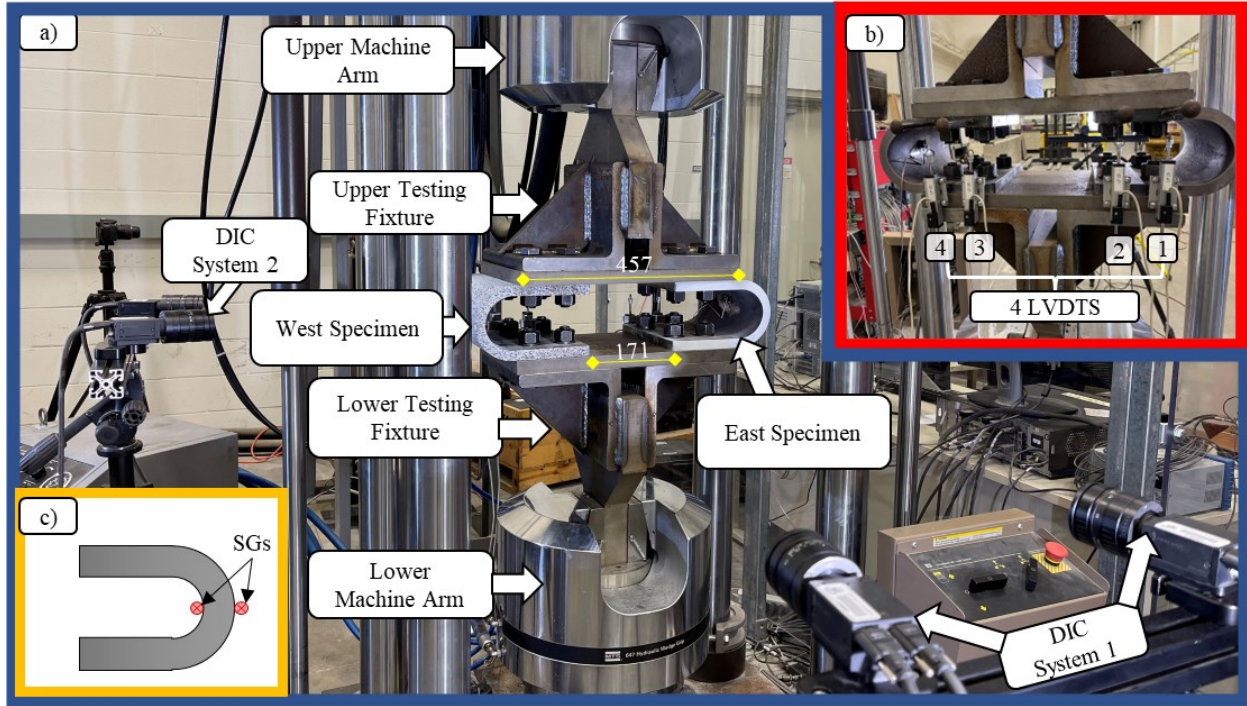


Figure 3-6. a) Test specimen and setup; b) LVDT positions (back of the specimen); c) strain gauge locations on East Specimen.

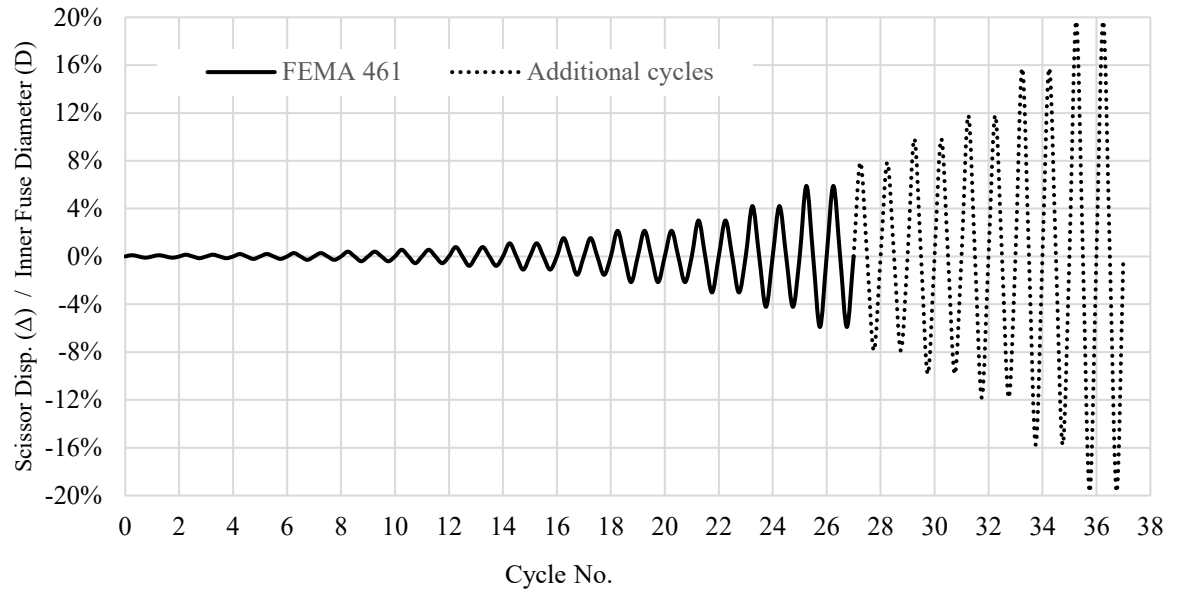


Figure 3-7. Loading protocol adapted from FEMA 461 (FEMA; & ATC, 2007).

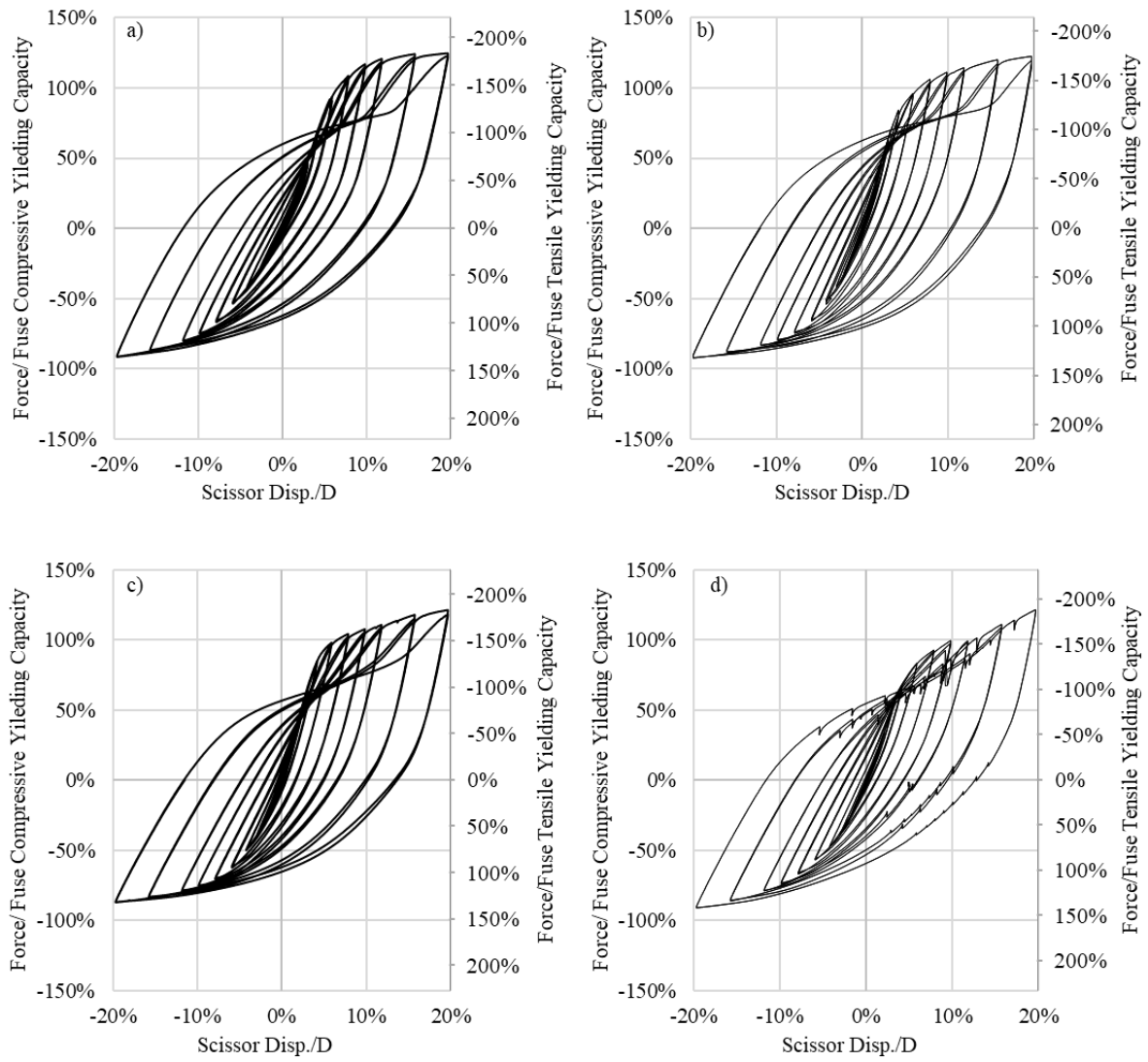


Figure 3-8. Force-displacement response: a-d) Specimens S1 – S4.

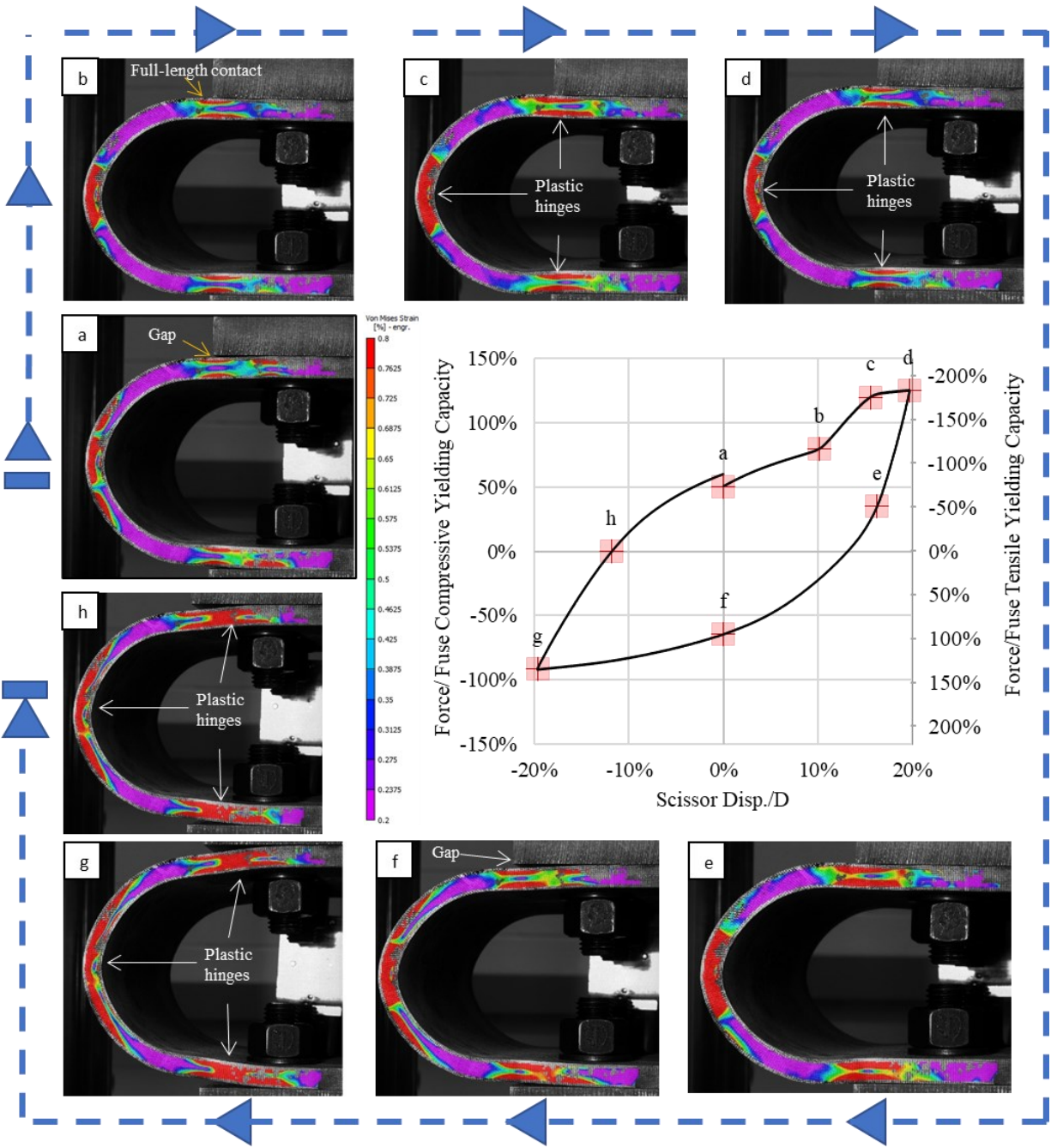


Figure 3-9. USP hysteresis response at 20%D displacement cycle and respective von Mises strains.

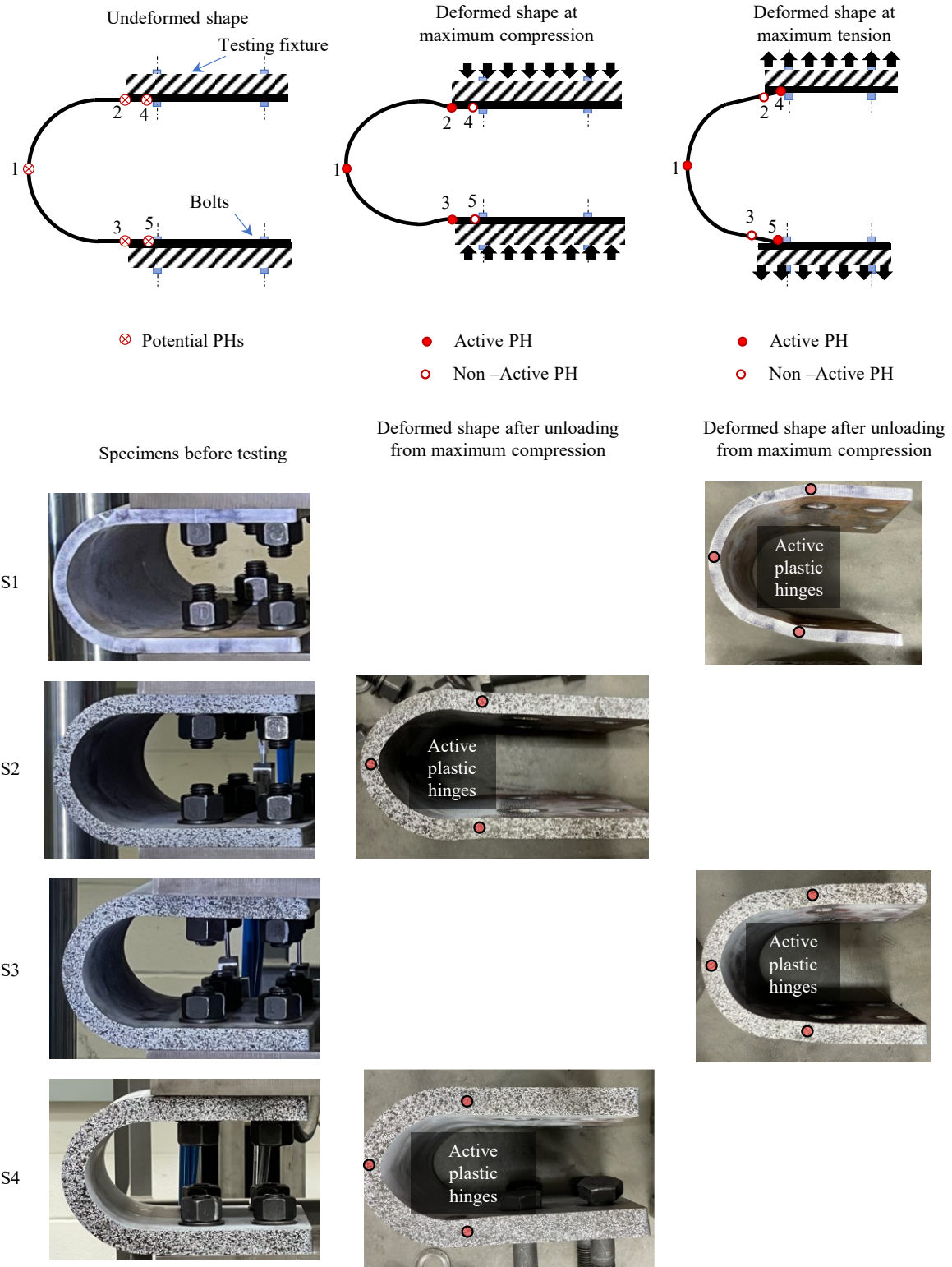


Figure 3-10. USP plastic mechanism at maximum (final) tension and compression cycles.

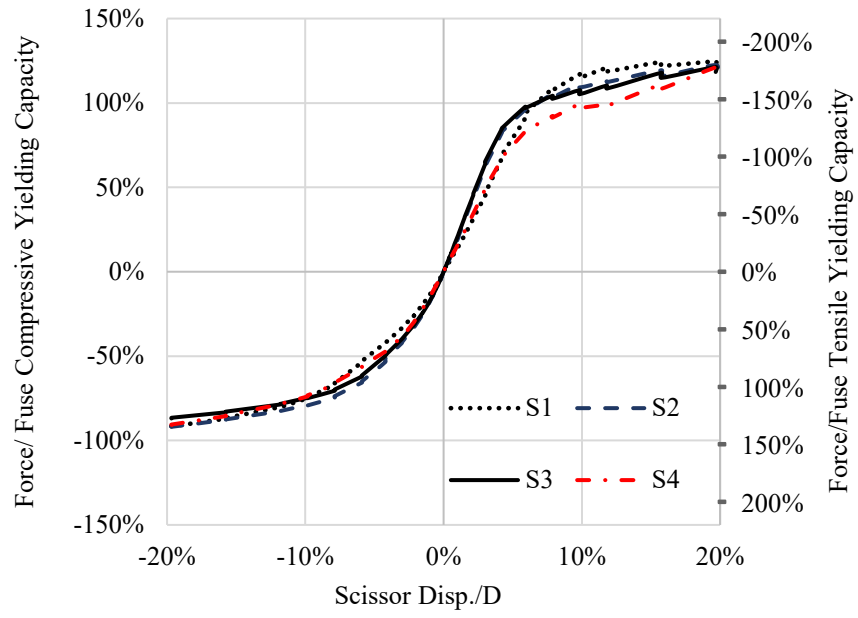


Figure 3-11. USP force-displacement (backbone) curves.

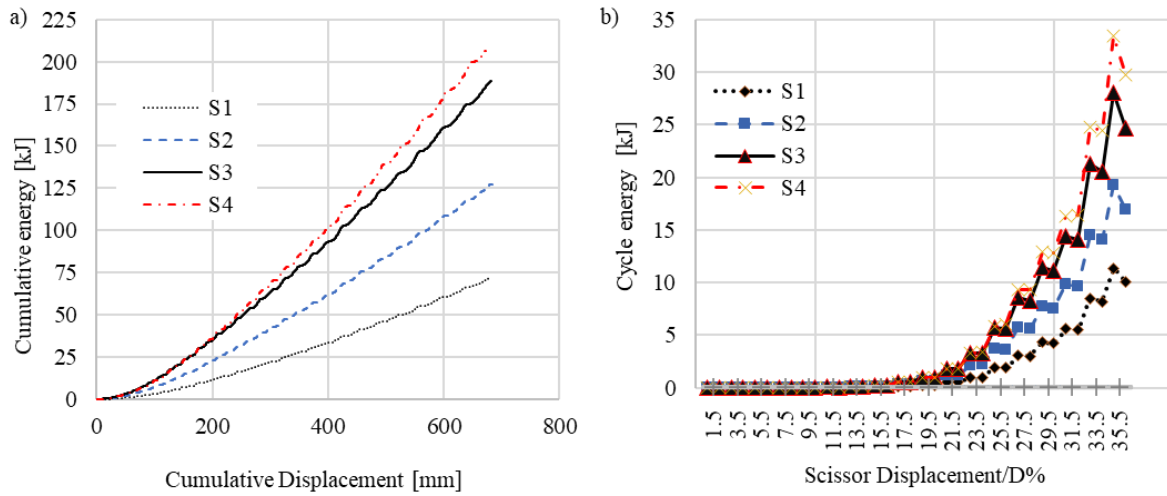


Figure 3-12. Fuse energy dissipation capacity: a) cumulative energy; b) cyclic energy.

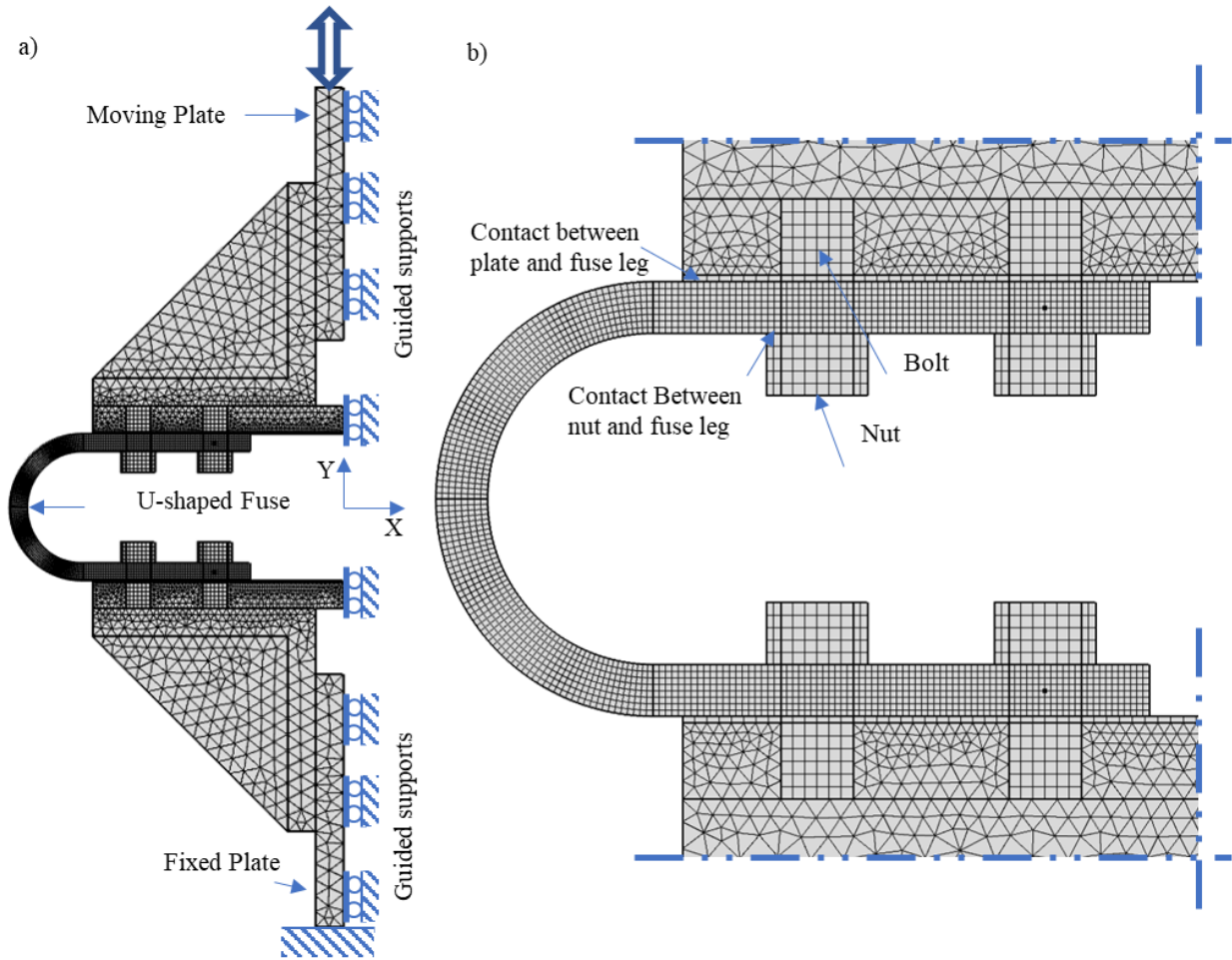


Figure 3-13. Finite element model: a) boundary conditions; b) contact areas between the fuse and the test setup.

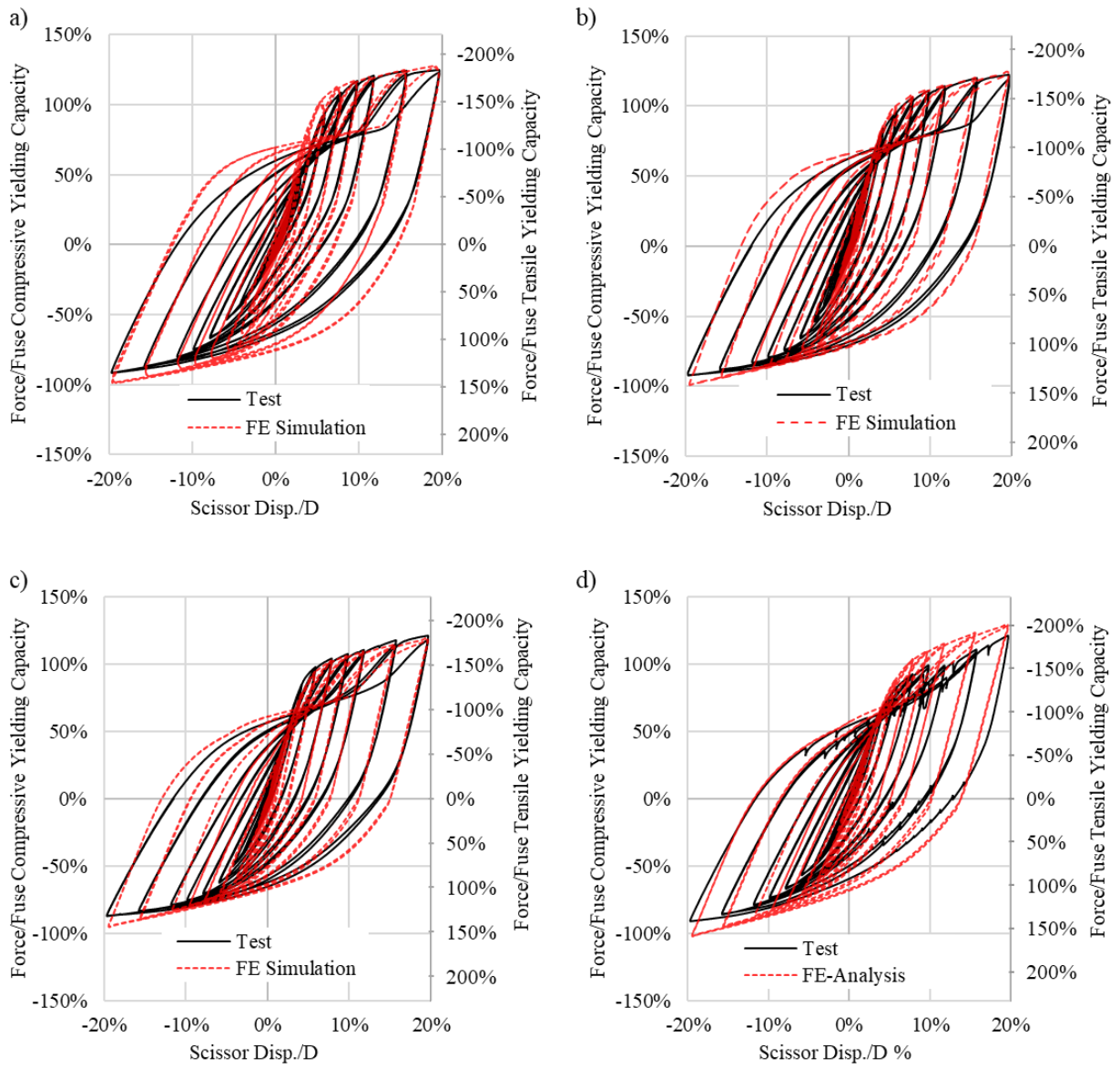


Figure 3-14. Hysteresis responses - experimental testing vs. numerical simulation: a-d) S1 – S4.

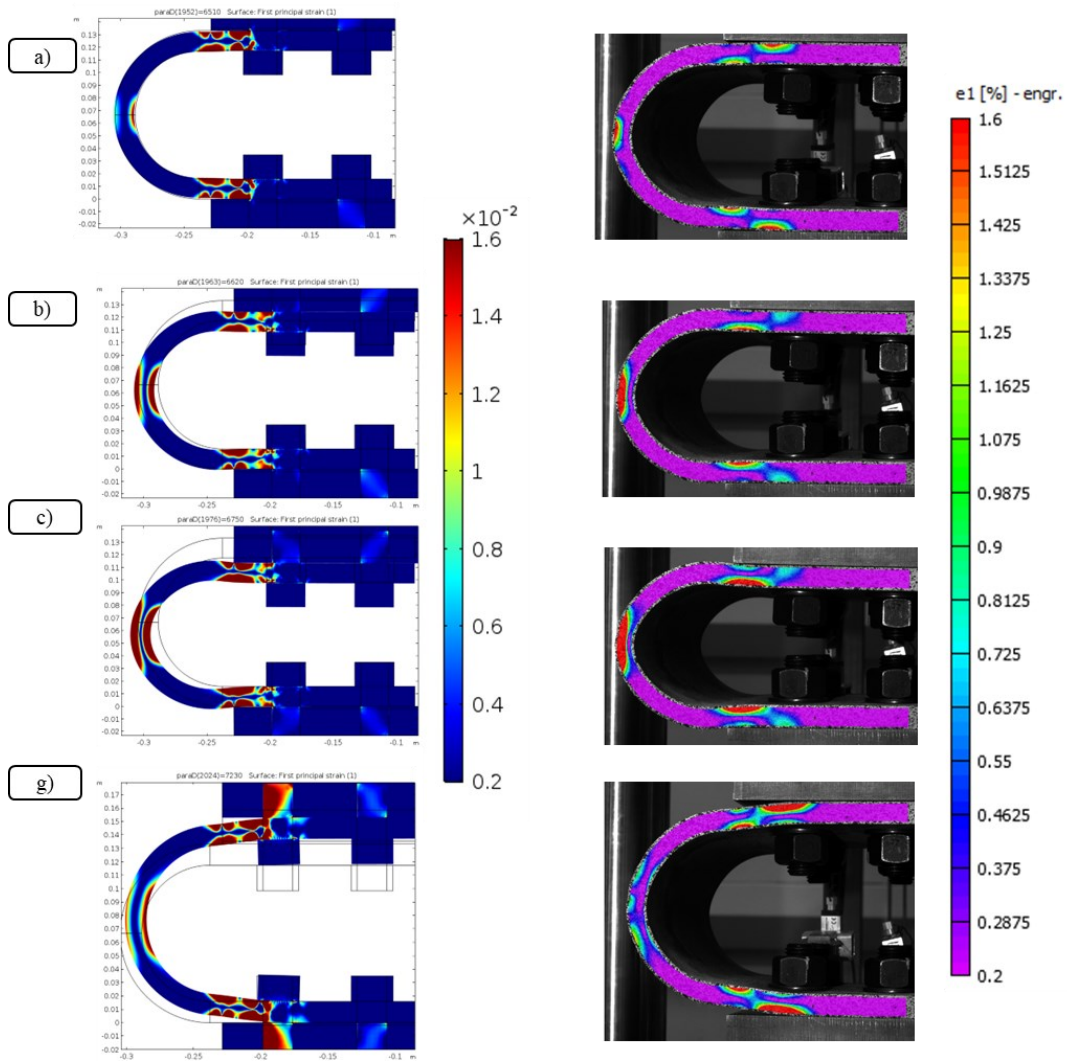
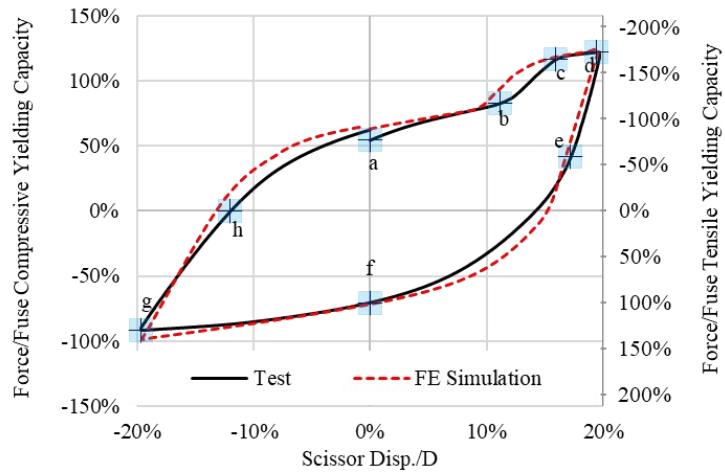


Figure 3-15. Deformed-shape and principal strain distributions at 20%D displacement cycle

(FEM on the left and test results on the right): a-c) points a-c; g) point g.

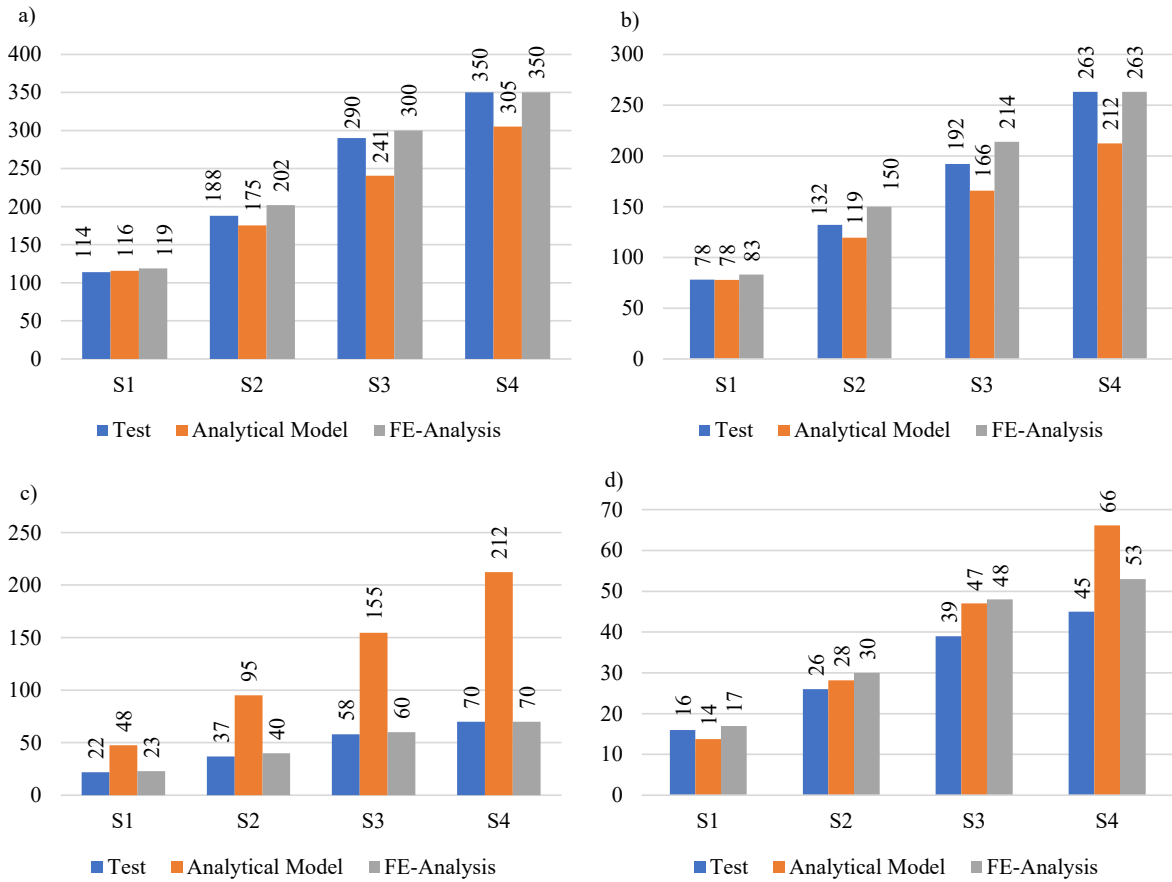


Figure 3-16. Numerical and analytical method predictions versus experimental test results: a-b) USP yielding capacities in compression and tension; c-d) UPS initial stiffness in compression and tension.

4. Development and cyclic testing of a hybrid timber-steel beam-to-column connection with replaceable U-shaped fuses*

4.1 Introduction

The combination of timber with other materials, such as steel, can result in improved structural efficiency under seismic loading as timber contributes to reducing self-weight of the structure while steel provides robust system ductility as a seismic fuse. This advantage is especially pronounced when steel is utilized in the joints developing seismic force-resisting systems (SFRSs) with concentrated and potentially replaceable seismic fuses. One example of such connections is the beam-to-column connection in frame structures.

Several innovative connections have been proposed in the past, mainly for the application in timber SFRSs, including nailed steel side-plate connections (Bryant et al., 1981) and bolted slotted-in steel plate connections (Cao et al., 2022; M. He et al., 2017), which lack ductility under seismic loading. To enhance the ductility capacity of such connections, bolted slotted-in steel plate connections reinforced with self-tapping screws (Lam et al., 2010) and bolted beam-to-column glulam connections reinforced with locally cross-laminated glulam members (Wang et al., 2015) have been proposed. Buchanan and Fairweather showed that Rods glued parallel to the grain can also introduce ductility in end-roof and multi-storey connections (A. H. Buchanan & Fairweather, 1993). Despite past efforts to improve ductility of connections in timber structure, the majority of these connections still suffer brittle failure modes, such as splitting, parallel-to-wood-grain shear cracks, or shear and tension failure. Andreolli et al. proposed using a combination of wood, steel, and glue to improve ductility (Andreolli et al., 2011). Yang et al. proposed a connection method

* The content of this chapter is being prepared and will be submitted as a journal manuscript.

using steel boxes, rods, and bolts with glulam beams and columns (Yang et al., 2016). In addition, He and Liu found that using dowel-type fasteners (such as plain round rods or self-tapping screws) as reinforcement in bolted connections can change the failure mode from brittle to ductile, improving ductility capacity and mitigating wood splitting (M. J. He & Liu, 2015). Iqbal et al. (Iqbal et al., 2010) confirmed that prestressed timber beam-column connections exhibit minimal residual deformations and damage under seismic loading. Ottenhaus et al studied how to design connections in buildings to better withstand earthquakes by improving their ductility (Ottenhaus et al., 2021). A hybrid steel-timber moment connection with replaceable steel links was proposed by Gohlich et al. (Gohlich et al., 2018) allowing the system to recover efficiently after a major seismic event. Although, timber structures can benefit from hybrid steel-timber connections, the methodology can be extended to the system level (Mowafy et al., 2021) where the SFRS of the structure consists of a stiff and ductile steel structure, while a light timber gravity load-resisting system (GLRS) is used to carry vertical gravity loads while transferring the inertia forces to the steel SFRS. An example of such hybrid timber-steel systems is a timber beam-to-steel column joint utilizing steel angles connected to the glulam beam through long steel bolts (Sirumbal-Zapata et al., 2019). This study presents a resilient glulam beam-to-steel column connection with replaceable U-shaped steel seismic fuses for hybrid timber-steel structural systems consisting of a timber GLRS and a steel concentrically braced frame. The development and experimental evaluation of the proposed hybrid connection are discussed in this paper.

4.2 Proposed Connection

4.2.1 Connection Components

The proposed timber beam-to-steel column connection is shown in Figure 4-1a. The connection consists of a mild steel pin connector and two U-shaped steel plates, which are attached to a glulam beam using bolts, an end T-plate with embedded knife plates, and self-drilling dowels (SDDs). The U-shaped plates are intended to provide ductile failure mechanism under large inelastic deformation due to seismic loading, thereby reducing the risk of brittle failure in the wood. Bent U-shaped plates were selected as they can offer excellent inelastic characteristics, e.g., high energy dissipation capability and fatigue resistance under cyclic loading (Baird et al., 2014; Priestley, 1996), ease of installation and potential replacement capability after a major quake. Steel U-shaped plates have been used as a seismic fuse in a variety of applications, including coupling shear walls (A. Iqbal et al., 2007), connecting post-tensioned timber walls to column-wall-column systems (Sarti et al., 2014), and metallic dissipators and seismic dampers (Qu et al., 2019). They are also used as connectors between the braces to dissipate energy in steel braced frames (Henriques et al., 2019b; Taiyari et al., 2019). Under cyclic loads, the anticipated inelastic mechanism involves rolling-bending or scissor-bending as shown in Figure 4-1a (Mowafy et al., 2023). Rolling bending dissipates energy through the elongation and shortening of the legs of the U-shaped plate as relative motion is directed parallel to them. In contrast, scissor-bending occurs when the load is perpendicular to the legs of the U-shaped plate. Most of the applications listed earlier used the rolling bending mechanism, while the proposed connection here benefits the scissor bending mechanism, which is deemed preferable in beam-to-column connections dissipating seismic-induced energy through flexural bending as kinematic response of scissor bending directly translates to expected deformation demands under seismic loading in a beam-to-column connection.

The developed connection is comprised of a mild steel pin connector and two U-shaped steel fuses, as shown in (Figure 4-1b). These elements are strategically combined to form a cohesive system that connects to a glulam beam. The pin connector serves as the central anchor, while the U-shaped steel fuses add ductility and energy dissipation. The connection to the glulam beam is achieved using bolts, an end T-plate with embedded knife plates, and SDDs. These components, including the self-drilling dowels and T-end plate connectors, are designed to simplify the installation process and eliminate alignment issues during testing, enhancing seismic resilience by enforcing ductile failure in the fuses and thus reducing the risk of brittle failure in the wood. The innovation lies in the combination of these components, considering not only mechanical strength but also practical aspects of constructability and easy on-site replacement.

4.2.2 Design Philosophy

The U-shaped steel plates resist flexural bending in the proposed hybrid timber-steel connection through the scissor-bending mechanism by inducing compression, C , and tension, T , in the upper and lower plates (under positive bending moment), respectively, while the middle pin connector transfers shear, V , to the steel column as shown in Figure 4-2a. The fuses are therefore designed to yield in tension and compression developing a robust inelastic flexural deformation in the connection, while the remaining components of the connection, including end T-plates, SDDs, and pin connector, are expected to remain essentially elastic under seismic loading. The upper and lower SDDs, and knife plates are designed to carry the probable yielding capacity of the fuse, P_u . The middle SDDs are designed to resist the accompanying probable maximum vertical shear force, V_u .

4.2.3 Yielding and probable capacities

The yielding capacity of each U-shaped fuse, P_y , is the same in tension and compression $T = C = P_y$. The probable yielding capacity of the fuse, P_{prob} is calculated as follows:

$$P_{prop} = R_{yield} \cdot R_{sh} \cdot P_y \quad (\text{Equation 4-1})$$

where R_y is ratio of actual yield strength to minimum specified yield taken as 1.0 here because coupon test data (see Appendix 1) has been used in calculation, and R_{sh} is the strain hardening coefficient taken as 1.2 based on experimental data in chapter 3. Designers could use R_{yield} and R_{sh} similar to ratio of probable to minimal yield strength, R_y and strain-hardening factor, C_{pr} , respectively calculated as per specified in AISC 341-16 (AISC, 2016).

The shear force of the beam transferred to the pin connector is calculated using the free body diagram of Figure 4-2b as follows:

$$V_{prop} = R_{prop} = M_{prop}/span \quad (\text{Equation 4-2})$$

where $M_{prop} = R_y \cdot R_e \cdot M_y$ is the probable yield moment of the fuse, and R_{prop} is the maximum vertical reaction induced in the beam.

4.2.4 Moment capacity

An analytical model capable of predicting the moment capacity of the connection was developed as shown in Figure 4-3. As shown, this model uses a half-circle connected to two straight elements at both ends. The radius of the half-circle is the same as the fuse centerline radius, R_{cl} , and the length of the straight element is equal to the fuse-free length before the first contact point, l_f . The analytical model addresses both orientations of U-shaped fuses, Open-Fuse and Closed-Fuse

connections as shown in Figure 4-3a and 3b, respectively. The Open-Fuse arrangement is the primary focus of this study due to its flexibility for replacement and suitability with the adjacent glulam beams. The Closed-Fuse connection was examined here as an alternate U-shaped plate arrangement. Referring to Figure 4-3, the rotation is permitted in Open-Fuse connections because the fuse's leg can rotate freely under the load acting in the perpendicular direction (Figure 4-3a), while the Closed-Fuse connections restrict the legs from rotating in its anticipated direction as it is represented in Figure 4-3b.

Open-Fuse Connection

Figure 4-4 presents the analytical model of the Open-Fuse connection. Fuses are modelled as translational springs at the final contact point between the fuse leg and the end plate, i.e., the edge of the connecting bolt at a distance \bar{Y} from the pin as shown in Figure 4-4a. This modeling approach for the springs' location considers the permanent deformation in the fuse leg, occurring at the transition between the end of the bent part and the start of the straight leg. This deformation, due to repetitive load cycles, leads to the contact point being considered at the bolt edge. When a transverse load, F , acts at the tip of the beam, it creates the rotation, θ , and scissor displacement, Δ , in each fuse (Figure 4-4b). Using the free body diagram of the connection shown in Figure 4-4a, the vertical reaction at the pin V , equals the applied force, F . In the horizontal direction, the tensile force, T , equals the compressive force, C , in the fuse, both represented by P in Figs. 4c-4e.

The flexural stiffness and moment capacity of the connection when it deforms as Figure 4-4c are determined using an equivalent model shown in Figure 4-4d. A more simplified model is then created taking advantage of symmetry at Point A as shown in Figure 4-4e.

To calculate the flexural stiffness of the End-Hinged Fuse, K_{HF} , the virtual work method is used, assuming that the deflection at Point B is half of the scissor displacement, Δ , due to symmetry:

$$K_{HF} = \frac{P}{\Delta} = 3 \frac{EI}{l'^3} \quad (\text{Equation 4-3})$$

Referring to Figure 4-4e, the force, P , produces a scissor displacement, Δ , along the horizontal direction and the vertical distance between Points A and B is set as the fuse effective span, l' .

Using the free body diagram of Figure 4-4e, the moment at Point A, M_A , is:

$$M_A = P \cdot l' \quad (\text{Equation 4-4})$$

The ultimate limit state of the plate, i.e., a complete plastic mechanism, is achieved when a flexural plastic hinge forms at Points A (Figure 4-4e) under the combined effect of axial force and bending.

The yielding capacity of the fuse, P_y , is therefore determined as:

$$P_y = wtF_y \left[\frac{1}{1 + \frac{4l'}{t}} \right] = wtF_y \xi_{HF} \quad (\text{Equation 4-5})$$

in which w is the width of the fuse out-of-plane, t is the plate thickness, and F_y is the yield strength of the steel material. ξ_{HF} is defined as an eccentricity factor for an End-Hinged fuse and is calculated as follows:

$$\xi_{HF} = \frac{1}{1 + \frac{4l'}{t}} \quad (\text{Equation 4-6})$$

Thus, the yielding moment capacity of the connection assembly, $M_{OF,y}$, is calculated using the free body diagram of Figure 4-4a and setting up the equilibrium forces and moments as follow:

$$M_{OF,y} = wtF_y \xi_{HF} \cdot (h_b - 2e) \quad (\text{Equation 4-7})$$

where h_b is the beam depth, and e is the distance between the fuse leg and the bolt edge as shown in Figure 4-4a.

Similarly, the connection stiffness, K_{OFC} , is calculated by referring to the relationship between the scissor displacement, Δ , and the connection rotation, θ , as follow:

$$\theta = \frac{\Delta}{\bar{Y}} \quad (\text{Equation 4-8})$$

Substituting this into the expression for stiffness:

$$K_{OFC} = \frac{M}{\theta} = \frac{3EI}{2l^3}(h_b - 2e) \quad (\text{Equation 4-9})$$

Closed-Fuse Connection

The proposed analytical model of the Closed-Fuse connection is shown in Figure 4-5. Fuses are modelled as translational springs at the final contact point between the fuse leg and end plate, assumed to be the bolt centerline (Figure 4-5a). This model considers the permanent deformation in the fuse leg at the transition between the bent and straight parts. Due to repeated load cycles, this leads to a prying action affecting the bolt. Therefore, the contact point is placed at the bolt centerline. Translational spring properties are determined using the fuse model in Figure 4-5b. As described for the Open-Fuse connection, a vertical load, F , acting at the tip of the beam creates the rotation, θ , and scissor displacement, Δ , as shown in Figure 4-5b. The free body diagram of Figure 4-5a reveals that the vertical reaction in the pin, V , equals the applied force, F , and the tensile force, T , equals the compressive force, C , which are represented by P .

Following similar steps described for the OF connection, the flexural stiffness and the yielding force of the fuse in a CF connection is calculated as follow:

$$K_{FF} = 1.2 \frac{EI}{l'^3} \quad (\text{Equation 4-10})$$

$$F_{cy} = wtF_y \left[\frac{2}{1 + \frac{4l'}{t}} \right] = wt f_y \xi_{FF} \quad (\text{Equation 4-11})$$

where ξ_{FF} is the eccentricity factor for the End-fixed fuse calculated as follows:

$$\xi_{FF} = \frac{2}{1 + \frac{4l'}{t}} \quad (\text{Equation 4-12})$$

Following a similar approach as the OF connection, the yielding moment capacity, $M_{CF,y}$, and the flexural stiffness, K_{CFC} , of the CF connection is obtained as:

$$M_{CF,y} = wtF_y \xi_{FF} \cdot (h_b - 2e) \quad (\text{Equation 4-13})$$

$$K_{CFC} = \frac{2F \cdot \bar{Y}}{\Delta / \bar{Y}} = 2K_{FF} \bar{Y}^2 = \frac{3EI}{5l'^3} (h_b - 2e)^2 \quad (\text{Equation 4-14})$$

4.2.5 Potential Applications in Seismic Design

Two potential applications of the proposed hybrid connection are shown in Figure 4-6. Figure 4-6a shown the application in a hybrid steel-timber moment-resisting frame, where the U-shaped fuses implemented in the beam-to-column joints are expected to dissipate seismic energy. Another potential application of the proposed connection is shown in Figure 4-6b in a rocking steel braced frame linked to a timber gravity system equipped with a self-centering capability using post-tensioned (PT) strands (Filiatrault et al., 2004).

4.3 Experimental Program

The full-scale experimental program was conducted at C-FER Technologies in Edmonton, Canada using the quasi-static testing procedure. The test program included four glulam beams (GB1, GB2,

GB3, and GB4) equipped with the proposed U-shaped connection with varying plate thickness. They were initially tested once in OF configuration with single or double self-tapping screw reinforcement. After that, the beams were retested to represent the retrofitted connection, in both OF and CF configurations, with double self-tapping screw reinforcement.

4.3.1 Test Matrix

Table 4-1 presents the matrix of the specimens tested in this test program. The specimens include those with the original glulam beam (GB) and the initial set of fuses and those where glulam beam is retrofitted (RGB) after replacing their yielded fuses with new ones. Groups I and II of GB specimens employed OF orientation, with the only difference being that Group I used single Self-Tabing Screws (STS) reinforcement, while Group II benefited from double STS reinforcement to investigate the effect of STS reinforcement. Groups III and IV of the RGB specimens utilized double STS reinforcement with the only difference being that Group III used OF orientation as replicas, while Group IV used CF orientation. The specimen labels include the fuse thickness, followed by the fuse orientation and the STS reinforcement.

4.3.2 Specimens

The glulam beams, GB1, GB2, GB3 and GB4, are shown in Figure 4-7a – 7e. Each beam was tested twice, once using original configuration with specific fuse or STS reinforcement and then with a new pair of fuses of the same thickness. Eight pairs of U-shaped fuses with four different thicknesses ranging from 13 to 22 mm were selected (Figure 4-8). GB1 - GB4 were designed using a U-shaped plate with a thicknesses of 13, 16, 19 and 22 mm, respectively. The glulam beams have the same dimensions of 265mm × 608mm × 1150mm, with the only difference being the number of SDDs used in the upper and lower parts of each specimen. These dowels protect the specimens

from compressive and tensile forces generated by the scissor bending of the fuses. Each fuse thickness is associated with a unique number of SDDs to carry the anticipated connection shear force.

U-shaped steel plates, knife plates, weld, SDDs, and bolts, were designed in accordance with the Canadian steel design standard, CSA S16 (Canadian Standards Association, 2014b), whereas the timber components, including the glulam beam and its connections were sized as per the Canadian Standard for Engineering Design in Wood, CSA O86 (Canadian Standards Association, 2014a). The glulam beams are made from Douglas-Fir Gr. 24f-EX and selected to resist the probable yield Moment, $M_{prop} = 205$ kN.m. U-shaped plates, made of steel conforming to CSA G40.21 300W (CSA Association, 2013) with a specified yield strength of 300 MPa. A custom bender was employed to shape these U-shaped plates. The end T-plate, to which four pre-tensioned 19-mm ASTM A490 high-strength steel bolts connected the U-shaped plates (ASTM International, 2020) was welded to double knife plates embedded in wood. 6 mm-thick butt welds were used between the knife plates and the end T-plate.

To connect the glulam beam to the knife plates, $\Phi 7.5 \times 235$ self-drilling dowels (SDDs) of SBD provided by RothoBlass (RothoBlass, 2022b) were selected. The knife plates, adhering to both CSA S16 and SDD manufacturer guidelines, utilized 6mm-thick S275 steel (RothoBlass, 2022a) to prevent potential drilling complications. The recommended pressure of approximately 40 kg and a screwing speed of around 1000 - 1500 rpm for a steel plate were adhered to ensure optimal performance and structural integrity. The self-tapping screws (STS) used for reinforcement to avoid splitting are VGZ-fully-threaded screws with cylinder head $\Phi 9 \times 280$ (Rothoblaas, 2022).

4.3.3 Test Setup

The test setup shown in Figure 4-9 consists of the reaction wall with a horizontally placed hydraulic actuator. The hydraulic actuator has a maximum load capacity of 300 kN and a stroke range of +/- 160 mm in both directions. The column member was represented by a reaction steel beam fixed to the strong floor using steel anchor rods attached to Hollow Structural Sections at both ends of the steel beam. To secure the reaction beam against horizontal loads, steel blocks with loading steel columns were used. The horizontal actuator was attached to the top end of beam with a steel cage comprising two steel plates attached using six steel rods.

To measure global and local responses of the specimens, load cells, potentiometers, inclinometers, Linear Variable Differential Transformers (LVDTs), strain gauges, and digital image correlation system, were used. The instrumentation plan is shown in Figure 4-9d and 9e. The applied load was measured using a load cell. Potentiometer P1 was used to measure actuator displacement, while P2 and P3 were fixed on both sides of the beam to control the applied displacement using the average of two readings. P4 monitored out-of-plane displacement at the top of the beam, and P5 measured the horizontal sliding of the setup. inclinometers I1-I4 were installed to capture the rotation of the glulam beam, the west knife plate, the east knife plate, and the pin connector, respectively, while I5 was used to monitor the actuator rotation during the test. LVDTs 1-4 were used to measure the relative scissor displacements between the legs of the fuses. Four strain gauges (SG) were attached to the inner and outer faces of the fuses at the most critical regions. Non-contact strain field measurements using the DIC system was also employed to monitor the deformation of the glulam beam (correlatedsolutions, 2018).

4.3.4 Loading Scheme

Figure 4-10 illustrates the cyclic loading protocols developed to perform the tests. Figure 4-10a shows the cyclic loading protocol developed based on FEMA 461 (FEMA; & ATC, 2007), which includes 26 displacement cycles. Each amplitude repeats twice, creating a pattern of increasing displacement with a maximum displacement of 54 mm at 900 mm away from the pin connector centreline. This creates a 6% chord rotation equivalent to a storey drift angle of 3% when the fuses are used as part of beam-to-column connections of a 3-storey building located in Vancouver. The prototype building used for this study shares similarities with the one described in Mowafy et al. 2021 (Mowafy et al., 2021), although the current research employs U-shaped fuses and a self-centering (SC) system for additional resilience. A total of 10 additional cycles with the same pace were then applied until failure or a maximum chord rotation of 16% was reached. This rotation is equivalent to 8% storey drift and five times the yielding displacement of the fuses. The cyclic loading protocol was used to perform seven tests, while one of the specimens (R22OF-DR) was evaluated under the seismic loading protocol of Figure 4-10b obtained from a nonlinear response history analysis of a 3-storey building located in Vancouver, using a displacement from the Miyagi, Japan 2011 ground motion. Similar to the cyclic loading protocol, two displacement cycles with an amplitude of 12% and 16% were applied once the ground motion-generated deformation ended as shown in Figure 4-10b.

4.4 Experimental results

This section presents the results of the eight cyclic tests conducted to evaluate the seismic performance of the proposed hybrid connection. The test results include connection moment-rotation hysteretic responses, observed failure modes, stiffness degradation, and ductility and energy dissipation capacities. Referring to Figure 4-11, the moment resisted by the connection

about the pin caused by the force F can be calculated by setting the equilibrium equation for the moment around the pin connector point as follows:

$$M = F. [S. \cos(\theta_j) + e. \sin(\theta_j) + L. \sin(\theta_j). \cos(\theta_j)] \quad (\text{Equation 4-15})$$

where θ_j is the jack rotation.

4.4.1 Hysteresis response

Figure 4-12 shows the normalized moment-chord rotation response of specimens. The vertical axis represents flexural moment normalized to the respective yielding capacity, which is determined from a bilinear backbone curve of the connection developed by connecting peak points of the hysteresis loops in each loading cycle. All specimens achieved $\pm 6\%$ rad. chord rotation without any noticeable global failure, but limited pinching behaviour. 10 additional cycles (Figure 4-10) with increasing amplitudes were applied until failure or a maximum $\pm 16\%$ rad. chord rotation was attained. Referring to Figure 4-12a – 12f, OF specimens in Groups I, II, and III exhibited a stable response with significant strain hardening and overstrength capacity, reaching on average 1.2 times the yielding capacity of the connection. Furthermore, a large deformation ductility (in the order of 5) was observed, which stems from the robust nonlinear response of the U-shaped fuses implemented in the connections. A closer examination of pinching behaviour observed in the OF connections shows that this response is associated with the plastic deformations developed in the U-shaped fuses, leading to residual deformations. Despite this phenomenon, it is not expected to significantly impact the energy dissipation capacity of the connection, as the inherent ductility of the fuses allows for continued load resistance even with the presence of these deformations.

The hysteresis behaviour of CF specimens in Group IV shown in Figure 4-13g and 13h involves a more noticeable progressive stiffness degradation or pinching response. Crack initiation was observed for the first time in the glulam beam at 4% chord rotation, leading to minor strength degradation in the second cycle of 4% rotation. Although flexural strength slightly decreased in the 6% rotation cycles, it remained above the 80% peak resistance, meeting the connection qualification requirement in AISC Seismic Provisions for Structural Steel Buildings, AISC 34-16 (AISC, 2016) for steel moment connections. Beyond 10% chord rotation, flexural capacity increased despite the slight reduction in preceding cycles due to plastic deformations occurring in the bent part of the U-shaped fuse. As the deformations progressed, they caused the fuse to come into contact with the column surface, creating a new boundary condition within the fuse itself. Specimen R19CF-DR failed at the pin connector SDDs, mainly due to global splitting failure at 14.5% chord rotation. No global failure was observed in Specimen R13CF-DR until the end of the test, which corresponds to 15% chord rotation. The hysteresis response of R22OF-DR under earthquake-consistent loading protocol demonstrates its potential to develop plastic hinging in U-shaped plates as expected in design.

All connection specimens exhibited a symmetric response, even though the fuse testing results displayed an asymmetric response. This stems from the fact that fuses are subjected to both tension and compression simultaneously, whereas in the fuse testing, both fuses experience either compression or tension simultaneously

4.4.2 Failure Modes

The key failure modes of Group I specimens with single STS reinforcement, S13OF-SR and S16OF-SR, included ductile yielding of steel fuses without any crack initiation in the glulam beam

in S13OF-SR, while S16OF-SR experienced crack initiation near the U-shaped fuse at 12% rotation. Figure 4-13 shows the 35th cycle of the normalized moment-rotation response where splitting was observed in the glulam beam in both loading directions. The DIC system data as shown in Figure 4-13b and 13c confirmed plastic hinging in the U-shaped plates, e.g., 0.2% Von Mises (VM) strain represents the yielding strain from the coupon test.

For Group II and Group III specimens, fuse yielding was the only failure mode observed. There were no splitting cracks in the glulam beams (Figure 4-14b). The VM strain distribution at maximum rotation demand (15%) remained consistent among OF specimens. Figure 4-14c shows yielding regions in the fuse at the 35th loading cycle of Figure 4-14a.

Implementing double STS reinforcement in Group II and Group III effectively prevents splitting cracks in glulam beams due to the confinement provided by the reinforcement, which evenly distributes the forces induced by fuses among the rows. Figure 4-15 highlights the difference in the principal strain field between single and double reinforcement. In single reinforcement case, higher values are concentrated in the two rows closest to the fuse half circle (Figure 4-15a), a phenomenon that corresponds to the splitting in Specimen 16OF-SR (Figure 4-13). Conversely, double reinforcement provided a more uniform strain distribution among all rows (Figure 4-15b), which suggests that this arrangement can potentially be used in design to effectively resist fuse-induced forces.

The testing of two specimens in Group IV with CF revealed a progressive stiffness degradation, with R19CF-DR exhibiting more severe pinching behaviour than R13CF-DR. Figure 4-16 illustrates the failure modes observed for R19CF-DR. At a chord rotation of 4%, a crack initiated near the pin (Figure 4-16a), and it propagated predominantly towards the edge row of the middle

SDDs adjacent to the pin connector. At 6% chord rotation, an alternative crack developed near the alternate compressive fuse (Figure 4-16b). As the lateral displacement increased, a sudden increase in flexural resistance was captured, mainly due to excessive deformation and changes in boundary conditions as the fuse rests on the base support beam (Figure 4-16c). For R19CF-DR, a set of cracks developed at the middle SDDs adjacent to the pin connector (Figure 4-17a), leading to a global failure of the glulam beam in the last two cycles of loading. This failure happened as splitting cracks generated in the beam (Figure 4-17b). R13CF-DR exhibited similar behaviour except that the increase in the flexural capacity occurred at 16% chord rotation and no global splitting failure was observed.

The failure modes of the specimens are summarized in Table 4-2. Group I specimens showed ductile yielding in steel fuses, with one specimen exhibiting splitting cracks in the glulam beam. Group II and III specimens reinforced with double STS showed only fuse yielding with no splitting cracks. Group IV specimens with closed U-shaped fuses experienced progressive stiffness degradation, crack initiation and propagation, an increase in the flexural capacity, and in some cases, a global failure in the glulam beam. Overall, OF specimens with double STS reinforcement showed a more robust cyclic response with ductile failure modes.

4.4.3 Connection performance characteristics

The backbone curves of the specimens, which were obtained by connecting the peaks of the hysteresis response of each specimen, are shown in Figure 4-18, except Specimen R22OF-DR as it was loaded under a seismic loading protocol. Overall, OF specimens exhibited a similar response with yielding at 4%, followed by material strain hardening. The CF specimens showed a comparable overall response with slightly higher stiffness and yielding at around 2% before strain

hardening at 8%. The final fluctuation in the backbone curve of CF specimens is associated to the increase in the yielding capacity of the connection.

The main performance characteristics of the connections studied are listed in Table 4-3. The nominal yield moment and yield rotation were determined using a bilinear backbone. The rotational ductility $\mu = \theta_u/\theta_y$ was obtained as per EN12512 (CEN, 2001) where θ_u is the chord rotation either at the maximum moment or at the end of the test (if no strength degradation is observed), and θ_y is the rotation at yield moment determined by the equivalent energy method. Referring to Table 4-3, CF connections exhibited higher flexural stiffness (on average 402% higher) and flexural strength (133.5kN.m vs. 52 kN.m on average) compared to OF connections. The ultimate moment for CF connections range between 87 and 180 kN.m, whereas that for OF connections vary between 32 and 92 kN.m. OF connections with a rotational ductility of $\mu = 4 - 6$ are categorized as moderate ductility. In contrast, closed-fuse connections with a ductility factor of $\mu > 6$ are considered as high ductile connections as per the criteria by Smith et al. (Smith et al., 2006) for timber connections.

4.4.4 Energy dissipation capacity

The hysteretic energy, which is determined as the area inside the moment-chord rotation curve, is an indicator of the capacity of a connection to dissipate seismic-induced energy. Figure 4-19a plots cumulative energy against cumulative rotation for all eight connections. As shown, the energy dissipation capacity of OF connections increases by 30-50% by every 3 mm increase in fuse thickness. However, CF connections exhibit a 130% increase in energy dissipation compared to their OF counterparts for the same fuse thickness, indicating a superior energy dissipation capacity compared to OF connections.

Figure 4-19b illustrates the energy absorbed by the specimens during each loading cycle. The initial elastic cycles (cycles 1-22 for OF and cycles 1-20 for CF specimens) have minimal energy dissipation as expected with amplitudes less than 4% for OF specimens and 2% for CF specimens. However, in-cycle energy dissipation capacity increases exponentially once the yielding limit is exceeded (cycles 23-36 for OF specimens and cycles 21-36 for CF specimens). When splitting cracks developed in the glulam beams, a repeated cycle with the same amplitude as the previous one exhibits relatively lower energy dissipation than the predominant cycle. This reduction is due to crack propagation caused by the predominant cycle as observed for Specimens 16OF-SR, R13CF-DR, and R19CF-DR. All in all, this comparison reaffirms that CF connections demonstrate greater energy absorption capacity than OF connections despite the brittle failure mode observed in CF connections. This observation is attributed to that fact that the CF connections have relatively higher stiffness and higher moment strength.

4.4.5 Evaluation of moment capacity prediction

The yield moment predicted using Eq. 4-7 are compared with the experimental moments shown in Figure 4-18 for both OF and CF connections. This comparison is shown in Figure 4-20. As shown, the analytical model predicts the yield moment on average 10% higher than the measured for OF connections with thinner fuses (specific thickness, e.g., 13mm, 16 mm), such as in specimens 13OF-SR, 16OF-SR, and R16OF-DR. Conversely, the proposed equation tends to underestimate the moment capacity by about 5% for the specimens with thicker fuses (specific thickness, e.g., 19mm, 22 mm), such as in specimens 19OF-DR and 22OF-DR. In the case of CF connections, the model consistently overestimates the yield moments with an average overestimation of about 5%.

4.5 Conclusions

This paper presents a new hybrid steel-timber beam-to-column connection with replaceable U-shaped fuses for seismic applications in multi-storey buildings. Two U-shaped plate arrangements, open-fuse and close-fuse were investigated. Simplified analytical methods to predict flexural moment and stiffness of the connection were proposed for engineering applications. Eight quasi-static cyclic tests were conducted to evaluate the cyclic performance of the proposed connections using four glulam beams by varying the U-shaped fuse thickness as 13, 16, 19, and 22 mm. The beams were reused to perform the second half of the tests with additional self-tapping screws reinforcement, referred to as retrofitted specimens. Of eight connection specimens, six specimens were tested in open-fuse arrangement and the remaining two specimens were set-up with close-fuses. The main findings of this study are summarized below:

- All double-reinforced open-fuse connections with two STS, including virgin glulam beams (Group II) and retrofitted ones (Group III), exhibited excellent ductile behaviour, with no cracks or strength degradation.
- Open-fuse connections with single STS reinforcement (Group I) exhibited splitting cracks in glulam beam at a chord rotation of 12% without noticeable strength degradation.
- Closed-fuse connections showed relatively higher stiffness and higher ductility. Splitting cracks took place around the pin connector area in the glulam beam at 4% chord rotation, which translates to 2% to 4% story drift in practical applications, suggesting that the Closed-fuse arrangement is viable solution for the connections studied here.
- Open-fuse connections showed similar hysteresis behaviour as closed-fuse connections with yielding at 4% chord rotation, while Closed-Fuse connections yielded earlier at 2% chord rotation.

- The results obtained from the retrofitted beams in which U-shaped plates were replaced with a new set showed the same cyclic performance, hysteretic behaviour, stiffness, and energy dissipation, as the original connections, confirming the potential for replacing steel U-shaped elements after a moderate or major seismic event.
- Increased U-shaped fuse thickness (13 to 22 mm) raises the connection stiffness and yield moment, 26 – 78 kN.m for open-fuse connections and 73 – 152 kN.m for closed-fuse connections.
- The proposed analytical model for moment capacity of the connection predicts the flexural moment capacity of the connection with sufficient accuracy, an error of +/-10%. Such method can be used in design to estimate the connection resistance and achieve a preliminary U-shaped plate thickness.

The study's scope was limited to specific beam sizes; future work could investigate the proposed connections with various beam sizes suitable for multi-storey buildings to enhance general applicability. The research focused on component-level behavior; an extension to system-level testing could further reveal how the connections perform within a full structural system, adding valuable insights for structural design. The limited exploration of specific U-shaped fuses leaves room for future investigations into alternative materials or shapes (i.e. perforated plates), potentially uncovering connections with improved performance characteristics.

Notation

The following symbols are used in this chapter:

SDD: Self-Drilling Dowel

T: Tension

C: Compression

LVDT: Linear Variable Differential Transformer

P: Potentiometers

I: inclinometers

SG: Strain Gauges

DIC: Digital Image Correlation

NBC: National Building Code

STS: Self-Tapping Screw

GB: Glulam beam

RGB: Retrofitted Glulam Beam

OF: Open-Fuse

STS: Single Self-Tapping Screw

SR: Single Self-Tapping Screw Reinforcement

PT: Post-Tensioned strands

DR: Double Self-Tapping Screw Reinforcement

CF: Closed-Fuse

VM: Von Mises

R_y = factor employed to estimate the impact of strain hardening

R_e = eccentricity factor introduced to account for potential deviations

P_y = fuse's yielding capacity

P_{prop} = probable yielding fuse capacity

V_u = probable maximum vertical shear force

M_{prop} = probable yield moment of the fuse

R_{prop} = maximum vertical reaction induced in the beam

P = force causing scissor displacement

Δ = scissor displacement

l' = U-shaped fuse's effective span

M_A = reaction moment at point A

K_{HF} = flexural stiffness of the End-Hinged Fuse

P_y = yielding capacity of the fuse

w = width of the fuse out-of-plane

t = plate thickness

F_y = yield strength of the steel material

ξ_{HF} = eccentricity factor for an End-Hinged fuse

$M_{OF,y}$ = yielding moment capacity of the connection

h_b = beam height

e = distance from the fuse leg to the bolt edge

K_{FF} = fuse stiffness

F_{cy} = fuse yielding force

ξ_{FF} = eccentricity factor for fixed fuse

$M_{CF,y}$ = yielding moment capacity of the Closed-Fuse Connection

K_{CFC} = Closed-Fuse connection stiffness

F = applied load from actuator

S = span of the glulam beam at its centreline

L = Length of the actuator

M = moment resisted by the connection

θ_j = jack rotation

μ = ductility factor

θ_u = connection rotation either at the maximum moment or at the end of the test

θ_y = rotation at yielding

Table 4-1. Test Matrix

A. Original Glulam Beams (GB)				
Test Group	I. GB with SR		II. GB with DR	
Specimen	13OF-SR	16OF-SR	22OF-DR	22OF-DR
				
Fuse Thickness [mm]	13	16	19	22
Glulam Beam	GB1	GB2	GB3	GB4
SDD No.	65	81	105	125
Fuse Orientation	Open Fuse	Open Fuse	Open Fuse	Open Fuse
STS Reinf.	Single Reinf.	Single Reinf.	Double Reinf.	Double Reinf.
B. Retrofitted Glulam Beams (RGB)				
Test Group	IV. RGB with CF	III. RGB with OF	IV. RGB with CF	III. RGB with OF
Specimen	R13CF-DR	R16OF-DR	R19CF-DR	R22OF-DR*
				
Fuse Thickness [mm]	13	16	19	22
Glulam Beam	RGB1	RGB2	RGB3	RGB4
SDD No.	65	81	105	125
Fuse Orientation	Closed Fuse	Open Fuse	Closed Fuse	Open Fuse
STS Reinf.	Double Reinf.	Double Reinf.	Double Reinf.	Double Reinf.

* Specimen that used a loading protocol was obtained from the EQ record, while the others used FEMA 461 cyclic loading protocol.

Table 4-2. Summary of failure modes of specimens.

Group	Mode of failure for fuses	Mode of failure in the glulam beam
I – OF-SR	Yielding	Splitting initiation in the fuses SDD inner row*
II – OF-DR	Yielding	N/A
III – ROF-DR	Yielding	N/A
IV – RCF-SR	Two levels of yielding resistance with crack initiation in fuses	Splitting near the middle SDDs adjacent to the pin connector followed by global splitting failure+

*Observed in Specimen 16OF-SR only

+Observed in Specimen R19CF-DR only

Table 4-3. Summary of connection performance characteristics

Specimen	Moment-rotation stiffness, K [kN.m/rad]	Yield moment, M_y [kN.m]	Ultimate moment, M_u [kN.m]	M_u/M_y [%]	θ_y [rad.]	θ_u [rad.]	Ductility Factor, μ
13OF-SR	767	26	32	123%	3.44%	15.20%	↗ 4.42
16OF-SR	1199	40	48	120%	3.34%	15.15%	↗ 4.54
19OF-DR	1717	61	72	118%	3.57%	15.30%	↗ 4.29
22OF-DR	2326	78	92	118%	3.34%	15.40%	↗ 4.61
R16OF-DR	1022	37	49	132%	3.58%	15.20%	↗ 4.25
R13CF-DR	4440	73	87	119%	1.64%	15.20%	↑ 9.21
R19CF-DR	8038	152	180	118%	1.89%	15.30%	↑ 8.10

↗ moderate ductile fuses

↑ high ductile fuses

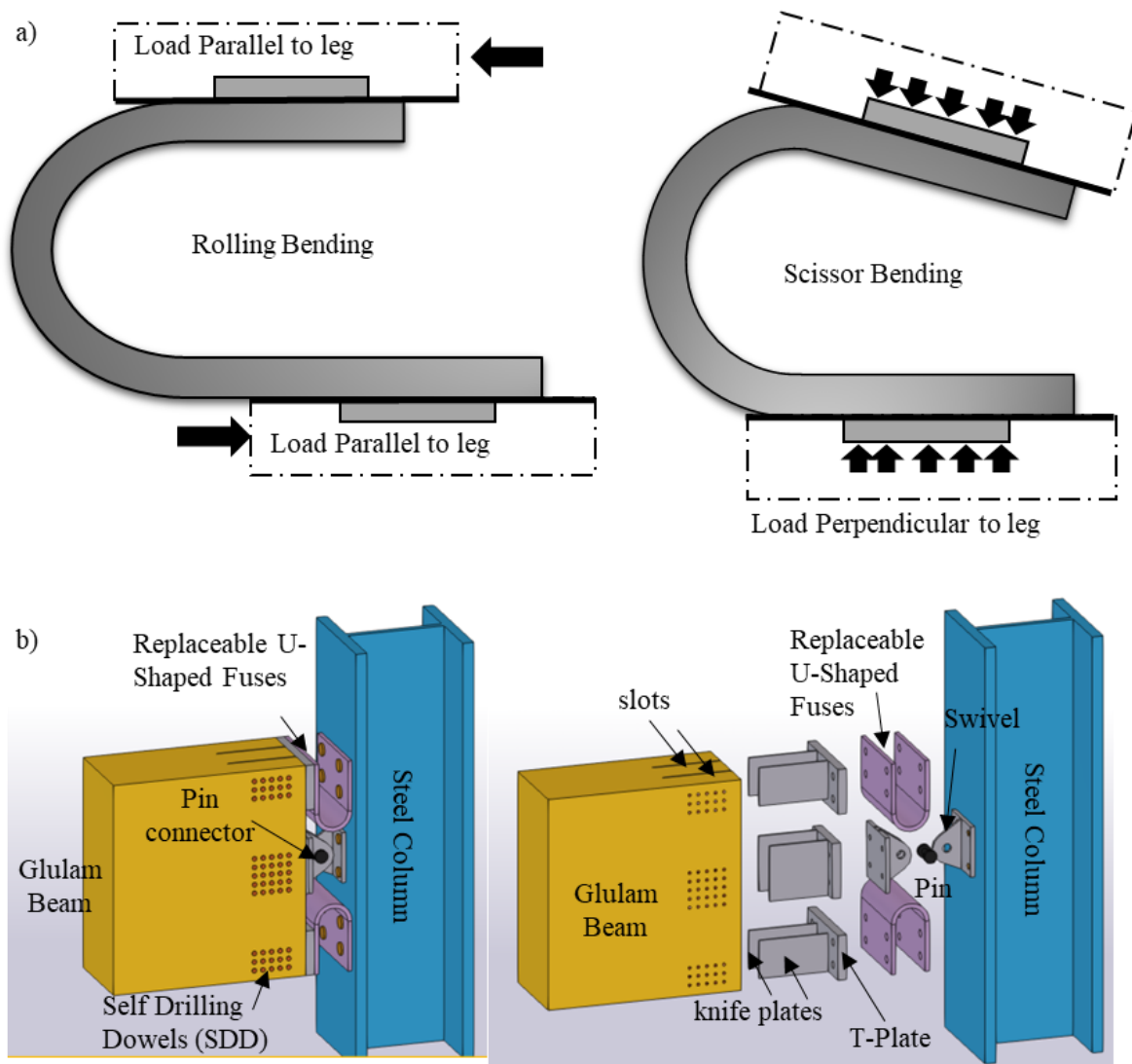


Figure 4-1. a) U-shaped steel fuse mechanisms (Mowafy et al., 2023); b) Connection components

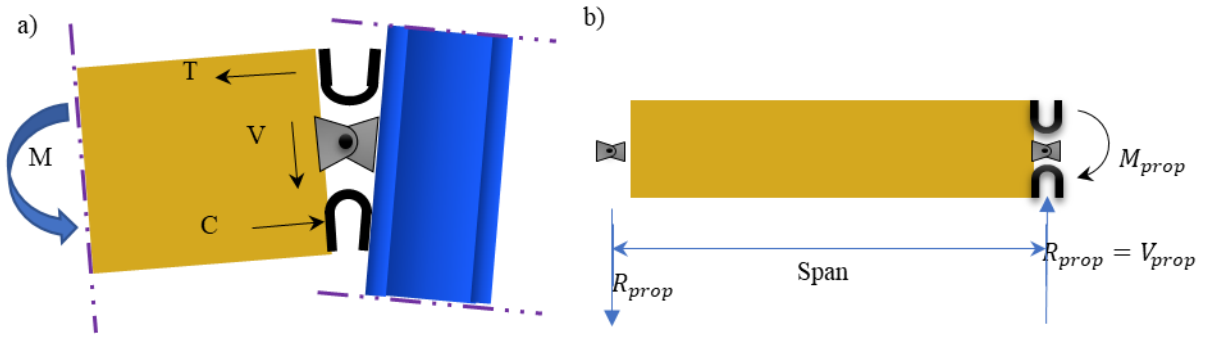


Figure 4-2. a) Flexural deformation under seismic loading; b) Free body diagram of the glulam beam under seismic loading.

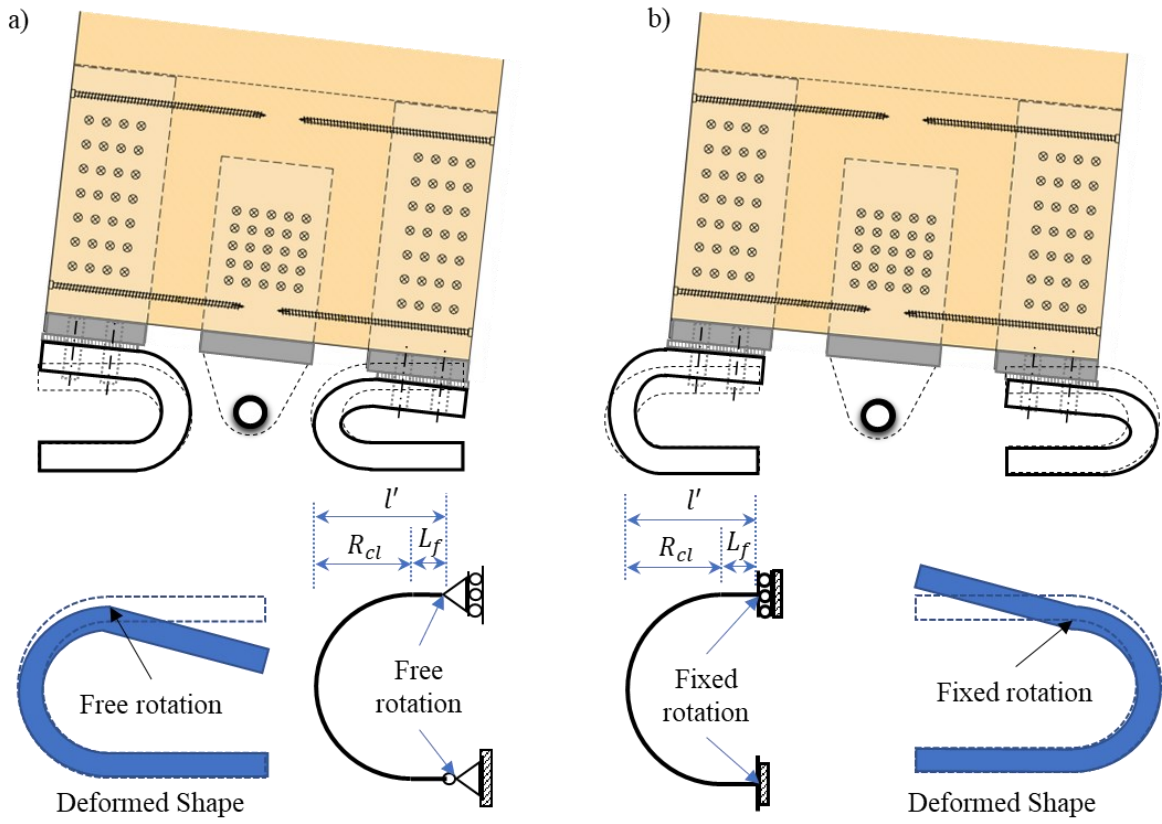


Figure 4-3. Fuse structural modelling: a) Open-Fuse connection; b) Closed-Fuse connection.

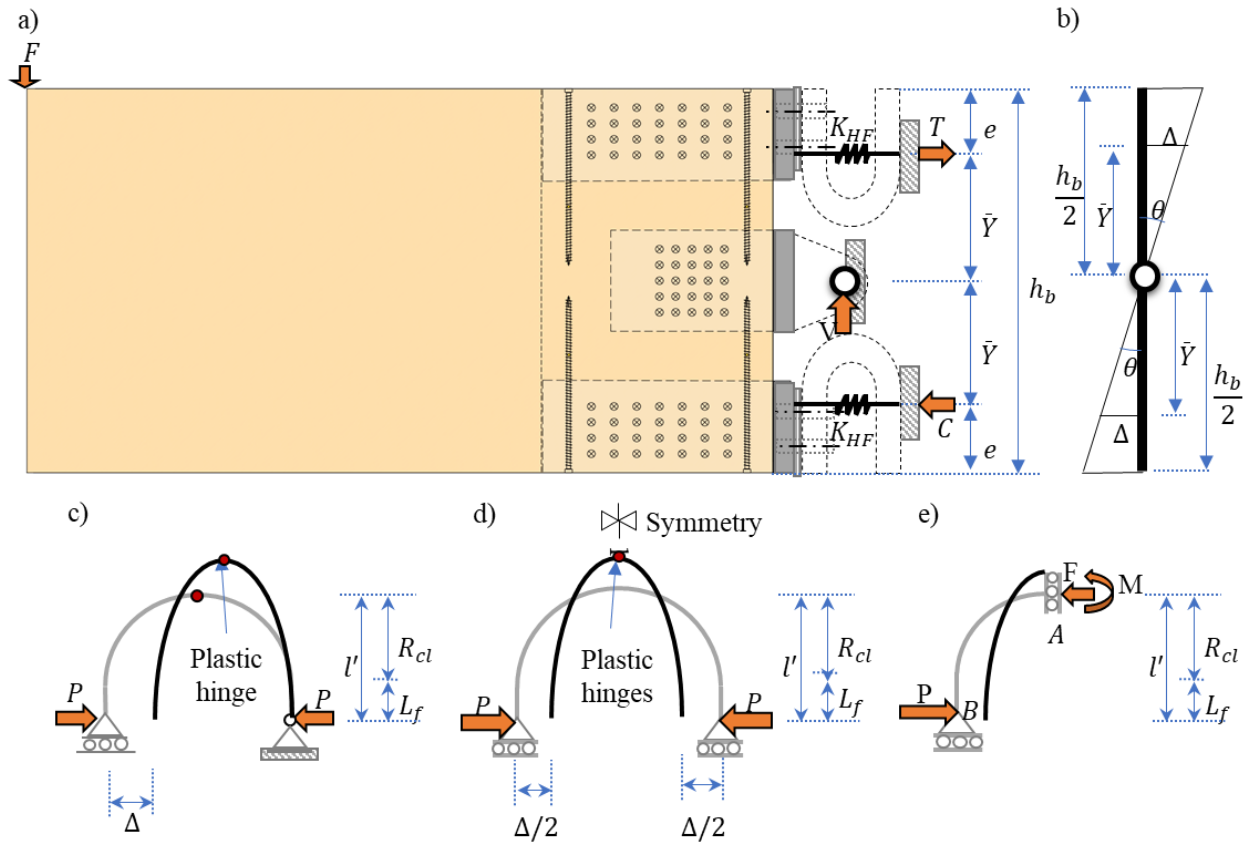


Figure 4-4. Analytical model of Open-Fuse Connection: a) Connection FBD; b) Deformation under flexural bending; c-e) Fuse analytical models: ideal, equivalent, and simplified.

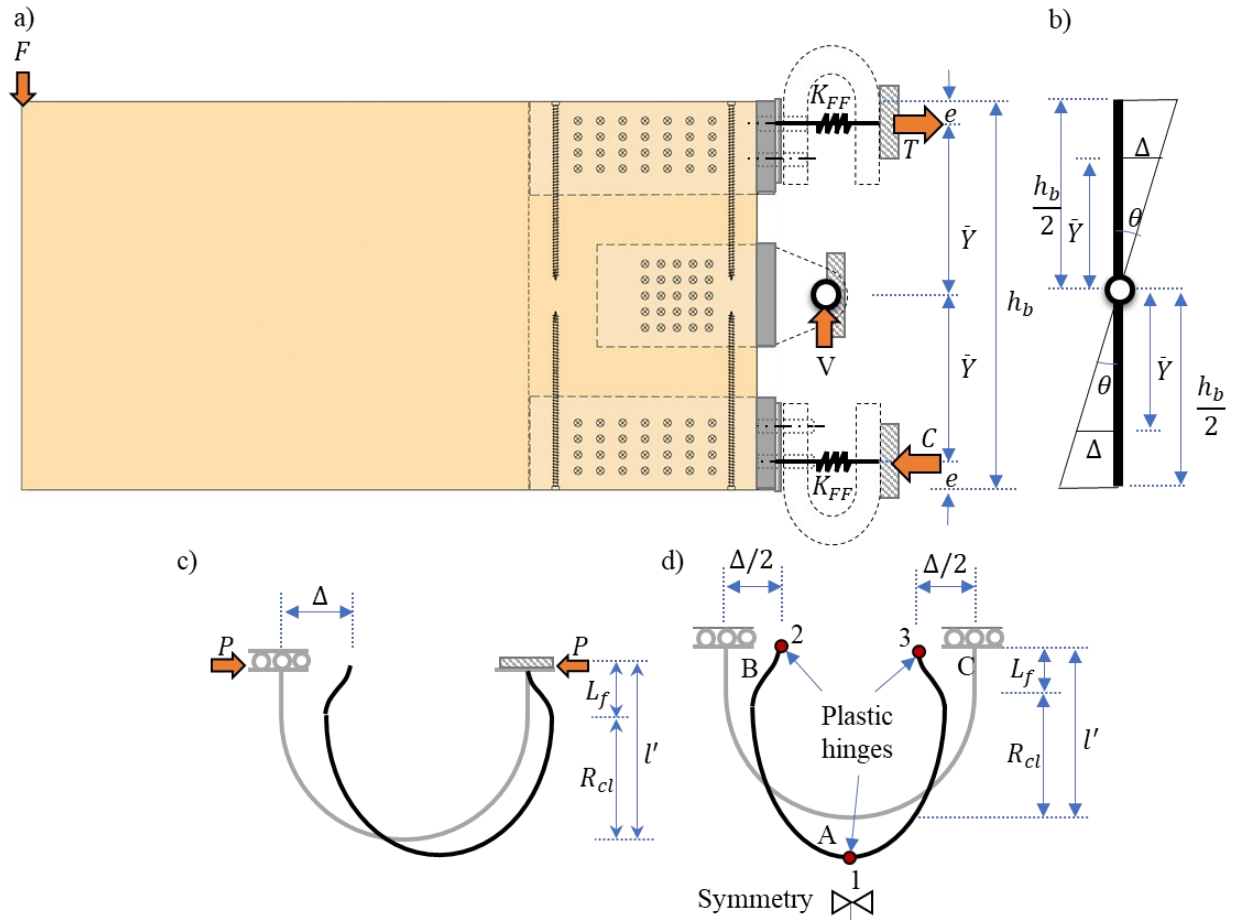


Figure 4-5. Analytical model of Closed-Fuse Connection: a) Connection FBD; b) Deformation under flexural bending; c-e) Fuse analytical models: idea and equivalent.

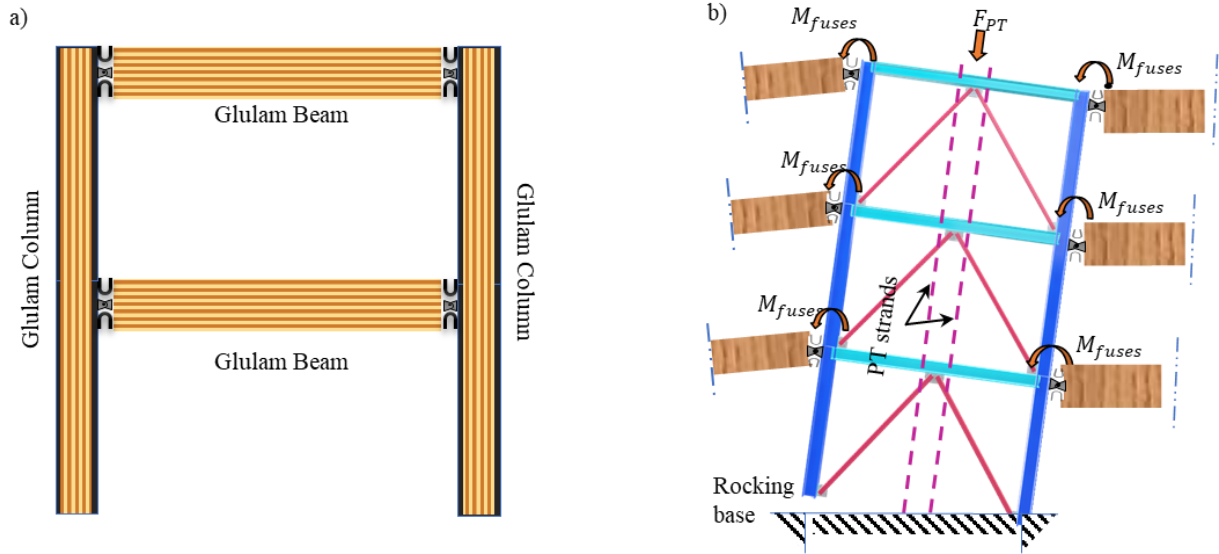


Figure 4-6. Potential applications: a) Timber Moment Resisting Frame; b) Control Rocking Concentrically Braced frames (CR-CBF).

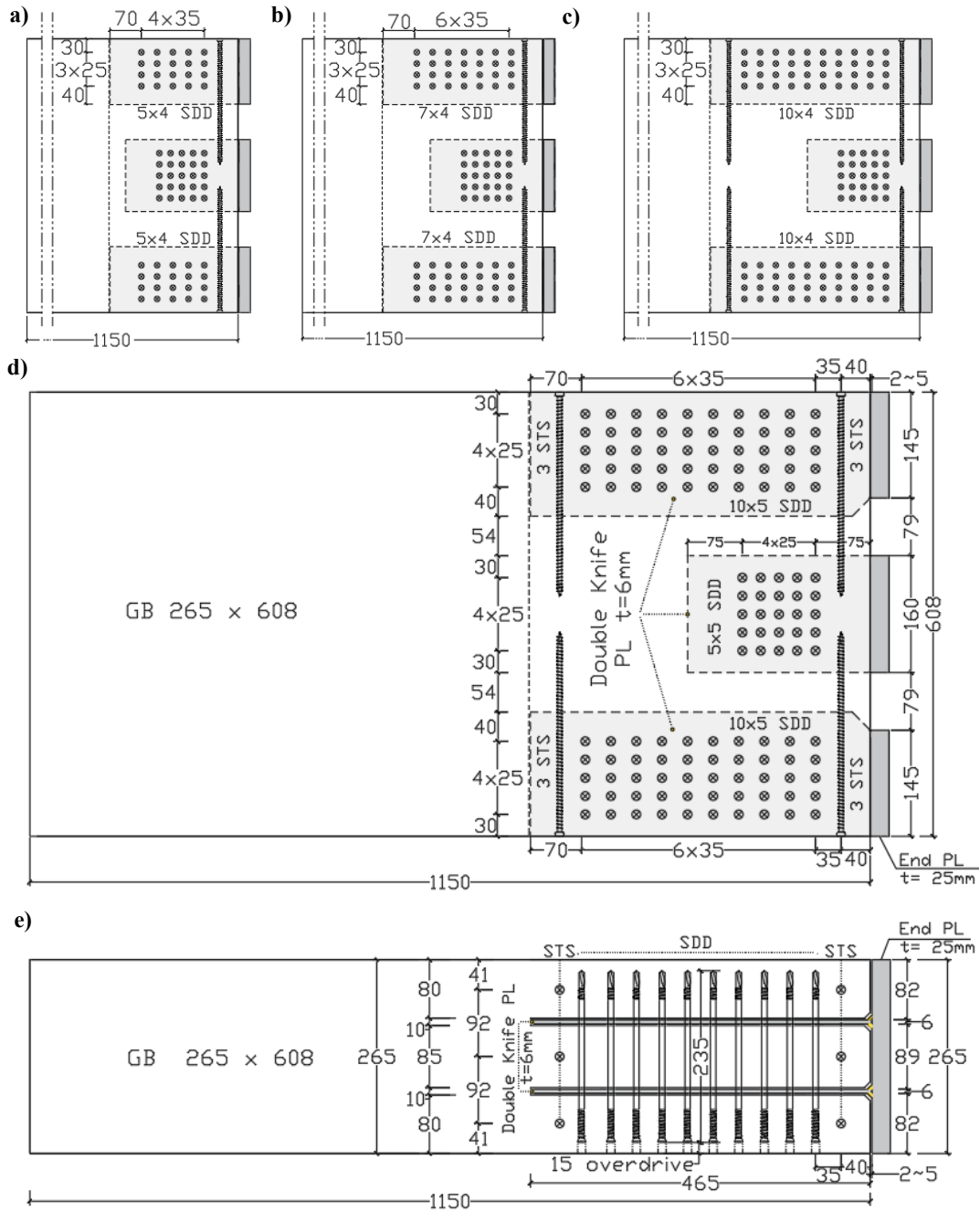


Figure 4-7. Specimens: a-c) GB1-3; d-e) GB4.

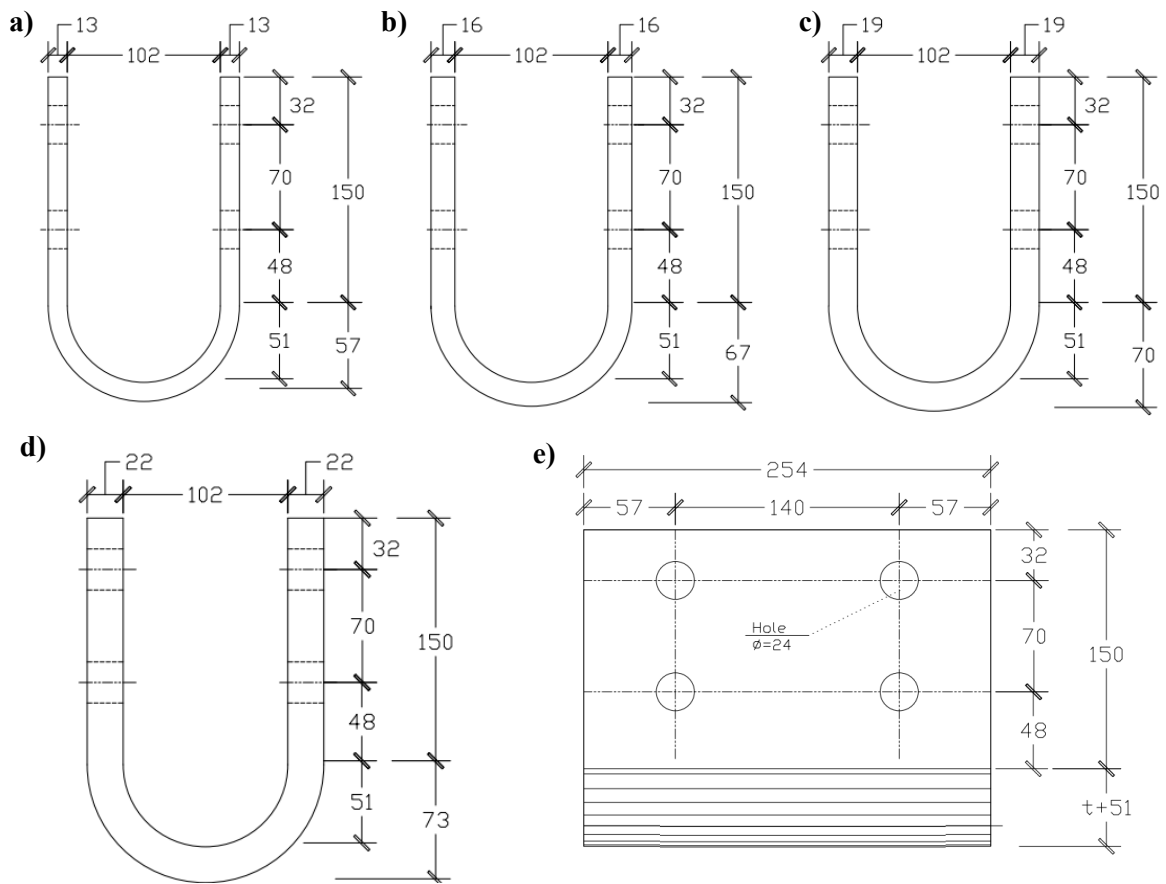


Figure 4-8. U-shaped fuses: a) 13 mm-thick fuse; b) 16 mm-thick fuse; c) 19 mm-thick fuse; d) 22 mm-thick fuse; e) Side view of the fuse.

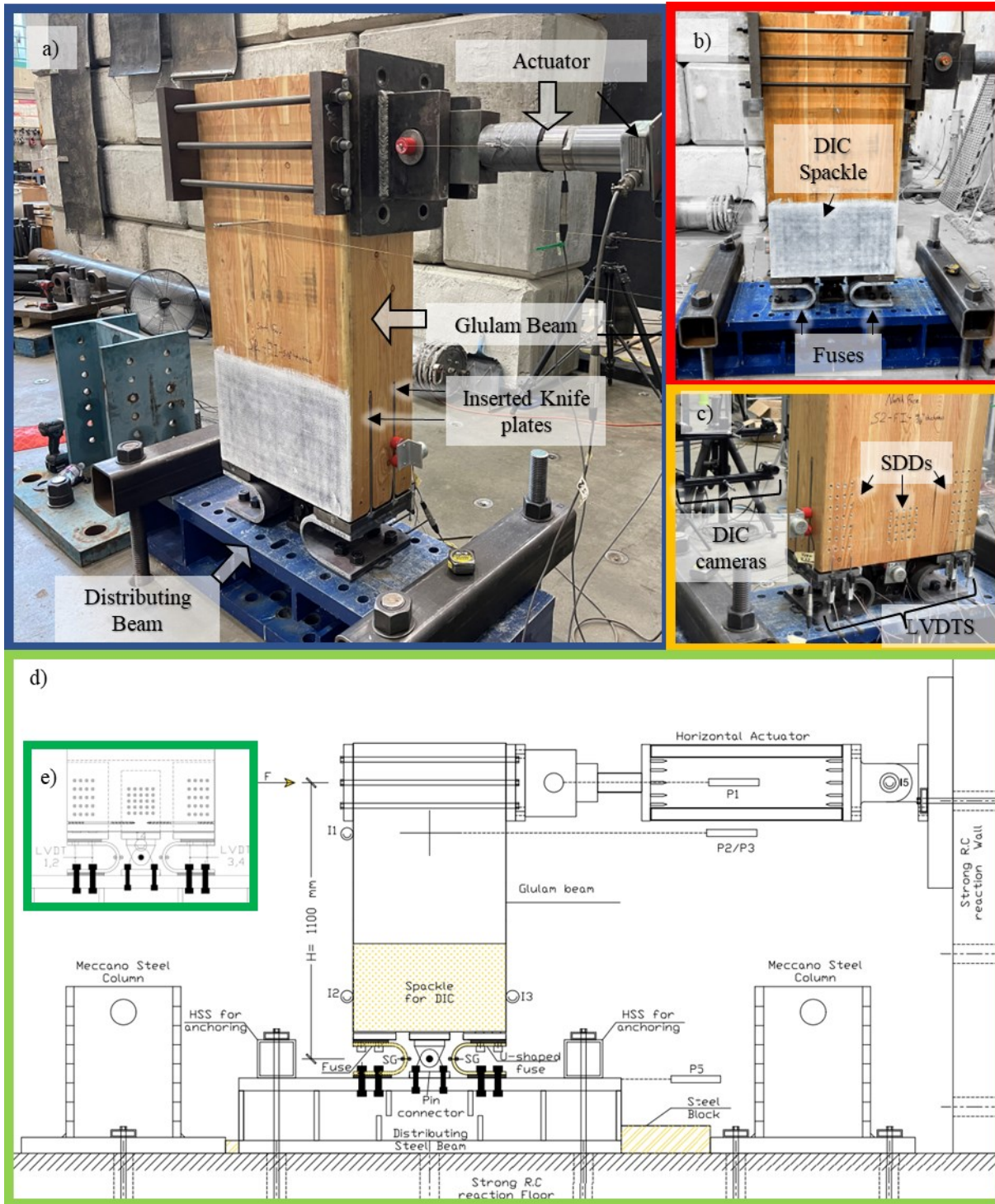


Figure 4-9. Test setup: a) Three-dimensional view; b) Front view; c) Back view; d) Instrumentation plan; e) Fuse instrumentation.

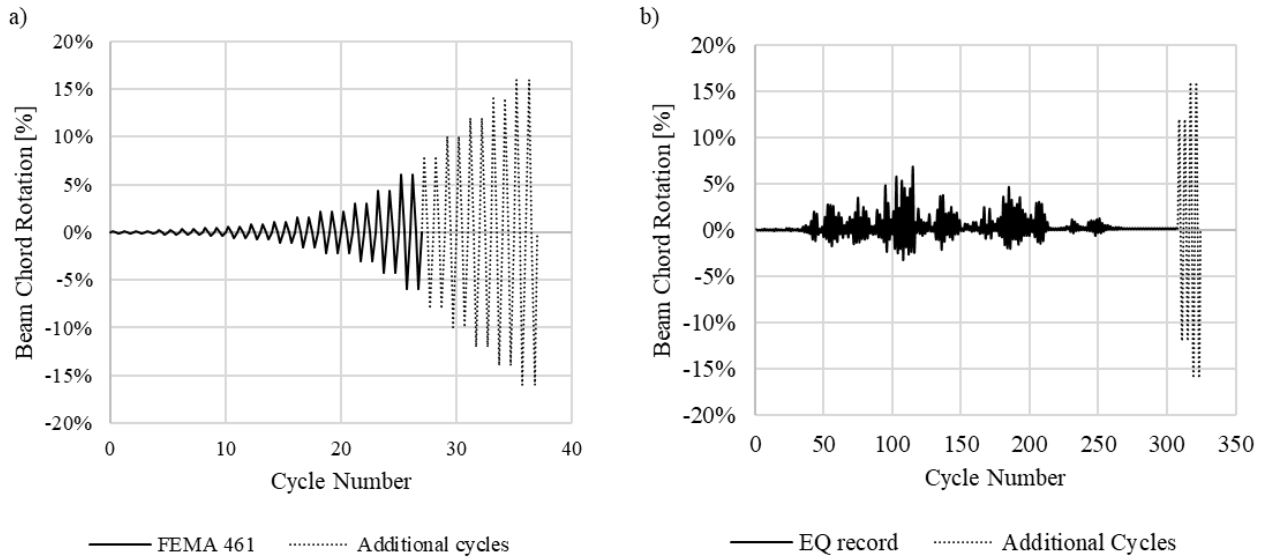


Figure 4-10. Loading protocols: a) FEMA 461 loading protocol proceeded with 10 additional cycles; b) Seismic loading obtained under the Miyagi, Japan 2011 earthquake proceeded with 4 additional cycles.

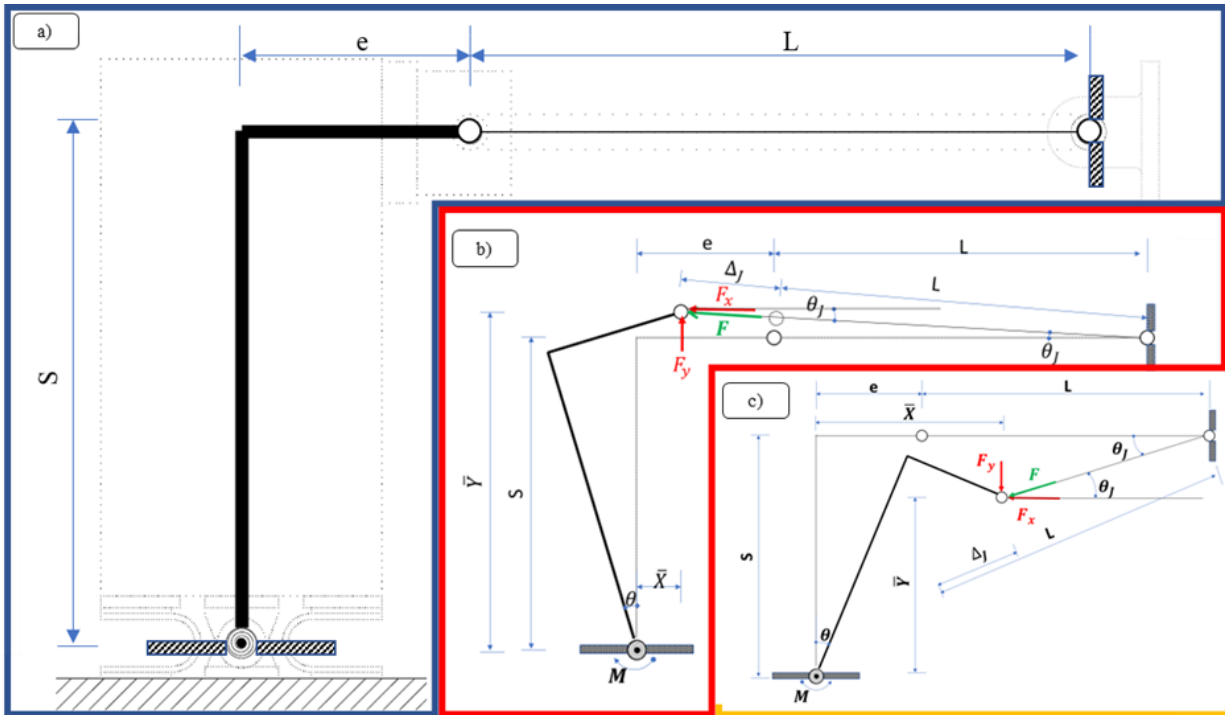


Figure 4-11: Test setup simplified model: a) at rest; b) during actuator push; c) during the actuator pull.

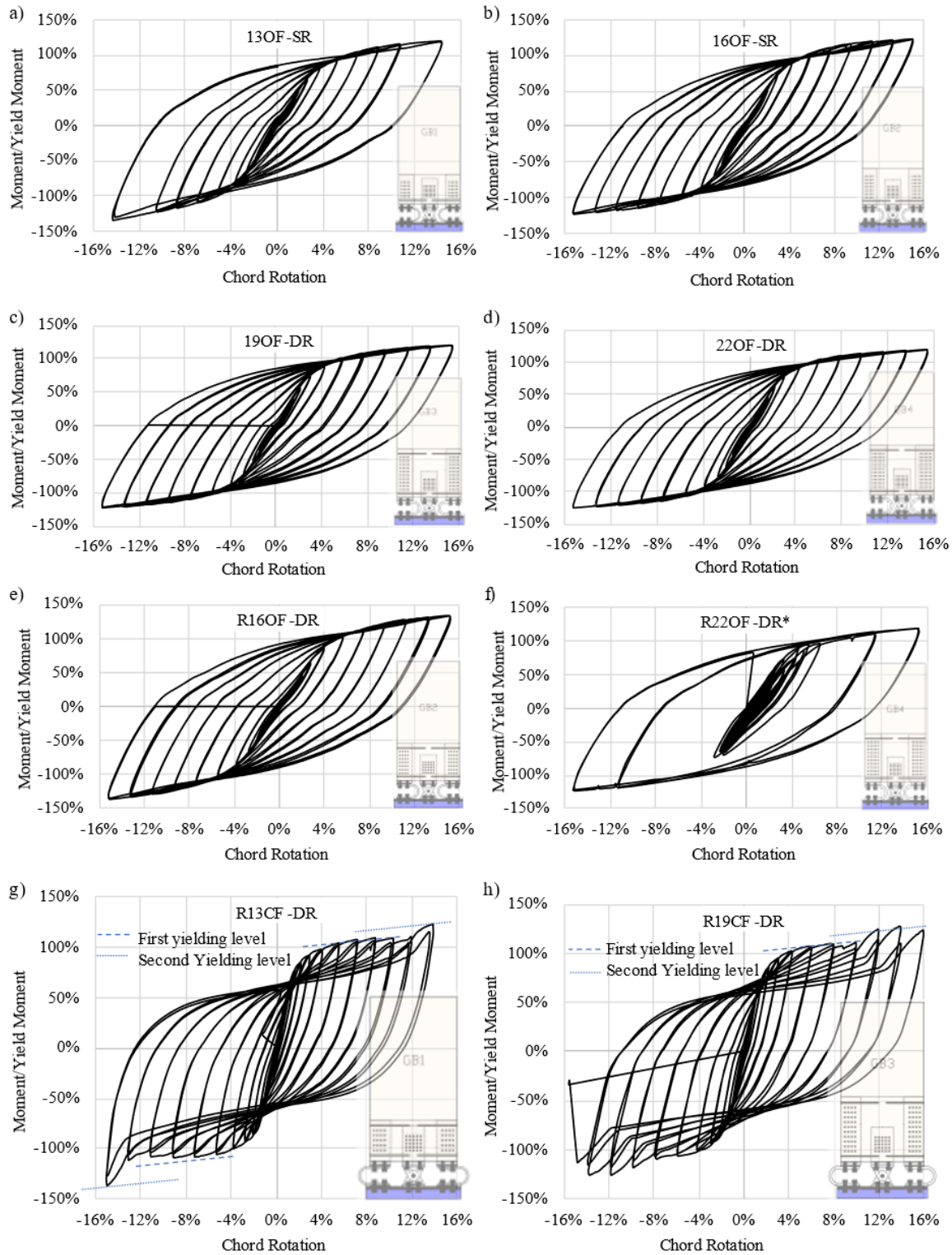


Figure 4-12. Normalized moment-chord rotation responses: a-b) Group I; c-d) Group II; e-f) Group III; g-h) Group IV.

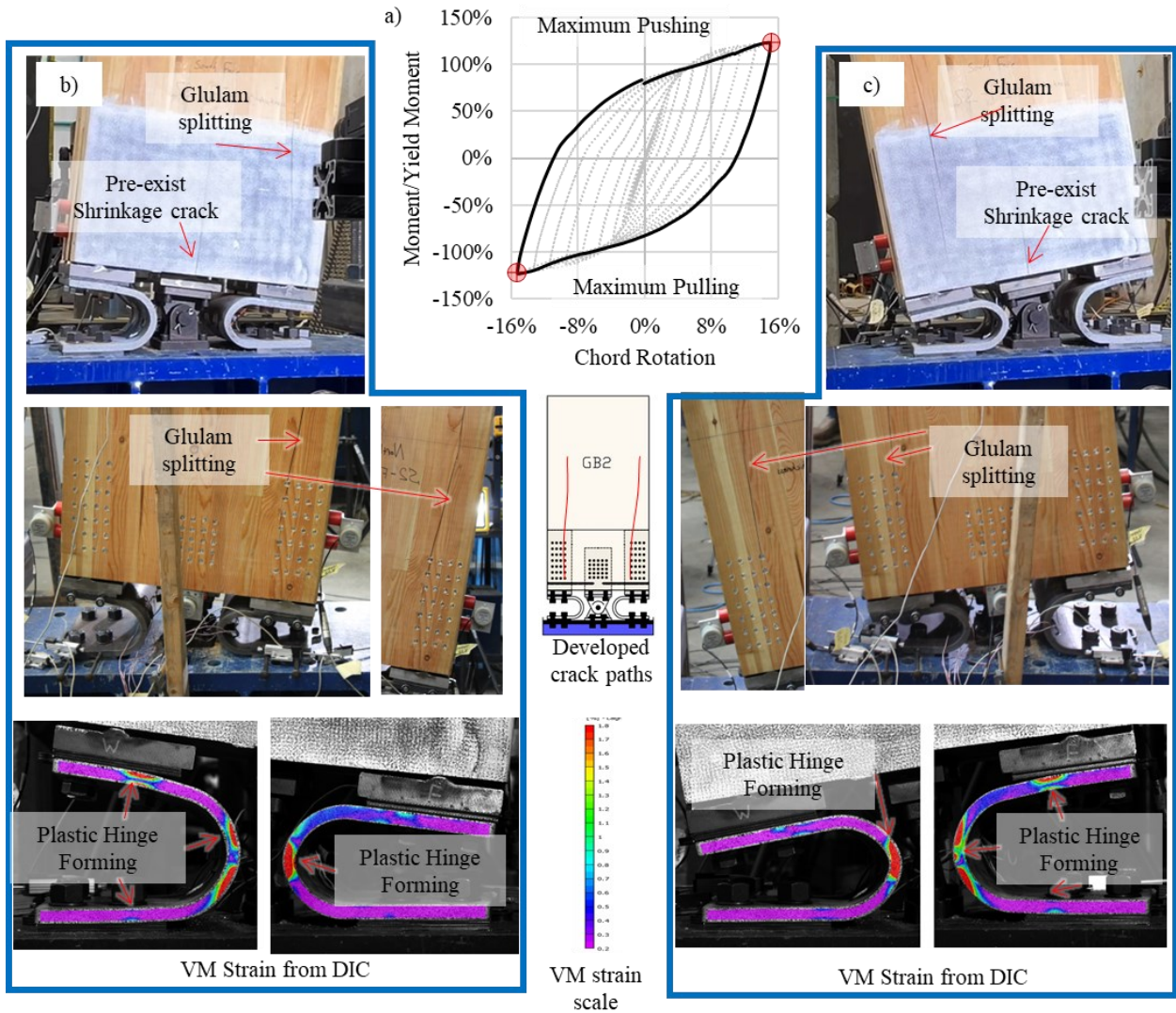


Figure 4-13. Specimen 16OF-SR (Group I): a) 35th cycle of moment-rotation response; b) Positive 15% rotation; c) Negative 15% rotation.

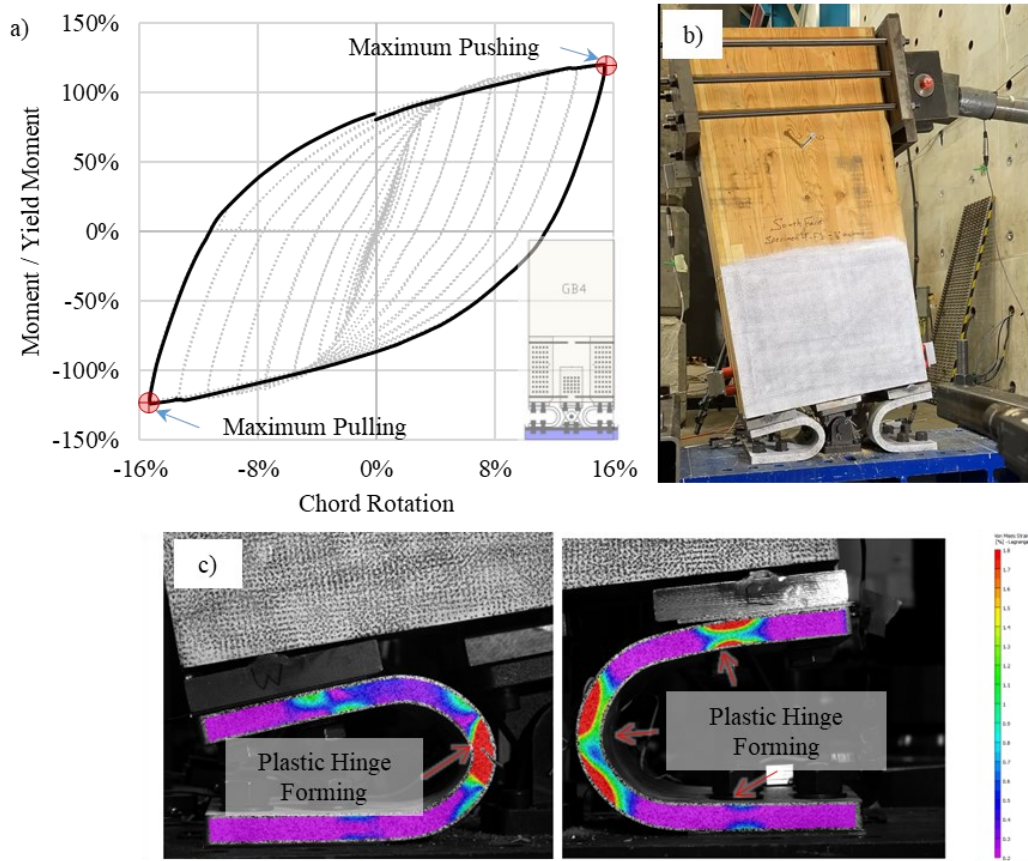


Figure 4-14. Specimen 22OF-DR (Group II): a) 35th cycle of moment-rotation response; b) Specimen deformed-shape at 15% rotation; c) Plastic hinge locations at 15% rotation.

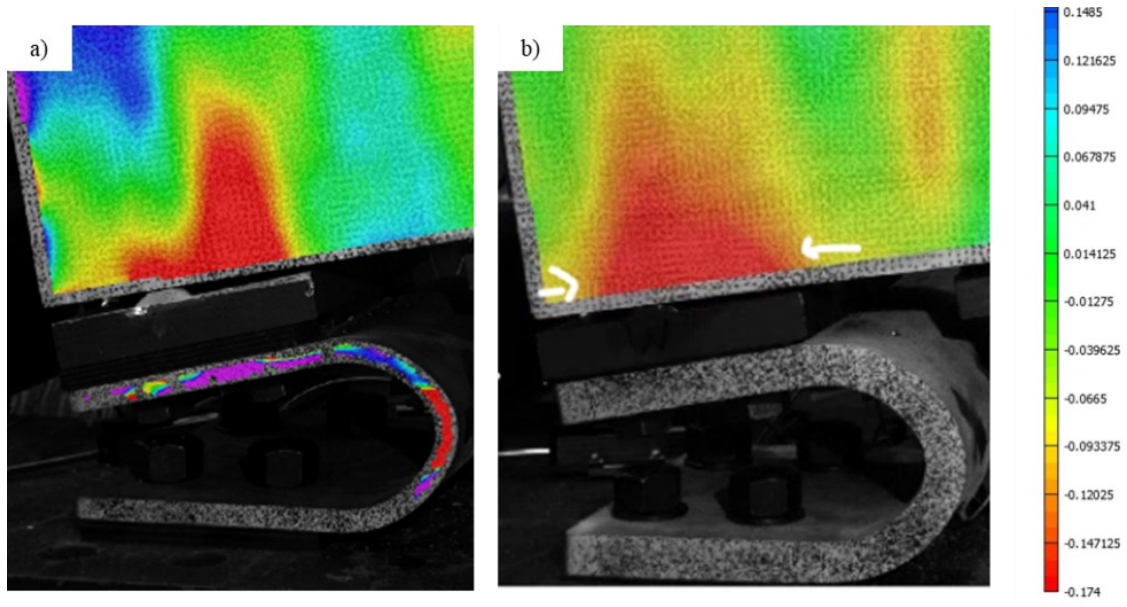


Figure 4-15. Comparison between principal strains: a) Specimen 13OF-SR with single STS reinforcement; b) Specimen 22OF-DR with double STS reinforcement.

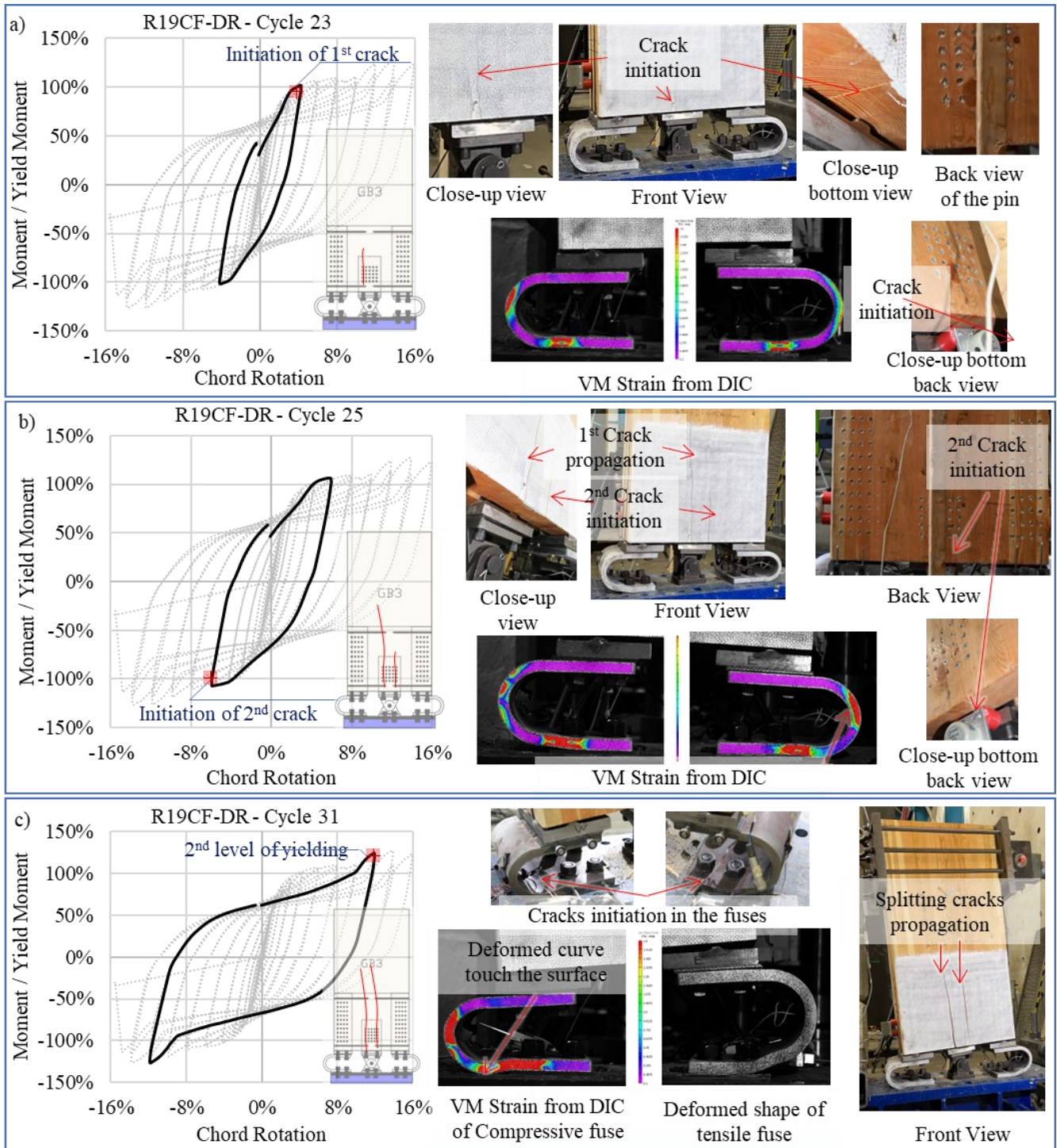


Figure 4-16. Specimen R19CF-DR: a) Fuse yielding and initiation of first splitting crack; b) Initiation of second splitting crack; c) Increase in flexural capacity.

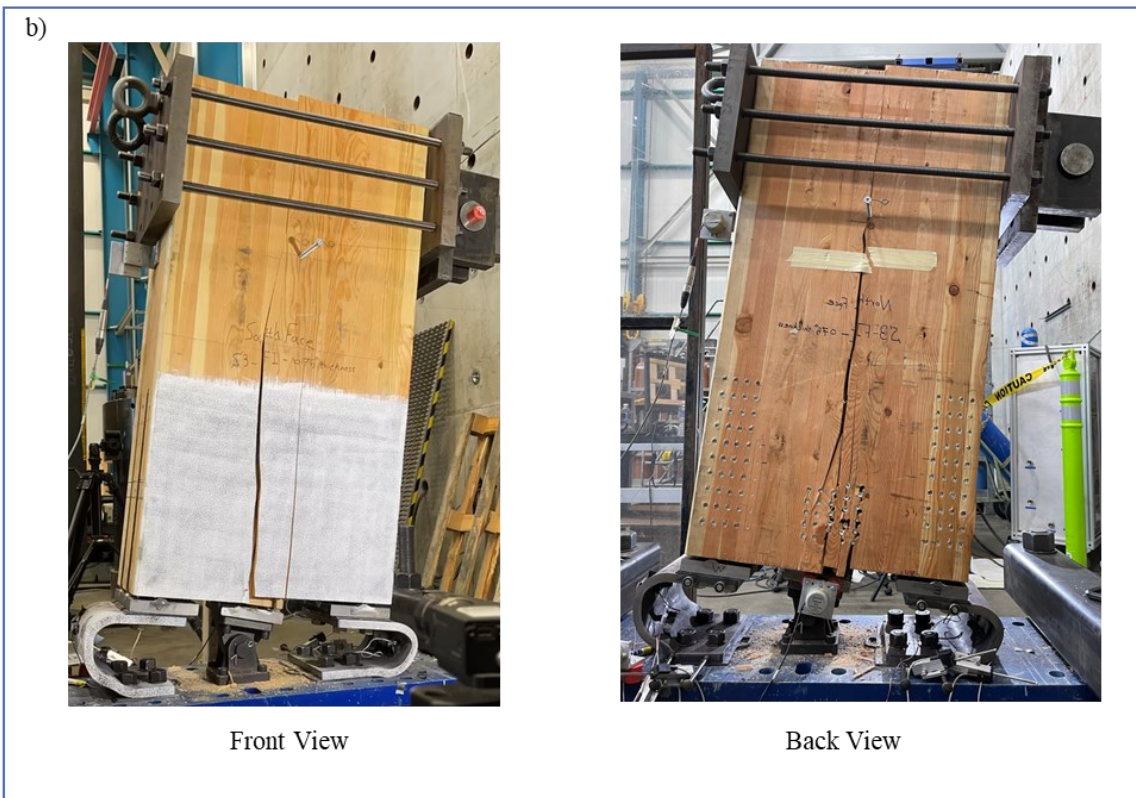
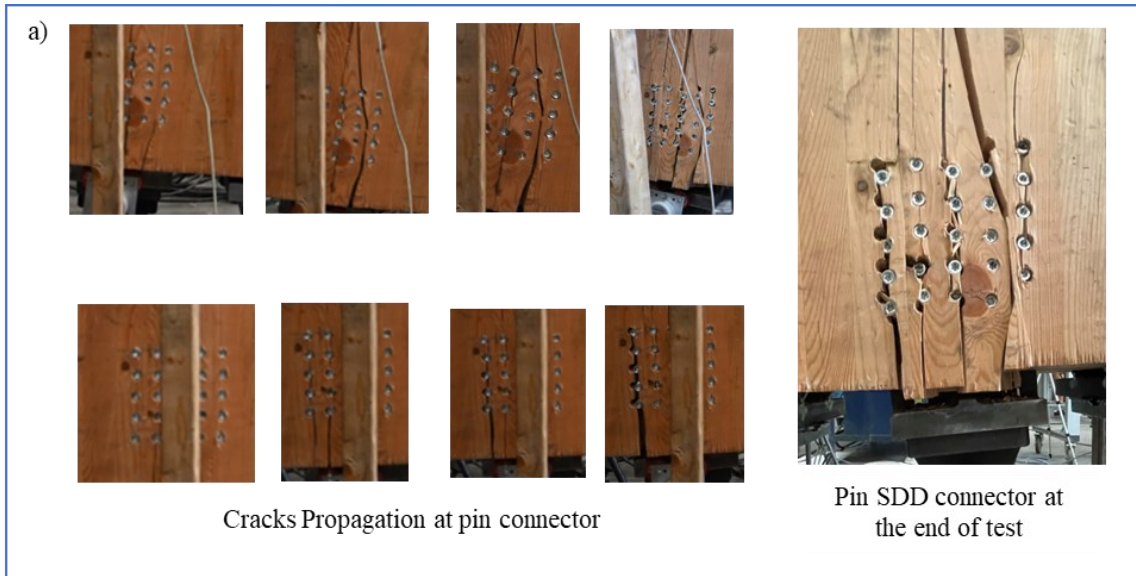


Figure 4-17. Specimen R19CF-DR: a) Crack propagation in the middle SDDs adjacent to the pin connector; b) Global splitting failure at the end of the test.

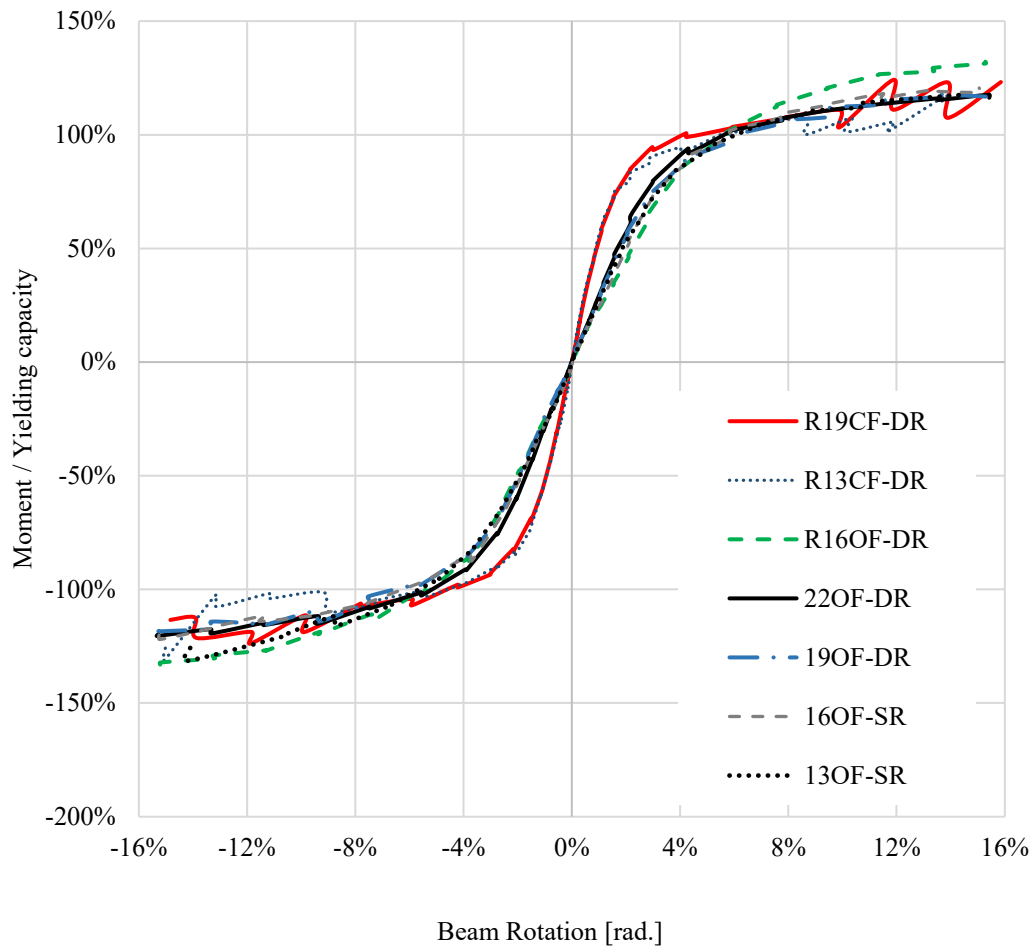


Figure 4-18. Specimen moment-rotation backbone curves.

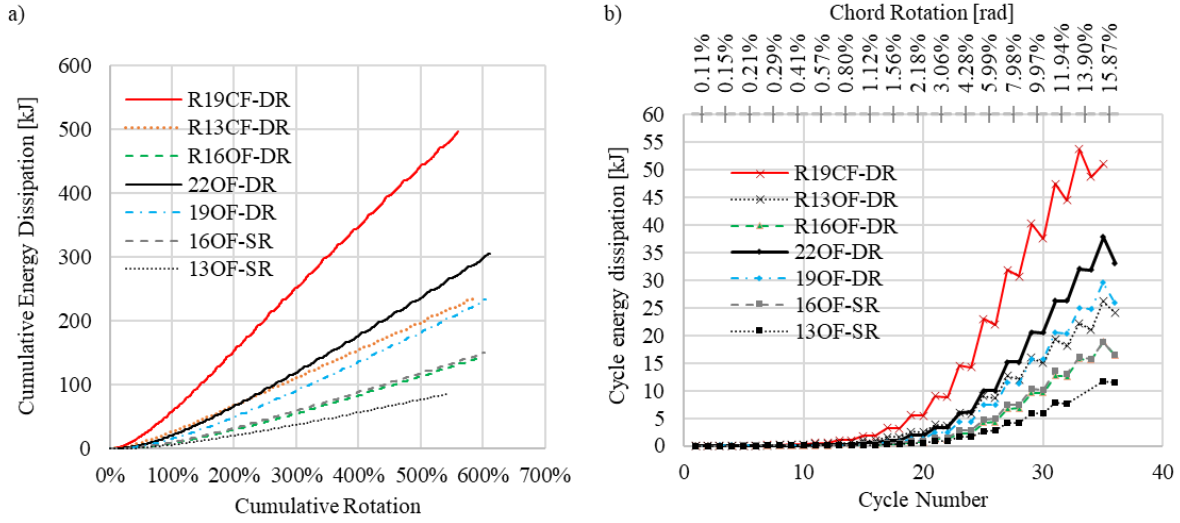


Figure 4-19. Connection energy dissipation: a) Cumulative energy dissipation capacity; b) In-cyclic energy dissipation capacity.

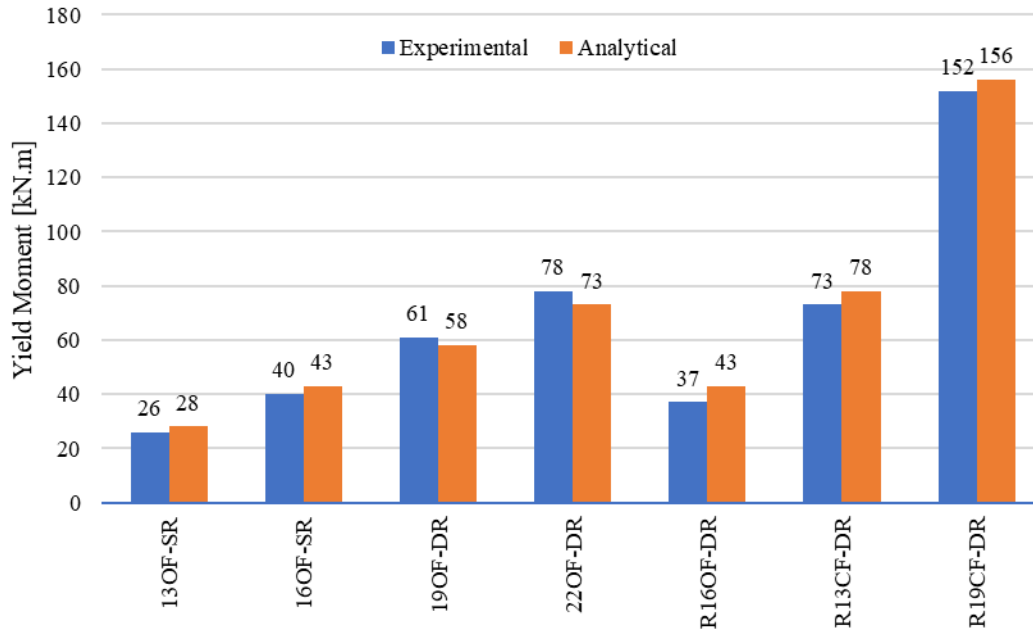


Figure 4-20. Connection yield moment: predicted versus experimental.

5. An Innovative Hybrid Steel-Timber Rocking Seismic Force Resisting System Equipped with U-shaped Fuse Connections *

5.1 Introduction

Hybrid steel-timber structures, combining large ductility and energy dissipation capacity of steel with lightweight and easy-to-construct timber material, offer enhanced structural performance and construction efficiency. Over the past decade, there has been a large body of knowledge created in the area of hybrid steel-timber seismic force resisting systems (SFRSs), including novel connections, structural components, and systems, such as novel timber connectors with integrated steel fuses (Daneshvar et al., 2022; Dong et al., 2021b), steel-timber SFRSs (Tesfamariam et al., 2014a; X. Zhang et al., 2016), and hybrid steel-timber structures (Gilbert & Erochko, 2019; Mowafy et al., 2021).

The 1994 Northridge earthquake underscored the crucial role of SFRSs for life safety, despite the challenges of extensive damage and post-event rehabilitation costs (Uang & Bruneau, 2018). The 2010-2011 Christchurch earthquakes, however, emphasized the need for quick recovery and cost-effective solutions for buildings subjected to seismic loading (Goldsworthy, 2012). Consequently, there is an increasing demand for resilient design solutions that ensure structural safety while minimizing service disruptions after major seismic events (Pampanin et al., 2011; Y. Zhang et al., 2022). One of the advanced solutions to achieve resilience is the rocking braced frame system, which allows column uplift during strong ground motions (Zhong & Christopoulos, 2022).

* The content of this chapter is being prepared and will be submitted as a journal manuscript.

Self-centring systems have evolved significantly over time, with research studies focusing on rocking benefits (Clough & Huckelbridge, 1977), uplifting and vertical force impacts (Housner, 1963; Pollino & Bruneau, 2004), and three-dimensional effects of uplifting elements on floor framing (Lu, 2004). Novel solutions, such as yielding base plates (Azuhata et al. 2006) and hydraulic dampers at column bases (Tremblay et al. 2008), were developed. Wada et al. 2001 and Wiebe and Christopoulos 2009 developed steel-braced frames with multiple uplifting points, while Pollino and Bruneau 2004 and Roke et al. 2009 introduced a similar approach within a rocking-braced frame. Past studies also introduced controlled rocking joints (Pollino & Bruneau, 2004; Wiebe et al., 2012) and self-centring systems (Eatherton & Hajjar, 2011), which contributed to advancing the state of knowledge in the area of rocking systems.

Leveraging the power of large-scale experimental testing (Eatherton, 2010; Sause et al., 2010; Eatherton, 2014), seismic design guidelines, including performance-based design methodologies, were developed for self-centring systems with replaceable fuse elements (Dyanati et al., 2015; Eatherton, 2014; Ma, 2010; Wiebe & Christopoulos, 2015b, 2015a).

Self-centering systems have been effectively employed in mass timber structures. One such application involves integrating U-shaped flexural plates with Laminated Veneer Lumber (LVL) or Cross-Laminated Timber (CLT) walls to create controlled rocking heavy timber walls that enhance seismic resilience (A. Iqbal et al., 2015; Kovacs & Wiebe, 2016). An approach utilizing resilient slip friction joints as energy dissipaters was employed to enhance the overall stability of the structures (Hashemi et al., 2020). A self-centring steel-timber hybrid shear wall was proposed to combine a Post-Tensioned (PT) steel frame with a light wood frame shear using slip friction dampers as energy dissipaters (Cui et al., 2020).

This paper proposes an innovative hybrid steel-timber rocking braced frame (STRBF) system for mid-rise buildings where a mass timber frame is connected to a rocking braced steel frame that aims to improve structural performance, reduce damage to structural and non-structural elements, and achieve a resilient SFRS that can reposition itself following a major seismic event. The use of the U-shaped fuses prevents the lateral load-resisting braced steel frame from inducing significant bending moments in the gravity load-resisting mass timber frame. In this paper, the proposed system combines a timber frame with incorporated energy dissipation devices, namely U-shaped fuses, and a steel concentrically braced frame (CBF) with columns that are allowed to rock. The system also consists of a self-centring feature through PT strands designed to reposition the structure after a major seismic event. The proposed system is first introduced, followed by a performance-based design procedure. A numerical model of a prototype frame consisting of STRBF is developed and employed to validate the proposed design method, particularly the design of seismic fuses, PT strands, and steel members. The numerical model is also used to examine the seismic performance of the system.

5.2 Proposed hybrid steel-timber rocking braced frame

5.2.1 System components

The proposed hybrid steel-timber rocking braced frame (STRBF) system combines a mass timber frame with incorporated energy dissipation devices (U-shaped fuses) and a steel CBF involving rocking columns, as shown in Figure 5-1a for a five-storey structure with three equal-span bays in each principle direction. The CBF consists of tension-compression steel braces in a chevron configuration connected to the mass timber frame through the proposed U-shaped joints, which comprises CLT floor panels glulam beams (GB) and glulam columns (GC). Distributing the fuses

vertically instead of concentrating them at the bottom offers multiple advantages, including isolating the gravity load-resisting system, enhancing redundancy, and better distribution of plasticity throughout the structure. The self-centring capability is provided to the proposed system through vertical PT strands located along the braced frame bay, as shown in Figure 5-1a. The U-shaped joint, shown in Figure 5-1b, comprises a mild steel pin connector and two cold-bent U-shaped steel fuses to resist the applied shear flexural bending, respectively. These components are attached to a GB using structural bolts, an end T-plate, and self-drilling dowels (SDD), as shown in Figure 5-1c. U-shaped plates are expected to dissipate seismic energy through bending and act as sacrificial elements of the system, ensuring the remaining structural elements, including the timber beam, connection plates, and fasteners, remain elastic under the expected seismic force. The pin connector provides a pure hinge condition between the timber beam and steel column to accommodate relatively high rotational demands expected under large storey drifts (e.g., 2%). A sample moment–rotation response of U-shaped connections as obtained from pre-qualification experimental testing described in Chapter 4 is given in Figure 5-1c.

5.2.2 Design methodology and performance objectives

The proposed performance-based design methodology and associated performance objectives to size the elements of the STRBF under seismic loading are described here. The lateral response of the system is a function of the rotational demand in the U-shaped fuses, which include those adjoining the rocking column (left column in Figure 5-2a), referred to as rocking fuses (RF), and those connected to the opposite column, called counter rocking fuses (CRF), as shown in Figure 5-2a.

The idealized deformed shape of the STRBF under lateral loads is shown in Figure 5-2b. Assuming a rigid body motion for the rocking frame and neglecting the influence of column deformations and gravity loads on the rotational demand, the correlation between the system uplift, θ , and the fuse rotation, ϑ , can be determined as $\vartheta_{RF} = 2\theta$ for the RF and $\vartheta_{CRF} = \theta$ for the CRF. The rotational demand on the rocking fuses involves the rotation due to frame rocking plus the beam flexural rotation, whereas, only the beam rotation is present on the counter rocking fuses. Note that the flexural stiffness of the U-shaped connection is ignored in these relationships as it is relatively small compared to the overall system stiffness. Using the free body diagram of the STRBF shown in Figure 2b, the forces imposed on the braced frame can be found as those causing overturning, M_{om} and those counteracting (or balancing) the overturning moment, M_{bm} . The source of the overturning moment is the inertia forces at each storey, F_1 to F_5 , caused uplift displacement, Δ_u , while the balanced moment is produced by the forces in PT strands, F_{PT} , rocking fuse moment, M_{RF} , counter rocking fuse moment, M_{CRF} , and vertical reaction, P_{RF} . The vertical reaction developed because of the RF moment on glulam beams, as shown in left side of Figure 2c, is computed as $P_{RF} = M_{RF}/L$ where L is the glulam beam span. The same applies to the CRF shown in right side of Figure 2c. The counter-rocking fuse moment in the elastic range is obtained as $M_{CRF} = M_{RF}/2$.

Figure 5-2d shows the idealized moment versus uplift rotation of the STRBF system relative to the response of each system component that contributes to the nonlinear response of the overall system. Referring to this figure, the points on the system curve encompass (1) initial uplift, (2) rocking fuse yielding, (3) counter rocking fuse yielding, (4) onset of yielding in PT strands, (5) ultimate capacity of PT strands leading to the loss of full self-centring capability, and (6-7) strength degradation, which could be the result of PT strand fracture, fuse fracture, or frame collapse.

The design methodology proposed herein aims to ensure the building is functional immediately after frequent earthquakes, e.g., seismic hazard with a probability of exceedance of 10% in 50 years, and prevent collapse under rare (design-level) events, e.g., seismic hazard with a probability of exceedance of 2% in 50 years. Therefore, the focus of the design method is primarily on the first four performance objectives (1-4). The corresponding system moments are denoted as M_{upi} , M_{y1} , M_{y2} , and M_m , respectively, while the associated uplift angles are indicated by θ_{upi} , θ_{y1} , θ_{y2} , and θ_m .

The ultimate overturning moment $M_{ot,u}$, which represents a moment that causes the system to rock, is obtained from the inertia forces calculated using the equivalent static force procedure as follows:

$$M_{ot,u} = \sum_{i=1}^{roof} F_i h_i \quad (\text{Equation 5-1})$$

where, F_i is the inertia force at storey i , and h_i is the height of storey i from the base level. The ultimate overturning moment is verified against the factored balancing moment, $\phi M_{bm,n}$, which is the moment produced by PT strands and connections as (ϕ is the resistance factor equal to 0.9):

$$M_{bm,n} = F_{PT0} D_{PT} + n(M_{RF,y} + P_{RF} A + M_{CRF,E}) + P_D A \quad (\text{Equation 5-2})$$

where n is the number of storeys, F_{PT0} is the initial pretension force in the PT bars, D_{PT} is the horizontal distance between the PT bar and the point about which overturning is computed, $M_{RF,y}$ is the yielding moment of the rocking fuse, $M_{CRF,E}$ is the elastic moment of CRF developed when the RF yields, P_D is the gravity load imposed on the uplifting column at each floor level, and A is

the bay width. It should be noted that the gravity load associated with the mass timber frame is neglected in (Equation 5-2 due to its relatively lower weight.

The self-centring ratio (SCR) is a term used in self-centring systems designed to return to their original position after an earthquake or other external force. The SCR is defined as the ratio between the contribution of the self-centring components to the non-self-centring system in the balanced moment. Two SCRs, SC1 and SC2, are defined as follows to evaluate the self-centring capability of the system before and after the yielding of CRFs, respectively.:

$$SC1 = \frac{F_{PT0}D_{PT} + n \cdot M_{CRF,E} + P_D A}{n(M_{RF,y} + P_{RF}A)} \quad (\text{Equation 5-3})$$

$$SC2 = \frac{F_{PT,FY}D_{PT} + P_D A}{n(M_{RF,y} + P_{RF}A + M_{CRF,y})} \quad (\text{Equation 5-4})$$

where, $F_{PT,FY}$ is the pre-tensioning force in the PT bars when rocking fuses yield, $M_{CRF,y}$ is the yielding moment of CRF. For the proposed system, the SCR should be between two boundary scenarios, SC1 and SC2, defined by the behaviour of the CRF. In SC1, RF yields, while CRF remains elastic, contributing a half-yielding moment to the self-centring force. SC2 represents the extreme case, assuming a yielded CRF contributes a full-yielding moment to energy dissipation. This scenario enhances the system's ED capability while reducing its SC ratio. However, due to cyclic loading and residual deformations, SC2 might occur earlier than anticipated. The ratios SC1 and SC2 should remain between 1.0 and 3.0 to ensure self-centring capability and sufficient energy dissipation of the system. These ratios compare the moment resistance developed by the components that are expected to remain elastic under 2.5% drift, such as post-tensioning bars and CRF, to the moment resistance produced by yielding fuses. Higher SCRs enhance the system's ability to return to its pre-excitation configuration after an earthquake, thereby minimizing residual deformation. However, there is a trade-off between SCRs and the energy dissipation capability of

the system. Higher SCRs can potentially result in a reduced energy dissipation capacity and excessive storey drifts. The energy dissipation capacity of the STRBF can be calculated as:

$$ED = \alpha_d \frac{n(M_{RF,Y} + P_{RFA})}{F_{PT0}D_{PT} + P_{DA} + n(M_{CRF,E} + M_{RF,Y} + P_{RFA})} \quad (\text{Equation 5-5})$$

where α_d denotes the degrading fuse factor, which is taken as unity in the case of a non-degrading fuse, such as the U-shaped fuse used here. The relationship between SCR and ED is then defined as:

$$ED = 1 - \frac{SC}{1 + SC} \quad (\text{Equation 5-6})$$

The peak drifts in these systems do not have a direct linear relationship with ED values; rather, they show less sensitivity, with a change in peak drifts being less than 25% for each unit change in ED (Eatherton & Hajjar, 2011). Hence, a SC ratio of 3, corresponding to ED = 25%, is considered the upper limit, while a ratio of 1.5, corresponding to a ED = 40%, is recommended for initial strength checks (Eatherton, 2010).

5.3 Prototype building design

5.3.1 Geometry and seismic design parameters

A five-storey office building located in Vancouver, British Columbia, a high seismic region in Canada, on site Class C, was selected to demonstrate the design and examine the seismic response of the STRBF. The building is square in plan, with three identical 5-m long spans in each principal direction. On each exterior wall of the building (Figure 5-1), the interior bay consists of steel CBF while timber frames are used in two exterior bays. The height of each storey is 4.0 m, except the first storey, which stands at 4.2 m.

All the loads were calculated in accordance with the 2015 National Building Code (NBC) of Canada (National Research Council of Canada, 2010). The dead and live loads of the floors are 0.83 and 2.4kPa, respectively. The timber frames, shown in Figure 5-1a, support CLT panels that rest on secondary and primary glulam beams. GCs are used to collect the loads from the main GBs. The timber members were sized per the Canadian wood design standard, CSA O86 (CSA, 2019a). The selected cross-sections for timber components include 87 V for CLT panels used, 80mm × 380mm for secondary GBs, 215mm × 266mm for interior GBs, 365mm × 608mm for outer GBs, and 215mm × 342mm for GCs. Note that the design of outer GBs connected to the CBF is influenced by the SFRS design to accommodate the induced flexural moment in the U-shaped connection during rocking as will be described later.

The seismic behaviour of the proposed STRBF involves two phases, initial rigidity (before uplift) and subsequent energy dissipation (after uplift). In the early stage, the system's rigidity is expected to be akin to that of a reinforced concrete shear wall, favouring the use of the respective equation ($T_a = 0.05 H^{0.75}$) for estimating the structure's fundamental period, T_a , knowing the structure's total height, H. As the rocking phase commences, the system's ductile behaviour starts mirroring steel Eccentrically Braced Frames (EBFs) (Ma 2010), making it suitable to employ EBF ductility and overstrength-related modification, $R_d = 4.0$ and $R_o = 1.5$, respectively. The design fundamental period of the structure using the NBC equation for reinforced concrete shear walls is $T_a = 0.61s$ resulting in a design spectral acceleration of $S_a = 0.659g$ under a hazard level corresponding to a 2% chance of exceedance in 50 years. The importance factor is $I_E = 1.0$, and the factor accounting for higher mode effects is $M_v = 1.0$. The seismic weight of the structure is 1611 kN. The design seismic base shear per STHRF determined using the equivalent static force procedure is 809 kN, including the effects of P- Δ notional loads and accidental torsion.

5.3.2 Seismic design of prototype STRBF

Figure 5-3 outlines the key seismic design steps for the STRBF. Design forces for system components are determined using overturning moment and design base shear. The SCRs, which reveal the capacity of the structure to return to its original position post-earthquake, are then calculated. A trade-off between self-centring and energy dissipation capacities dictates the initial post-tensioning force and U-shaped fuse design forces. Steel CBF members are finally sized to carry the capacity of U-shaped fuses.

Step 1: Determine component design forces.

To determine member forces, the self-centring ratios should first be set. When the STRBF is part of the gravity system, the contributions of gravity loads can be leveraged to self-centre the structure (Pollino 2015, Mottier et al. 2018, 2019) by computing the SCR as:

$$SC1 = \frac{0.5(n \cdot M_{RF,y}) + P_D A}{(n \cdot M_{RF,y})(1 + A/L)} \quad \text{where} \quad n \cdot M_{RF,y} = \frac{[M_{ovt,u}/\phi - P_D A]}{1.5 + A/L} \quad (\text{Equation 5-7})$$

For the proposed STRBF, the SC1 ratio is $0.184 < 1.0$, confirming that the self-centring capacity provided is insufficient and the need to incorporate PT strands to reposition the structure after an earthquake. The initial post-tensioning force of the strands can therefore be computed as:

$$F_{PT0} \geq \frac{SC1 - 0.5/(1 + \frac{A}{L})}{(1 + SC1)} \frac{M_{ovt}}{\phi D_{PT}} - \frac{P_D A}{D_{PT}} \quad (\text{Equation 5-8})$$

Assuming an $SC1 = 1.5$ strikes a balance in the trade-off between self-centring and energy dissipation capacities. This value offers a reasonable SCR while ensuring an adequate energy dissipation capacity ratio of 40%. The U-shaped fuse design force is then determined as:

$$n. M_{RF,y} \geq \frac{1}{(1 + SC1)(1 + \frac{A}{L})} \frac{M_{ovt}}{\phi} \quad (\text{Equation 5-9})$$

Step 2: Size post-tensioning strands

Once the initial post-tensioning force is determined, the number of PT strands required is determined based on their pre-stress level, i.e., the amount of stress applied to strands before they are subjected to any additional external forces, and yielding uplift ratio denoted as θ_m . By setting θ_m as 2.5%, which corresponds to the interstorey drift limit prescribed by NBC, the maximum initial pre-stress level, η_{max} , to ensure PT strands fracture upon maximum interstorey drift angle can be calculated as:

$$\eta_{max} = \frac{f_y}{f_u} - \frac{E_{PT} D_{PT}}{f_u L_{PT}} \theta_m \quad (\text{Equation 5-10})$$

The initial pre-stress level, η_0 , is then chosen so that it does not exceed η_{max} :

$$\eta_0 = \frac{f_0}{f_u} \quad (\text{Equation 5-11})$$

in which f_0 and is the initial stress in PT strands and f_u is their ultimate strength. The number of PT strands, N , is therefore obtained as:

$$N = \frac{F_{PT0}}{\eta_0 f_u A_s} \quad (\text{Equation 5-12})$$

The initial pre-stress level in PT strands should be verified again after rounding up the number of strands to the nearest integer, resulting in the actual pre-stress level, $\eta_{0,act}$:

$$\eta_{0,act} = \frac{F_{PT0}}{N f_u A_s} \quad (\text{Equation 5-13})$$

Once the actual pre-stress level in PT strands is determined, their actual yield uplift ratio, θ_m is computed as follows:

$$\theta_m = 2 \frac{f_u}{E_{PT}} \frac{H}{A} \left(\frac{f_y}{f_u} - \eta_{o,act} \right) > 2.5\% \quad (\text{Equation 5-14})$$

where H is the total height of the frame.

For the design example of Figure 5-1a, an initial post-tensioning force of $F_{PT0} = 257$ kN requires two strands with a diameter of $D = 15$ mm and a cross-sectional area of $A = 353$ mm². These strands have a modulus of elasticity $E = 195$ GPa, a yield strength $F_y = 1676$ MPa, and an ultimate strength $F_u = 1860$ MPa. Additionally, the initial strain in the strands (η_0) is set to 25%, and the stiffness, determined as the product of the modulus of elasticity and the cross-sectional area divided by the height of the building, is calculated to be 40 kN/mm.

Step 3: Size U-shaped fuses

The U-shaped steel fuse connection pre-qualified by (Mowafy et al. 2023), as shown in Figure 5-1c, was used here as the source of seismic-induced energy dissipation in the proposed STRBF. The thickness of the U-shape plates, t , was chosen such that the flexural resistance of the U-shaped connection, $M_{F,y} = wtF_y\xi_{HF} \cdot (h_b - 2e)$, exceeds the applied moment:

$$t \geq \frac{1}{wF_y\xi_{HF} \cdot (h_b - 2e)} \cdot \frac{1}{n(1 + SC1)(1 + A/L)} \cdot \frac{M_{ovt}}{\phi} \quad (\text{Equation 5-15})$$

where h_b is the depth of the connecting beam, as shown in Figure 5-4a, and e is the distance from the fuse leg to the edge of the inner bolts connecting the U-shaped plates to the beam using a knife plate shown in Figure 5-4a. ξ_{HF} is defined as an eccentricity factor for an end-hinged fuse as the leg of the fuse can freely rotate under a perpendicular load., ξ_{HF} is calculated as:

$$\xi_{HF} = \frac{1}{1 + 4l'/t} \quad (\text{Equation 5-16})$$

where l' is the effective fuse span measured vertically from the edge of inner bolts to the farthest point of the bent centreline, as shown in Figure 5-4a.

The required thickness of the U-shaped fuses in the prototype frame of Figure 5-1b is determined through a systematic design process that considers factors such as the desired yield moment and the fuse ductility factor. The dimensions of the U-shaped fuses, including width and length, are chosen based on the physical constraints of the glulam beam and the anticipated structural performance.

The U-shaped fuses in the design example are made of CSA G40.21 44W / 300W steel plates (CSA & Association, 2013), with $F_y = 345$ MPa. The design parameters of the fuse include flexural stiffness $K = 2326$ kN.m/rad, yield moment $M_{F,y} = 78$ kN.m, and ultimate moment $M_{F,u} = 92$ kN.m. This leads to ultimate to yield moment ratio of $M_{F,u}/M_{F,y} = 118\%$. The yield rotation of the fuse (ϑ_y) and its ultimate rotation (ϑ_u) are at 3.34% and 15.40%, respectively. The ductility factor (μ) is finally determined as 4.61. These performance characteristics ensure the selected fuses yield before other structural elements.

The remaining elements of the U-shaped connection are capacity protected. The upper and lower SDD connections are designed to withstand the probable yielding fuse capacity, $P_u = R_y \cdot R_e \cdot P_y$ where R_y is a factor employed to estimate the impact of strain hardening, taken as 1.2 as shown in chapter 3, R_e is an eccentricity factor taken as 1.5, P_y is the yielding capacity of the fuse $= wtF_y\xi_{HF}$. The middle SDD are designed to withstand the vertical reaction force, P_{RF} , as shown in Figure 5-2c. The geometry of the U-shaped connection is kept consistent throughout the height of the frame for simplicity and to ensure uniform seismic performance. However, it is worth noting that in a real-world application, the fuse geometry may be adjusted to account for variations in loading. Once the fuses are sized, the self-centring ratio SC2 (after yielding of counter rocking fuses),

as described in (Equation 5-4. If this ratio falls below 1.0, the PT strand design force should be increased, and larger PT strands should be selected (*Step 2*).

Step 4: Develop moment – uplift rotation curve.

The history of forces in key system elements, i.e., PT and fuses, with respect to uplift ratio, θ , should be defined to understand the nonlinear behaviour of the system in design, which then helps estimate member design forces. The uplift ratios are defined as a function of the fuse connection rotation angle at the yielding of RF and CRF, respectively, $\theta_{y1} = \vartheta_y/2$ and $\theta_{y2} = \vartheta_y$.

Axial forces in PT strands, $F_{PT@θ}$, and flexural moments in the RF and CRF fuses, $M_{RF@θ}$ and $M_{CRF@θ}$, respectively, are then derived at any given uplift ratio, θ , based on their anticipated behaviour in Figure 5-4b as:

$$F_{PT@θ} = F_{PT0} + K_{PT} \cdot \overline{\theta} \cdot \overline{D_{PT}} \quad (\text{Equation 5-17})$$

$$M_{RF@θ} = \begin{cases} K_{fuse} \cdot \overline{2\theta} & \text{for } \theta \leq \theta_{y1} \\ [M_{RF,y} + K_{fuse2} \cdot (2\theta - \theta_{y1})] (1 + A/L) & \text{for } \theta > \theta_{y1} \end{cases} \quad (\text{Equation 5-18})$$

$$M_{CRF@θ} = \begin{cases} K_{fuse} \cdot \overline{\theta} & \text{for } \theta \leq \theta_{y2} \\ [M_{RF,y} + K_{fuse2} \cdot (\theta - \theta_{y2})] & \text{for } \theta > \theta_{y2} \end{cases} \quad (\text{Equation 5-19})$$

in which K_{PT} is the stiffness of the PT strands and K_{fuse2} is the post-yield stiffness of the fuse, as shown in Figure 5-4c.

Now, the idealized moment-rotation response of the system is determined using four critical points (see Figure 5-2d) that represent the first four critical limit states from which the moment values are obtained as follows:

$$M_{upi} = F_{PT0}D_{PT} \quad (\text{Equation 5-20})$$

$$M_{y1} = F_{PT,y1}D_{PT} + n.M_{F,y}(1.5 + A/L) \quad (\text{Equation 5-21})$$

$$M_{y2} = F_{PT,y2}D_{PT} + n.M_{RF,y2}(1 + A/L) + n.M_{F,y} \quad (\text{Equation 5-22})$$

$$M_m = F_{PT,y}D_{PT} + n.M_{RF,m}(1 + A/L) + n.M_{CRF,m} \quad (\text{Equation 5-23})$$

where $F_{PT,y1}$ is the force in PT strands at θ_{y1} , $F_{PT,y2}$ is the force in PT strands at θ_{y2} , F_{PTY} is the yielding force of the PT strands, $M_{F,y}$ is the yielding moment of the U-shaped connection, as described earlier, $M_{RF,y2}$ is the moment in RF fuses at θ_{y2} , $M_{RF,m}$ is the moment induced in the fuses at the PT yielding uplift ratio, θ_m .

Step 5: Estimate the maximum uplift ratio.

The maximum frame uplift ratio under design level hazard is calculated following Direct Displacement-Based Design (DDBD), which uses an idealized Single Degree of Freedom (SDOF) model (Ma, 2010). The derived maximum uplift ratio, θ_e , for the frame example is 2.4%, which is deemed acceptable as it is less than the allowable maximum drift of 2.5%, prescribed by the NBC of Canada (Structural Commentaries, 2015).

Step 6: Estimate member forces

The seismic-induced forces in the members, including steel beams, steel braces, and steel columns, are estimated under a specific loading condition. This condition involves lateral inertia forces impacting each floor and vertical loads originating from the point load imposed by the post-tensioning (PT) strands and the fuse. The forces in PT, F_{PTE} , plus the moments in RF and CRF fuses, $M_{RF,e}$ and $M_{CRF,e}$, at a maximum uplift ratio, θ_e , are:

$$F_{PTE} = F_{PT0} + K_{PT} \cdot \overbrace{\theta_e \cdot D_{PT}}^{\Delta_{PT,e}} \quad (\text{Equation 5-24})$$

$$M_{RF,e} = [M_{RF,y} + K_{fuse2} \cdot (2\theta_e - \theta_{y1})] (1 + A/L) \quad (\text{Equation 5-25})$$

$$M_{CRF,e} = \begin{cases} K_{fuse} \cdot \theta_e & \text{where } \theta_e \leq \theta_{y2} \\ M_{RF,y} + K_{fuse2} \cdot (\theta_e - \theta_{y2}) & \text{where } \theta_e > \theta_{y2} \end{cases} \quad (\text{Equation 5-26})$$

Inertia forces developed at the floor levels upon rocking θ_e are determined using an empirical approach proposed by (Ma 2010) as follows:

i) Calculate the maximum expected overturning moment, $M_{ot,max}$:

$$M_{ot,max} = F_{PTe} \frac{A}{2} + M_{RF,e} + M_{CRF,e} \quad (\text{Equation 5-27})$$

ii) Calculate the maximum expected base shear, V_{max} :

$$V_{max} = \frac{M_{ot,max}}{\alpha H} \quad (\text{Equation 5-28})$$

in which $\alpha = 1/a$ is the equivalent single load height ratio calculated from a regression analysis assuming $a = H/A$ as the frame aspect ratio.

iii) Compute the peak inertia force at the roof, F_{roof} :

$$F_{roof} = \alpha_F V_{max} \quad (\text{Equation 5-29})$$

where $\alpha_F = \frac{1.1}{\sqrt{n}}$ is the roof load to base shear ratio, and n is the number of storeys.

iv) Determine the peak inertia force at each floor, F_{floor} :

$$F_{floor} = \frac{V_{max} - F_{roof}}{n - 1} \quad (\text{Equation 5-30})$$

Once the lateral inertia forces are found, the force demands in STRBF members, including beams, braces, and columns, are determined using a linear analysis assuming a frame with pinned bases, which is necessary to balance the base reactions as lateral inertia forces impose a net overturning

moment on the frame. Seismic-induced forces computed here, together with forces imposed by gravity loads, are used to size the steel CBF members per CSA S16 (CSA, 2019b). HSS152×152×7.9 braces are selected for the roof level, whereas HSS114×114×6.4 braces are used in the Storeys 2-4, and HSS127×127×6.4 braces are chosen for the first storey. The braces are in conformance with ASTM A1085 with a yield strength of $F_y = 345$ MPa (ASTM, 2013). The beams and columns are chosen from wide-flange sections conforming to ASTM A992 steel with $F_y = 345$ MPa (ASTM, 2015). The beam sections comprise of W100×19.3 sections in all storeys. W360×79 columns are used for all storeys. They are continuous along the height of two storeys with a splice connection at Storey 3.

5.4 Verification of the design method

5.4.1 Numerical model development

The proposed design method for the STRBF is verified here by evaluating the seismic performance of the system using a three-dimensional fibre-based numerical model created in the *OpenSees* program (Gregory L. Fenves, 2009; McKenna et al., 2010). The numerical model is shown in Figure 5-5a. Due to symmetry in the plane, only one-half of the building was simulated, assuming that CLT panels supply sufficient rigidity in the plane of floors and the roof, allowing an even distribution of seismic inertial forces between STRBFs. The interior timber columns carrying gravity loads are not explicitly simulated; instead, their respected masses are lumped on the adjacent exterior columns. Moreover, the gravity loads tributary to these interior timber columns are imposed on a lean-on column coupled in the horizontal translation at each floor to the main STRBF.

The beams, columns, and braces of the timber system and the steel CBF are simulated using elastic beam-column elements. The nonlinear cyclic response of U-shaped fuse connections was reproduced using a zero-length rotational spring with a Giuffre-Megnetto-Pinto material model represented as steel02 uniaxial material model (Filippou et al., 1983) in OpenSees. The Steel02 parameters were obtained by calibrating the moment-rotation response of the spring against the experimental test data from U-shaped connections performed by the authors, as shown in Figure 5-5b. The parameters consist of the yield moment, $M_{F,y} = 79$ kN.m, rotational stiffness, $K_{fuse} = 2326$ kN.m/rad, strain hardening ratio representing the post-yield stiffness $b = 0.0591$, initial elastic hardening modulus $Ro = 25$, elastic-to-plastic transition parameter, $cR1 = 0.925$, and isotropic hardening rate parameter, $cR2 = 0.15$. A relatively rigid material was assigned to other DOFs of the spring simulating the fuse. Referring to Figure 5-5b, a very good agreement was found between the numerical prediction and the experimental results, which confirms the capability of the proposed spring model to simulate the complex hysteresis response of the U-shaped plates used in this study.

The PT strands were modelled using a truss element using a uniaxial material (Ma 2010) consisting of the bilinear response shown in Figure 5-5c. To generate the backbone curve, the initial strain $\epsilon_o = 0.232\%$ and yield strain $\epsilon_y = 0.860\%$ were calculated using the design parameters described earlier. The moduli of elasticity, $E_1 = 54,036$ kN/mm² and $E_2 = 140,964$ kN/mm².

To simulate the rocking base of STRBF, compression-only gap elements are used, as shown in Figure 5-5d. As shown, the gap closes when the column undergoes compression and opens under tension (Moradi and Burton 2018). Other DOFs at the bases of the STRBF and lean-on columns

were modelled as pinned support. Steel diagonal-to-beam/column and beam-to-column connections, plus timber beam-to-column connections, were modelled as pin connections.

A co-rotational geometric transformation was implemented to account for P- Δ effects and large deformations. Gravity loads respective to each column of the exterior frame were applied on the top end of the column at each storey. Gravity loads tributary to the interior timber columns were applied on the lean-on column to reproduce the P- Δ effect due to their gravity loads. The lateral out-of-plane translation of the columns was restrained at each storey level. Pin connections were used at both ends of each timber column in each storey. To generate viscous damping, a classical Rayleigh damping method was utilized with mass- and stiffness-proportional damping factors assuming a critical damping ratio of 2% in the first and second vibration modes as most of damping will be generated in the steel joints (Yousef Bozorgnia & Vitelmo V. Bertero, 2004). A suite of 33 seismic ground motion records representing three seismic hazard sources expected on the west coast of Canada, namely Crustal, subduction In-slab, and subduction interface, were selected and scaled to match, on average, the 2015 NBC design response spectra (Ashrafi and Imanpour 2021). To perform structural analysis, the gravity loads of the frame were first applied using a static analysis procedure followed by a nonlinear response history analysis (NLRHA) by applying an earthquake acceleration at the base of the frame in the horizontal direction.

5.4.2 Seismic response of STRBF

The NLRHA was performed to evaluate the seismic performance of the STRBF and verify the proposed design method by examining key response parameters, including interstorey drift, brace and columns force demands, axial force demands in PT strands, and fuse flexural demands.

Figure 5-6 presents the seismic response of the STRBF under one of the ground motion records, the 2014 Iquique, Chile earthquake. The history of column uplift for the left columns is shown in Figure 5-6a. Referring to Figure 5-6a, the maximum uplift was recorded as 2.8% and almost no residual uplift was observed at the end of the earthquake. This confirms the recentring capability of the STRBF, which can potentially minimize post-quake damage and rehabilitation costs. The overturning moment normalized to the overturning moment of the system at the yielding of the RF, M_{y1} , (Equation 5-21) is given in Figure 5-6b against column uplift. This figure shows the flagged shape behaviour of the system upon achieving an interstorey drift ratio of 1.68%, suggesting that the rocking response incorporated in the SFRS performs as expected in design.

The fuse moment normalized to the yielding moment is shown in Figure 5-6c versus connection rotation. As shown in Figure 5-6c, the rocking fuses (represented by positive bending) and their counter-rocking counterparts (represented by negative bending) behave as expected in design; namely, a stable hysteresis response was observed under positive and negative bending. Minimal yielding of fuses during rocking does not produce significant deformation, whereas residual deformations start to develop when fuses undergo significant yielding, which triggers yielding in the counter-rocking phase. This response confirms the capability of the seismic fuses implemented in the STRBF to dissipate seismic-induced energy. The axial force of the PT strand normalized to the yielding capacity of the strand is shown in Figure 5-6d. Referring to Figure 5-6d, the PT strand remained in the elastic range during the ground motion (the axial force reached approximately $0.75T_y$) as expected in design, thus providing a self-centring capability to the system.

The peak response parameters from NLRHA were computed by taking the maximum of means over the earthquake ensembles of the peak response parameter obtained under each ground motion record as recommended by the Commentary J of the NBC (Structural Commentaries, 2015). The

results obtained from the NLRHA of the STRBF studied here confirm the potential for a robust seismic performance, evidenced by its effective dissipation of seismic energy, ability to maintain structural integrity under major seismic events, and limited residual deformations after large quakes. These characteristics are central to resilient design in earthquake-prone regions, thus underscoring the promising response of the proposed STRBF.

Figure 5-7a shows the inter-storey drift profiles for the STRBF example as obtained from NLRHA. As shown, the peak drift demand reached 2.18, 2.15, 2.16, 2.13 and 2.14% in storeys 1 - 5, respectively, which are slightly below the assumed drift demand in design, 2.5%. The profiles of uplift, as shown in Figure 5-7c, confirm the development of a rigid body motion under lateral loads with negligible differential displacement between storeys, while dynamic instability is prevented through the implantation of PT strands and the counteraction provided by the gravity loads.

Figure 5-7b shows the profiles of normalized peak fuse moments. The positive values refer to the right connections, while the negative refers to the left connections. Referring to Figure 5-7b, some and not all fuses reached their yielding capacity, which signifies that not all fuses are actively engaged in all ground motion records. This observation is consistent with Figure 5-7c, where not all ground motion records surpass the yield uplift ratio of 1.68%. It can be inferred that the fuses are only actively engaged when this yield uplift ratio is exceeded. The dense area around the 100% mark on the graph in Figure 5-7b represents scenarios where the fuses have reached their capacity, creating a yielding plateau. This behaviour aligns with the design and further confirms the role of the fuses in limiting the overall deformation demands on the structure while efficiently dissipating seismic energy. Figure 5-7d presents the profiles of normalized peak PT strand axial forces. The forces always remained below the strand yielding limit, which indicates that PT strands can

reposition the structure after a seismic event, thereby minimizing permanent deformation and potential damage to structural and non-structural components.

The peak value of force demands in the prototype STRBF is presented in Figure 5-8. Figure 5-8a shows the profiles of peak storey shear normalized by design storey shear $V_{st-Design}$. The peak storey shear aligns well with the predicted values for the first three storeys. However, it is underestimated by approximately 20% in the top two storeys, which could be attributed to higher mode effects (Wiebe et al., 2012). The profiles of normalized peak brace axial forces are depicted in Figure 5-8b, where positive values represent tensile forces and negative values indicate compressive forces. This figure reveals that all braces remained in the elastic region when undergoing tensile forces and remained well below their buckling loads under compression except in three cases where the first-storey brace buckled. The peak normalized compressive axial forces in the braces of storeys 1 – 5 reached 75, 55, 42, 60 and 42%, respectively. The peak normalized brace axial forces in tension also were 32, 22, 17, 24 and 1% in storeys 1 – 5. This observation reaffirms the effectiveness of the rocking system implemented in the STRBF.

Figure 5-8c presents the axial force-moment interaction ratios for the steel columns. The peak values of the interaction ratios were below unity in all storeys, reaching 35, 38, 32, 26 and 14% for Storeys 1 – 5, respectively. Figure 5-8d presents the axial force-moment interaction ratios for the steel beams. Limited inelastic behaviour was observed in the first-storey beams in a few instances, evidenced in only two records. Nevertheless, peak interaction ratios were recorded as 65, 40, 31, 14 and 37% for Storeys 1 – 5, respectively. Overall, the observed peak responses in capacity-protected elements confirm that they remain essentially elastic under design-level seismic events, which was targeted in the proposed design method.

5.5 Limitations

This study proposed a new hybrid SFRS and validated its seismic performance. The authors, however, recognize certain limitations, which also outline potential avenues for future research. First, the analysis conducted here does not fully consider three-dimensional effects. Second, the prototype building selected aimed to match the fuse connections for which test data is available and may not fully represent the diversity in real-world building designs. Hence, future studies considering various potential building layouts and heights are needed to extrapolate the findings of this study. Moreover, future research should investigate the collapse performance of the proposed hybrid steel-timber rocking braced frame systems, e.g., using the FEMA P695 methodology. Lastly, the proposed system should be studied experimentally to verify its performance and refine the proposed design method.

5.6 Conclusions

This paper introduced an innovative low-damage hybrid steel-timber rocking braced frame (STRBF) with self-centring capability. This system aims to minimize structural damage and associated repair costs after a seismic event, thus enhancing structural resilience. Proposed system combines a timber frame to mainly carry gravity loads and a steel concentrically braced frame acting as a lateral load-resisting system. A design method was proposed in the framework of the Canadian design standards, including sizing of ductile fuses, post-tensioning strands and steel members. The proposed method was demonstrated for a five-storey prototype structure. The seismic performance of the proposed system, along with the efficiency of the proposed design guidelines, were examined through a set of dynamic analyses. The key findings of this study are summarized below:

- The STRBF system effectively resists seismic-induced demands through the rocking response of the columns, which create rigid body motion under the lateral seismic load.
- The prototype STRBF experienced an average peak inter-storey drift of 2.2%, which meets the code-specified drift limit of 2.5%.
- The rocking behaviour imposes distinct rotational demands on the fuses incorporated in the beam-to-column connections. The fuses acting on the rocking side experience twice the rotational demand as those on the counter-rocking side. The rocking fuses reach their yielding moment at an uplift of 1.68%, while the counter-rocking ones remain elastic.
- The self-centring capability of the system is provided by vertical PT strands that are designed to remain elastic under 70% of their yielding force.
- The storey shear forces obtained from numerical analyses are consistent with those obtained from the Direct Displacement-Based Design method used to develop the design method. Storey shears predicted by the numerical model at the top two storeys are 20% higher than design values due to higher mode effects.
- Capacity-protected elements, including beams, columns, and braces, remained elastic under design-level hazards. The normalized peak compressive axial force of the brace reached 75% in the first storey, and the peak axial force-moment interaction ratio of the steel columns and beams reached 38% and 65% in the second and first storeys, respectively.

Notation

The following symbols are used in this chapter:

PT: Post-Tensioned

STRBF: Steel-Timber Rocking Braced Frame

SFRS: Seismic Force Resisting System

U-shaped fuses: U-shaped steel fuses

CBF: Concentrically Braced Frame

CRF: Counter Rocking Fuses

RF: Rocking Fuses

NBC: National Building Code

θ : Uplift ratio

ϑ : Fuse rotation

M_{om} : Overturning moment

M_{bm} : Balancing moment

F_{PT} : Force in Post-Tensioned strands

M_{RF} : Moment in Rocking Fuses

M_{CRF} : Moment in Counter Rocking Fuses

P_{RF} : Vertical reaction force

η_{max} : Maximum initial pre-stress level in PT strands

η_0 : Initial pre-stress level in PT strands

N : Number of PT strands

θ_m : Yield uplift ratio of PT strands

ED : Energy Dissipation capacity

R_d : Ductility modification factor

R_o : Overstrength modification factor

T_a : Design fundamental period

S_a : Design spectral acceleration

I_E : Importance factor

M_ν : Factor accounting for higher mode effects

SC : Self-Centring ratio

μ : Ductility factor

t : Thickness of U-shaped connection plates

H : Total height of the frame

F_y : Yield strength

F_u : Ultimate strength

D_{PT} : Horizontal distance between PT bars and the point of overturning computation

L_{PT} : Length of PT bars

$F_{PT,FY}$: Pre-tensioning force in PT bars when fuses yield

ϑ_y : Yield rotation of the fuses

ϑ_u : Ultimate rotation of the fuses

$M_{F,y}$: Yielding moment of the U-shaped connection

$M_{F,u}$: Ultimate moment of the U-shaped connection

K_{PT} : Stiffness of PT strands

K_{fuse2} : Post-yield stiffness of the fuse

θ_{y1} : Uplift ratio at yielding of Rocking Fuses

θ_{y2} : Uplift ratio at yielding of Counter Rocking Fuses

θ_e : Maximum uplift ratio

F_{PTE} : Force in PT strands at maximum uplift ratio

$M_{RF,e}$: Moment in Rocking Fuses at maximum uplift ratio

$M_{CRF,e}$: Moment in Counter Rocking Fuses at maximum uplift ratio

α : Equivalent single load height ratio

V_{max} : Maximum expected base shear

F_{roof} : Peak inertia force at the roof

F_{floor} : Peak inertia force at each floor

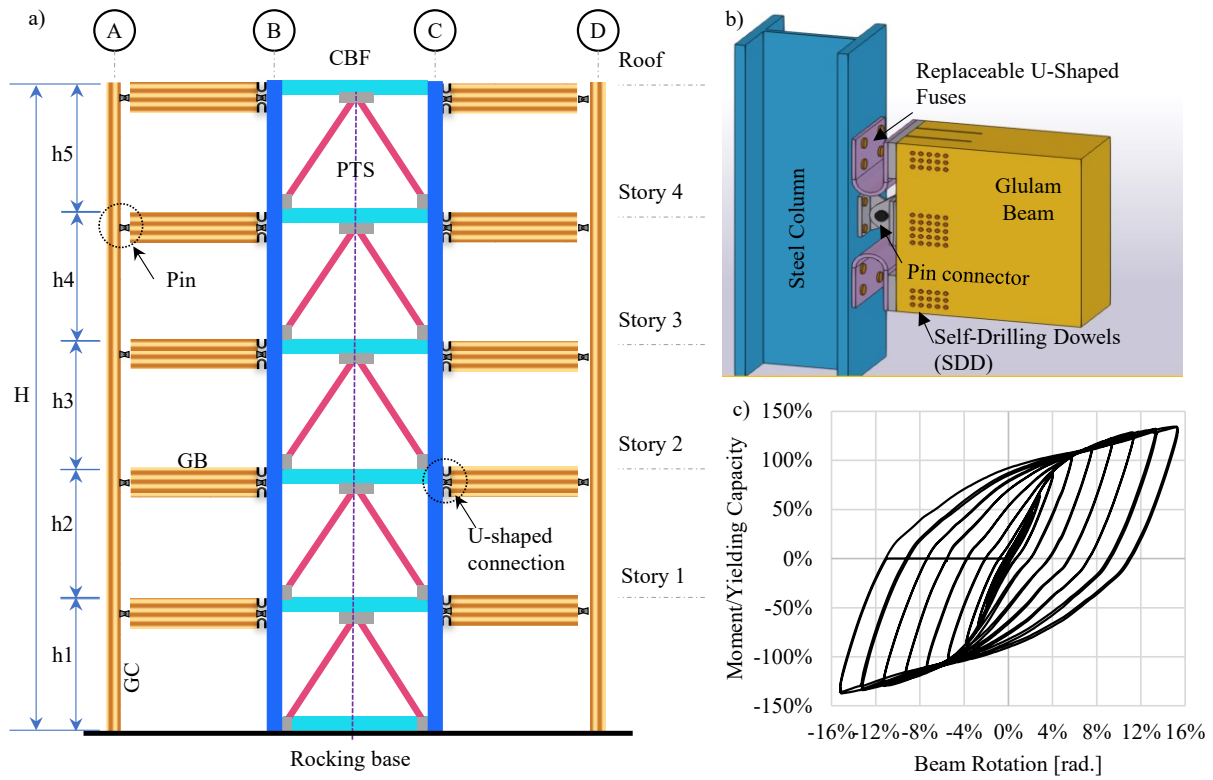


Figure 5-1: a) Proposed hybrid steel-timber frame building system; b) U-shaped connection; and c) Moment-rotation response of the U-shaped connection under cyclic loading.

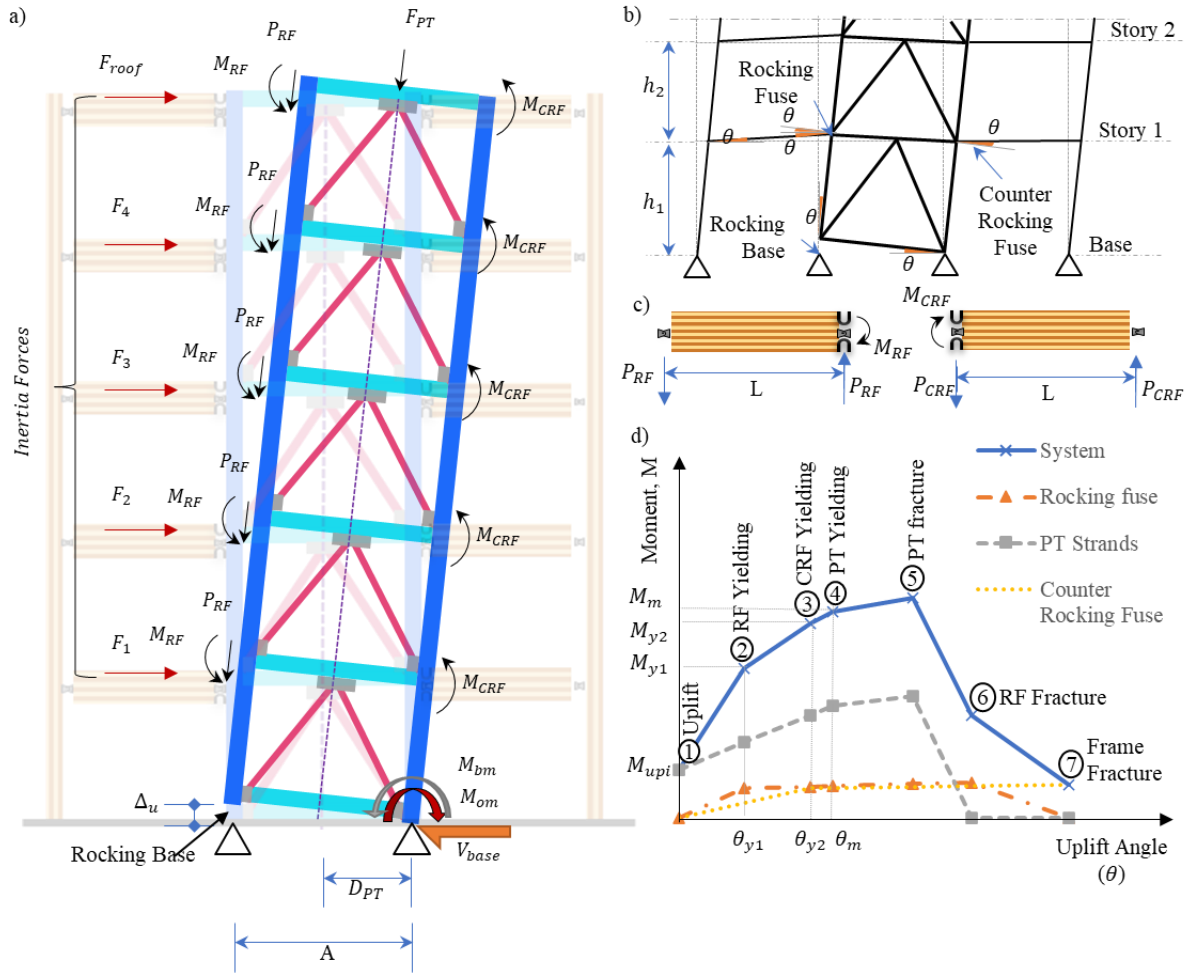


Figure 5-2: Lateral response of hybrid steel-timber rocking braced frame: a) For equilibrium of the STRBF upon rocking; b) Column uplift θ and fuse connection rotations upon rocking; c) Free body diagram of glulam beam with rocking and counter rocking joints; d) Moment versus uplift angle of the STRBF.

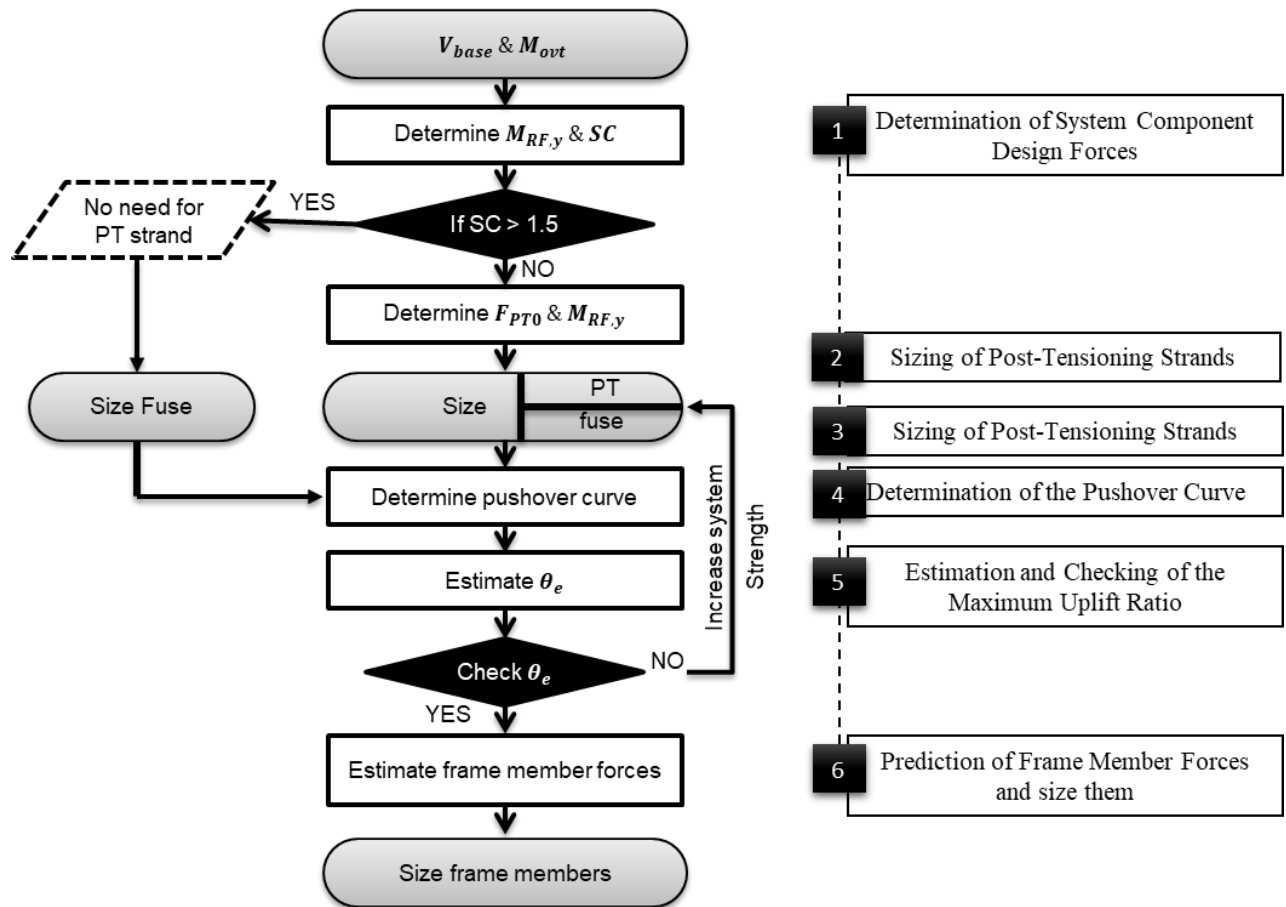


Figure 5-3. Design steps for the STRBF.

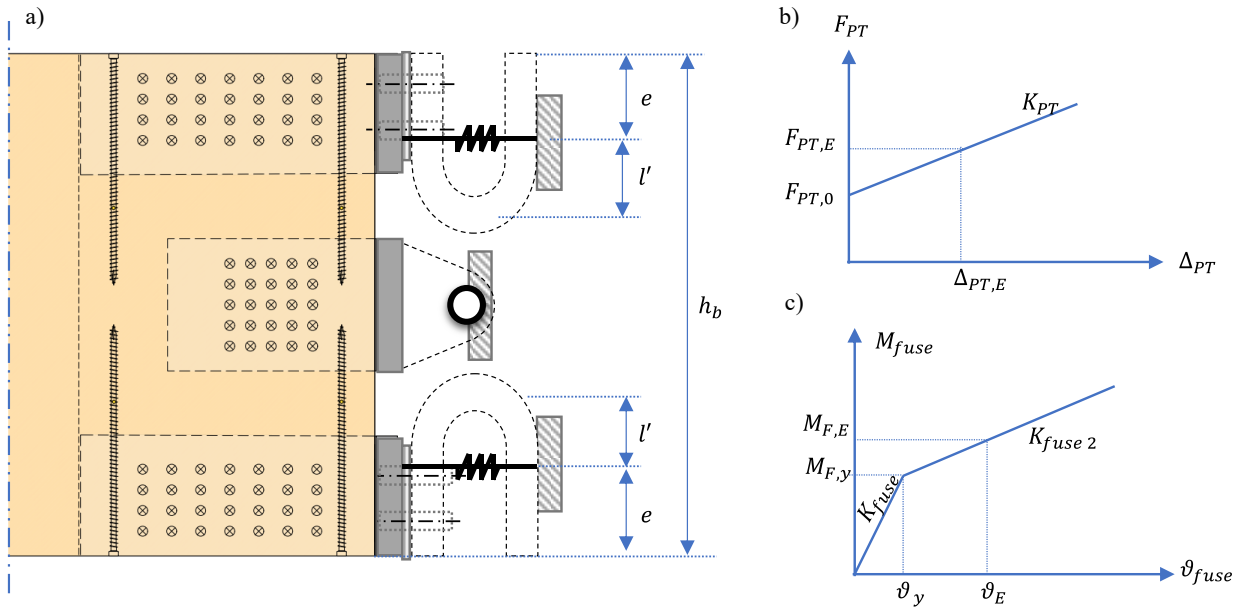


Figure 5-4: a) U-shaped fuse connection design parameters; b) PT strands inelastic behaviour; c)

U-shaped connection inelastic behaviour.

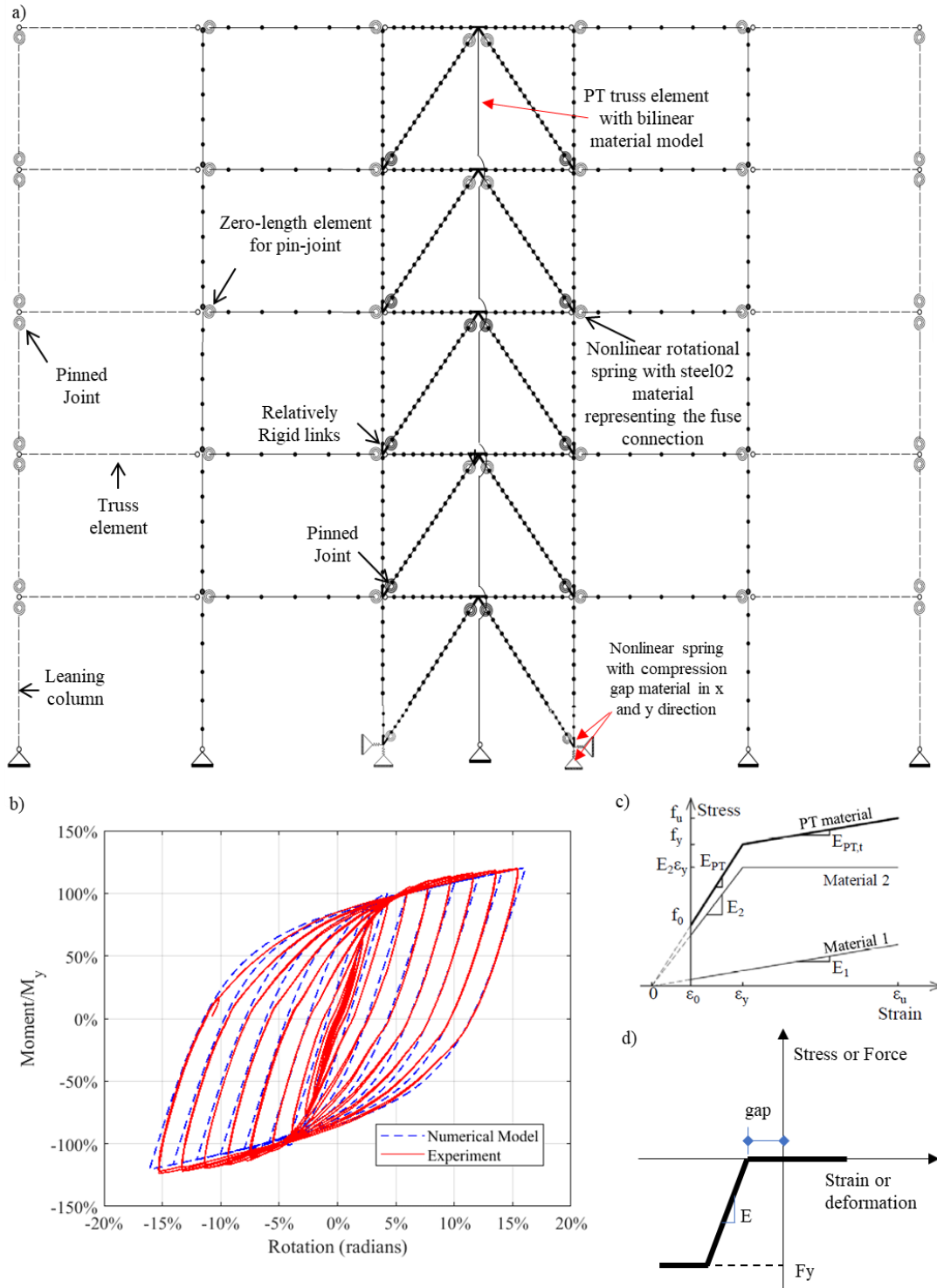


Figure 5-5: a) STRBF fibre-based numerical model; b) U-shaped fuse moment – rotation response: numerical prediction vs. experimental data; c) PT truss element; d) Compression gap element.

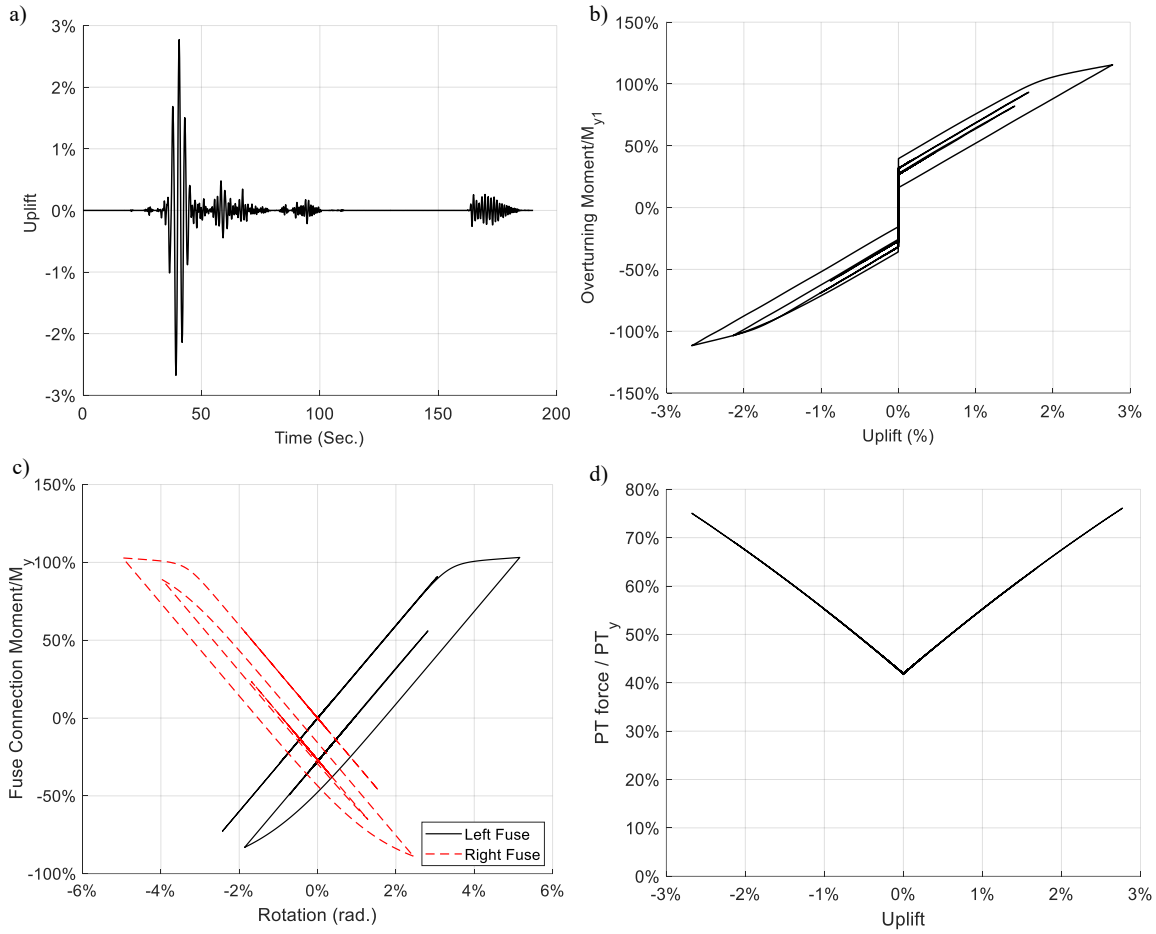


Figure 5-6: Seismic response of the prototype STRBF under 2014 Iquique, Chile earthquake record: a) History of frame uplift; b) Overturning moment vs. uplift; c) Fuse connection moment vs. connection rotation; d) PT strand force vs. uplift.

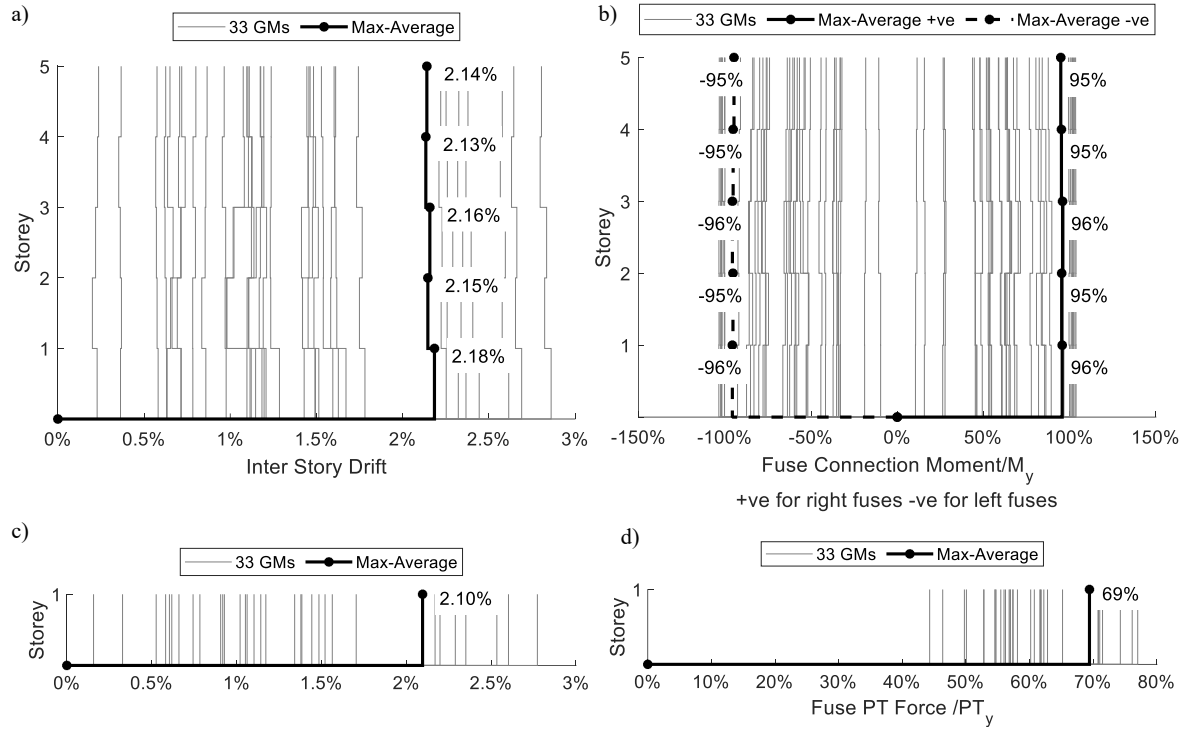


Figure 5-7: Profile of peak response parameters from NLRHA: a) Interstorey drift; b) Fuse connection bending moment; c) Uplift; d) PT strand axial force.

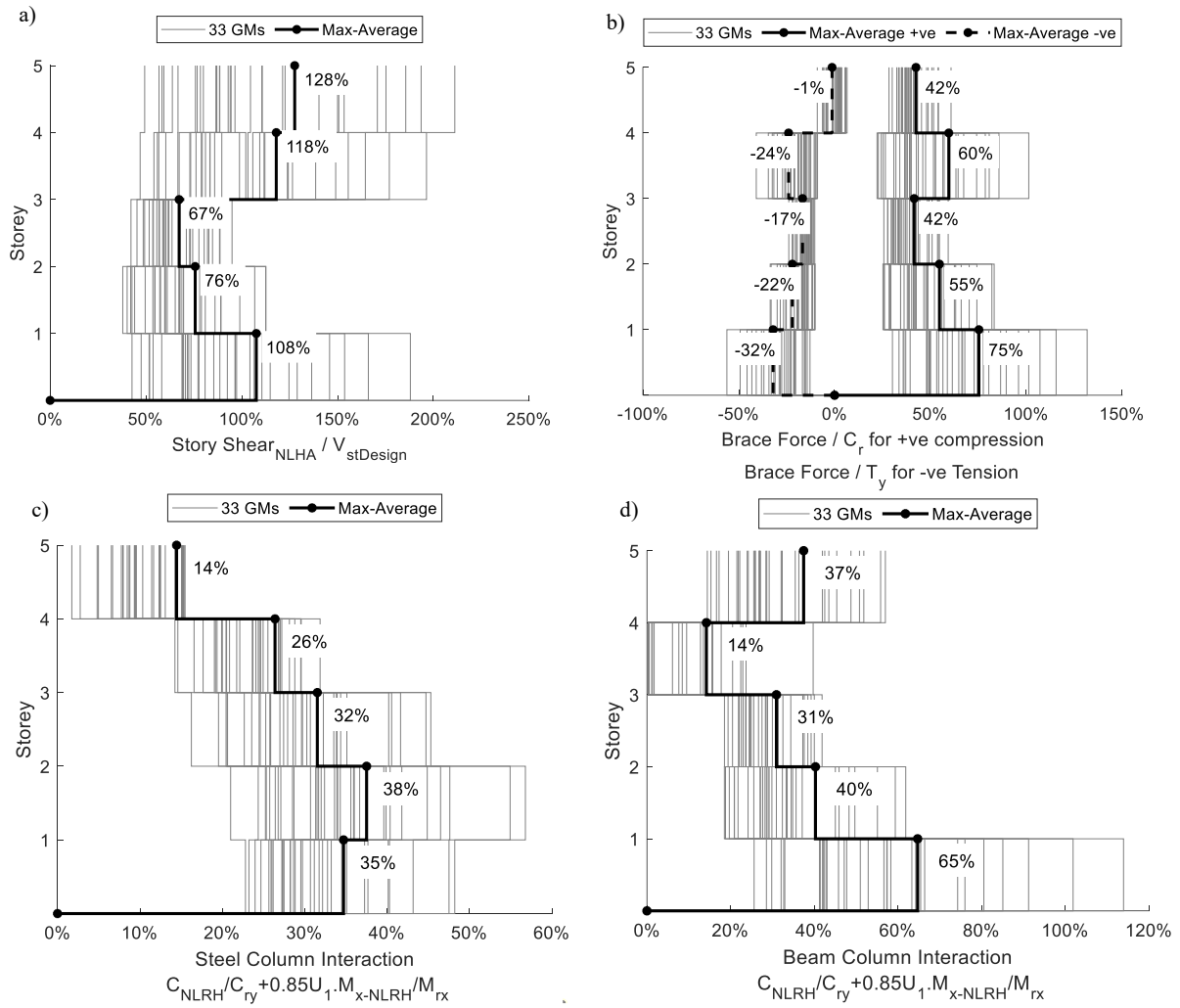


Figure 5-8 Profile of peak response parameters from NLRH analyses: a) Storey shear; b) Steel-brace axial forces; c) Steel-column forces; d) Steel-beam forces.

6. Conclusions and recommendations

6.1 Conclusions

The 1994 Northridge and 2010-2011 Christchurch earthquakes revealed conventional structures' vulnerabilities and led to the interest in resilient structures. These structures should prioritize life safety and enable swift post-earthquake recovery while minimizing repair and retrofitting costs. Hybrid steel-timber structures have emerged as a promising solution for resilient structures. These hybrid structures offer a compelling approach to improving overall structural performance and enhancing construction efficiency by harnessing the ductility of steel in combination with the lightness and sustainability of timber.

The thesis presented a practical guideline to design a resilient hybrid steel-timber rocking braced frame (STRBF) and developed novel connection and self-centring systems. This novel connection system featuring U-shaped steel seismic fuses was designed to connect a gravity load-resisting timber frame with a steel concentrically braced frame acting as the lateral load-resisting system with self-centring capability. The STRBF has been studied through three interconnected research components as follows:

- The first component investigated the novel U-shaped steel seismic fuse, highlighting its potential for diverse applications with notable strength, stiffness, ductility, and energy dissipation capacity.
- The second component integrated the proposed U-shaped steel plate (USP) into an innovative hybrid timber beam-to-steel column connection system. This connection system

demonstrated enhanced cyclic load resistance and stable load-displacement cycles and facilitated rapid post-earthquake recovery.

- The third component proposed an innovative, low-damage STRBF based on the results of the earlier components. The proposed design methodology was validated through extensive numerical analyses, showcasing the system's seismic performance and its capability to exhibit minimal residual deformations following an earthquake event.

The research findings advanced the understanding of the seismic resilience of hybrid steel-timber structures. The U-shaped steel seismic fuse with scissor bending mechanism demonstrated an effective dissipation of the seismic loads and enhanced the structural performance of the system. The novel hybrid steel-timber rocking braced frame demonstrated effective resistance to seismic-induced demands, displaying self-centring capabilities and remaining within code-specified drift limits, highlighting its resilience and capacity to recover after seismic events. The key findings from this thesis are as follows:

- The U-shaped steel seismic fuse, employing a scissor bending mechanism, demonstrated notable strength, stiffness, ductility, and energy dissipation capacity, making it a viable option for various applications in hybrid steel-timber structures. The USP fuses yielded, on average at 5% scissor displacement (D) of the inter diameter of the USP while sustaining a deformation demand of $20\%D$ without unsatisfactory limit states, confirming their potential to safely dissipate seismic loads.
- The innovative hybrid timber beam-to-steel column connection system, incorporating the proposed USP, enhanced cyclic load resistance and stable load-displacement cycles. It also facilitated rapid post-earthquake recovery and enhanced the overall seismic resilience of

the structure. Increasing the fuse thickness raised the stiffness and yielding moment of the connection, ranging from 26-78 kN.m.

- The development and validation of replaceable fuses provided flexible and effective structural upgrade options post-earthquake, improving the repairability and resilience of hybrid steel-timber structures. Retrofitted beams with replaceable fuses demonstrated the same level of hysteretic behaviour, stiffness, and yielding.
- Practical applications of these research findings were evident in the design of a five-storey prototype building, where a self-centring, chevron-type steel frame served as an effective lateral load-resisting system. The seismic design standards have been significantly influenced, and the broader use of timber in structural design has been fostered, promoting the development of resilient hybrid steel-timber structures.
- The novel hybrid steel-timber rocking braced frame, designed with a self-centring capability, effectively resisted seismic-induced demands, minimized residual deformations post-earthquake. It also remained elastic under design-level hazards and highlighted its superior seismic performance and resilience. The prototype STRBF experienced an average peak inter-storey drift of 2.2%, meeting the code-specified drift limit of 2.5%.

By incorporating the research findings in seismic design of mid-rise buildings, structural engineers can enhance buildings' safety, resiliency, and sustainability in locations that are prone to strong seismic activities. Developing innovative force-resisting systems and replaceable fuses can significantly reduce earthquake-induced damage and minimize post-earthquake repair costs, thus promoting more resilient and safer structures in seismic regions.

6.2 Recommendations for future work

A more comprehensive set of guidelines for enhancing the seismic resilience of hybrid steel-timber structures could be as follows:

- Validation and field testing of USP fuses: To ensure the practical applicability and reliability, further validation through extensive field testing is essential. Collaborating with industry partners and conducting full-scale tests on full-scale structures will provide valuable data on the performance of these fuses under actual seismic loading conditions.
- Material and residual stress distribution investigation: Conducting in-depth research on the material properties and residual stress distribution in USP fuses is recommended. Understanding the influence of material strain hardening and residual stresses on the cyclic behaviour of the fuses will enable engineers to optimize the design and enhance the overall seismic performance of hybrid steel-timber structures.
- Optimization of USP fuse dimensions: Further research and numerical simulations are required to optimize the dimensions of USP fuses for different applications. Investigating the effect of varying thicknesses and configurations will aid in designing connection systems tailored to specific building requirements and seismic hazards.
- Innovative retrofitting strategies: Building upon the successful implementation of USP fuses, researchers and engineers should explore innovative retrofitting strategies for existing structures. Identifying critical connections vulnerable to seismic forces and retrofitting them with the proposed fuses can significantly improve the seismic resilience of older hybrid steel-timber buildings.

- Testing and design guidelines for hybrid timber beam-to-steel column connections: The hybrid timber beam-to-steel column connection system, featuring USP fuses, demonstrated promising results. However, further extensive parametric studies and finite element modelling are needed to ensure its widespread adoption and reliable implementation in diverse projects. Developing comprehensive testing protocols and design guidelines based on these studies will enable engineers to confidently incorporate these connections into new construction and retrofit projects, enhancing the overall seismic resilience of hybrid steel-timber structures.
- Further investigation is required to address the splitting cracks observed in closed-fuse connections, particularly considering their relatively higher stiffness and ductility. The splitting cracks were found to occur around the pin connector area in the glulam at 4% radians and propagated, leading to global failure at the end of the test. Identifying potential ways to mitigate these splitting cracks is essential to enhance the overall performance and resilience of the closed-fuse connection system in hybrid timber structures.
- Future studies should consider various potential building layouts and heights to extrapolate the findings of this study, as the prototype building selected may not fully represent the diversity in real-world building designs.
- A simplified force-based design method should be developed for the proposed rocking system in the framework of the National Building Code of Canada.
- Further investigations should examine the collapse performance of the proposed hybrid steel-timber rocking braced frame system, using FEMA P695 (FEMA, 2009) method and determine the ductility- and overstrength-related force modification factors.

- Further investigations should assess the behaviour of the proposed under wind loading. These studies should verify that the system remains elastic without initiation of the rocking mechanism.
- Research on combined connection systems: Combining USP fuses with other innovative connection systems can lead to even more resilient hybrid steel-timber structures. Research efforts should be directed toward investigating the synergistic effects of different connection technologies to enhance overall seismic performance.
- Public awareness and education: Increasing public awareness and educating stakeholders about the benefits and importance of seismic resilience in hybrid steel-timber structures is crucial. Engaging with communities, policymakers, and building owners will foster support for adopting these technologies and investing in resilient construction practices.
- Long-term monitoring and performance assessment: Implementing long-term monitoring and performance assessment of hybrid steel-timber buildings will provide valuable data on their behaviour over time. Continuous monitoring of structural responses under actual seismic events will enable engineers to refine designs and make informed decisions for future projects.

By incorporating these recommendations into future research, design, and construction practices, the seismic resilience of hybrid steel-timber structures can be significantly enhanced. Embracing innovation, collaboration, and a proactive approach to seismic design will contribute to developing sustainable and resilient building solutions for seismic-prone regions.

Bibliography

- Aghlara, R., & Tahir, M. M. (2018). A passive metallic damper with replaceable steel bar components for earthquake protection of structures. *Engineering Structures*, *159*(December 2017), 185–197. <https://doi.org/10.1016/j.engstruct.2017.12.049>
- AISC. (2016). Seismic Provisions for Structural Steel Buildings, ANSI/AISC 341-16. In *American Institute of Steel Construction*. <https://doi.org/10.1201/b11248-8>
- Andreolli, M., Piazza, M., Tomasi, R., & Zandonini, R. (2011). Ductile moment-resistant steel-timber connections. *Proceedings of the Institution of Civil Engineers: Structures and Buildings*, *164*(2), 65–78. <https://doi.org/10.1680/stbu.9.00098>
- ASTM. (2013). *A1085-13: Standard Specification for Cold-Formed Welded Carbon Steel Hollow Structural Sections (HSS): Vol. i* (pp. 1–5). https://doi.org/10.1520/A1085_A1085M-15
- ASTM. (2015). *ASTM A992 / A992M-11(2015), Standard Specification for Structural Steel Shapes*. ASTM International.
- ASTM International. (2020). *ASTM A490 - 14(2020)*. ASTM International. <https://www.astm.org/Standards/A490.htm>
- Azuhata, T., Ishihara, T., Midorikawa, M., & Wada, A. (2006). Seismic response reduction of steel frames with multi-spans by applying rocking structural system. *Proc of 2006 STESSA*.
- Bagheri, S., Barghian, M., Saieri, F., & Farzinfar, A. (2015). U-shaped metallic-yielding damper in building structures: Seismic behavior and comparison with a friction damper. *Structures*,

3, 163–171. <https://doi.org/10.1016/j.istruc.2015.04.003>

Baird, A., Smith, T., Palermo, A., & Pampanin, S. (2014). Experimental and numerical Study of U-shape Flexural Plate (UFP) dissipators. *NZSEE Conference, January 2021*, 1–9.

http://db.nzsee.org.nz/2014/poster/2_Baird.pdf

Bruneau, M., Uang, C.-M., & Sabelli, S. E. R. (2011). *Ductile design of steel structures*.

McGraw Hill Professional.

Bryant, A. H., Gibson, J. A., Mitchell, T. N., & Thurston, S. J. (1981). Nailed Moment Joints in

Timber Structures. *Bulletin of the New Zealand National Society for Earthquake*

Engineering, 14(4), 223–232. <https://doi.org/10.5459/bnzsee.14.4.223-232>

Buchanan, A., Deam, B., Fragiaco, M., Pampanin, S., & Palermo, A. (2008). Multi-Storey Prestressed Timber Buildings in New Zealand. *Structural Engineering International*, 18(2),

166–173. <https://doi.org/10.2749/101686608784218635>

Buchanan, A. H., & Fairweather, R. H. (1993). Seismic design of glulam structures. *Bulletin of the New Zealand National Society for Earthquake Engineering*, 26(4), 415–436.

<https://doi.org/10.5459/bnzsee.26.4.415-436>

Canadian Standards Association, [CSA]. (2014a). *CAN/CSA O86-14 Wood Design Manual*.

McGraw-Hill Education. <https://doi.org/10.1036/1097-8542.757406>

Canadian Standards Association, [CSA]. (2014b). *CAN/CSA S16-14 Limit States Design of Steel Structures*.

Cao, J., Xiong, H., & Cui, Y. (2022). Seismic performance analysis of timber frames based on a

- calibrated simplified model. *Journal of Building Engineering*, 46(November 2021), 103701.
<https://doi.org/10.1016/j.jobe.2021.103701>
- Castro e Sousa, A. de, Hartloper, A. R., & Lignos, D. G. (2021). Cyclic Metal Plasticity Model Parameters with Limited Information: Constrained Optimization Approach. *Journal of Engineering Mechanics*, 147(7). [https://doi.org/10.1061/\(asce\)em.1943-7889.0001922](https://doi.org/10.1061/(asce)em.1943-7889.0001922)
- CEN. (2001). *Standards Europe. EN 12512:2001 Timber structures - Test methods*.
- Chan, R. W. K., Albermani, F., & Kitipornchai, S. (2013). Experimental study of perforated yielding shear panel device for passive energy dissipation. *Journal of Constructional Steel Research*, 91, 14–25. <https://doi.org/10.1016/j.jcsr.2013.08.013>
- Chancellor, N. B., Eatherton, M. R., Roke, D. A., & Akbas, T. (2014). Self-centering seismic lateral force resisting systems: High performance structures for the city of tomorrow. *Buildings*, 4(3), 520–548. <https://doi.org/10.3390/buildings4030520>
- Clough, R. W., & Huckelbridge, A. A. (1977). Preliminary experimental study of seismic uplift of a steel frame. *Earthquake Engineering Research Center*, Report No. UCB/EERC-77/22.
- correlatedsolutions. (2018). *correlatedsolutions*. <https://www.correlatedsolutions.com/>
- Council, A. T. (1996). *Seismic Evaluation and Retrofit of Concrete Buildings*.
<https://doi.org/SSC 96-01>
- CSA. (2019a). CAN/CSA-086-01. A National Standard of Canada. Engineering Design in Wood. In *Standard* (Vol. 1, Issue 1).
- CSA. (2019b). *CSA S16-19: Design of steel structures*.

<https://www.csagroup.org/store/product/CSA S16:19/>

CSA, C., & Association, S. (2013). *General requirements for rolled or welded structural quality steel / Structural quality steel, in CAN/CSA G40.20-13/G40.21-1*. CSA Group.

<https://www.csagroup.org/store/product/2702047/>

Cui, Y., Shu, Z., Zhou, R., Li, Z., Chen, F., & Ma, Z. (2020). Self-centering steel–timber hybrid shear wall with slip friction dampers: Theoretical analysis and experimental investigation. *The Structural Design of Tall and Special Buildings*, e1789.

Daneshvar, H., Niederwestberg, J., Dickof, C., Jackson, R., & Hei Chui, Y. (2022). Perforated steel structural fuses in mass timber lateral load resisting systems. *Engineering Structures*, 257(March), 114097. <https://doi.org/10.1016/j.engstruct.2022.114097>

de Castro e Sousa, A., Suzuki, Y., & Lignos, D. (2020). Consistency in Solving the Inverse Problem of the Voce-Chaboche Constitutive Model for Plastic Straining. *Journal of Engineering Mechanics*, 146(9), 1–16. [https://doi.org/10.1061/\(asce\)em.1943-7889.0001839](https://doi.org/10.1061/(asce)em.1943-7889.0001839)

Deng, K., Pan, P., & Wang, C. (2013). Development of crawler steel damper for bridges. *Journal of Constructional Steel Research*, 85, 140–150. <https://doi.org/10.1016/j.jcsr.2013.03.009>

Dong, W., Li, M., He, M., & Li, Z. (2021a). Experimental Testing and Analytical Modeling of Glulam Moment Connections with Self-Drilling Dowels. *Journal of Structural Engineering*, 147(5), 04021047. [https://doi.org/10.1061/\(asce\)st.1943-541x.0002977](https://doi.org/10.1061/(asce)st.1943-541x.0002977)

Dong, W., Li, M., He, M., & Li, Z. (2021b). Experimental Testing and Analytical Modeling of

Glulam Moment Connections with Self-Drilling Dowels. *Journal of Structural Engineering*, 147(5), 1–18. [https://doi.org/10.1061/\(asce\)st.1943-541x.0002977](https://doi.org/10.1061/(asce)st.1943-541x.0002977)

Dongbin, Z., Xin, N., Peng, P., Mengzi, W., Kailai, D., & Yabin, C. (2016). Experimental study and finite element analysis of a buckling-restrained brace consisting of three steel tubes with slotted holes in the middle tube. *Journal of Constructional Steel Research*, 124, 1–11. <https://doi.org/10.1016/j.jcsr.2016.05.003>

Dyanati, M., Huang, Q., & Roke, D. (2015). Seismic demand models and performance evaluation of self-centering and conventional concentrically braced frames. *Engineering Structures*, 84, 368–381.

Eatherton, M. R. (2010). *Large-scale cyclic and hybrid simulation testing and development of a controlled-rocking steel building system with replaceable fuses*. University of Illinois at Urbana-Champaign.

Eatherton, M. R., & Hajjar, J. F. (2011). Residual drifts of self-centering systems including effects of ambient building resistance. *Earthquake Spectra*, 27(3), 719–744. <https://doi.org/10.1193/1.3605318>

Eatherton, M. R., Ma, X., Krawinkler, H., Deierlein, G. G., & Hajjar, J. F. (2014). Quasi-static cyclic behavior of controlled rocking steel frames. *Journal of Structural Engineering*, 140(11), 4014083.

Eatherton, M. R., Ma, X., Krawinkler, H., Mar, D., Billington, S., Hajjar, J. F., & Deierlein, G. G. (2014). Design concepts for controlled rocking of self-centering steel-braced frames. *Journal of Structural Engineering*, 140(11), 4014082.

- FEMA;, & ATC. (2007). *461/Interim Testing Protocols for Determining the Seismic Performance Characteristics of Structural and Nonstructural Components* (Issue June). Applied Technology Council.
- FEMA. (2009). *Quantification of Building Seismic Performance Factors, FEMA P-695*.
- Filiatrault, A., Restrepo, J., & Christopoulos, C. (2004). Development of self-centering earthquake resisting systems. *13th World Conference on Earthquake Engineering*, 1–6.
- Filippou, F. C., Popov, E. P., & Bertero, V. V. (1983). *Effects of bond deterioration on hysteretic behavior of reinforced concrete joints*. Earthquake Engineering Research Center.
- Foliente, G. C. (2000). History of Timber Construction. In *Wood Structures: A Global Forum on the Treatment, Conservation, and Repair of Cultural Heritage* (pp. 3–22).
<https://doi.org/10.1520/STP13370S>
- Gavric, I., Fragiacomio, M., & Ceccotti, A. (2015). Cyclic Behavior of CLT Wall Systems: Experimental Tests and Analytical Prediction Models. *Journal of Structural Engineering*, *141*(11), 4015034. [https://doi.org/10.1061/\(ASCE\)ST.1943-541X.0001246](https://doi.org/10.1061/(ASCE)ST.1943-541X.0001246)
- Gilbert, C. F., & Erochko, J. (2016). Adaptation of advanced high R-factor bracing systems into heavy timber frames. *WCTE 2016 - World Conference on Timber Engineering, December*.
- Gilbert, C. F., & Erochko, J. (2019). Development and testing of hybrid timber-steel braced frames. *Engineering Structures*, *198*, 109495.
<https://doi.org/10.1016/j.engstruct.2019.109495>
- Gohlich, R., Erochko, J., & Woods, J. E. (2018). Experimental testing and numerical modelling

- of a heavy timber moment-resisting frame with ductile steel links. *Earthquake Engineering and Structural Dynamics*, 47(6), 1460–1477. <https://doi.org/10.1002/eqe.3025>
- Goldsworthy, H. (2012). Lessons from the 22 February 2011 Christchurch earthquake. *Australian Journal of Structural Engineering*, 13(2). <https://doi.org/10.7158/s11-136.2012.13.2>
- Gregory L. Fenves, F. M. S. M. M. H. S. (2009). *OpenSees command manual*. Pacific Earthquake Engineering Research Center.
- Hashemi, A., Bagheri, H., Yousef-Beik, S. M. M., Darani, F. M., Valadbeigi, A., Zarnani, P., & Quenneville, P. (2020). Enhanced Seismic Performance of Timber Structures Using Resilient Connections: Full-Scale Testing and Design Procedure. *Journal of Structural Engineering*, 146(9), 1–15. [https://doi.org/10.1061/\(asce\)st.1943-541x.0002749](https://doi.org/10.1061/(asce)st.1943-541x.0002749)
- Hashemi, A., Masoudnia, R., & Quenneville, P. (2016). Seismic performance of hybrid self-centring steel-timber rocking core walls with slip friction connections. *Journal of Constructional Steel Research*, 126, 201–213. <https://doi.org/10.1016/j.jcsr.2016.07.022>
- He, M. J., & Liu, H. F. (2015). Comparison of glulam post-to-beam connections reinforced by two different dowel-type fasteners. *Construction and Building Materials*, 99, 99–108. <https://doi.org/10.1016/j.conbuildmat.2015.09.005>
- He, M., Li, Z., Lam, F., Ma, R., & Ma, Z. (2014). Experimental Investigation on Lateral Performance of Timber-Steel Hybrid Shear Wall Systems. *Journal of Structural Engineering*, 140(6), 1–12. [https://doi.org/10.1061/\(asce\)st.1943-541x.0000855](https://doi.org/10.1061/(asce)st.1943-541x.0000855)

- He, M., Zhang, J., & Li, Z. (2017). Influence of cracks on the mechanical performance of dowel type glulam bolted joints. *Construction and Building Materials*, 153, 445–458.
<https://doi.org/10.1016/j.conbuildmat.2017.07.095>
- Henriques, J., Calado, L., Castiglioni, C. A., & Degée, H. (2019a). U-shaped steel plate dissipative connection for concentrically braced frames. *SDSS 2019 - International Colloquium on Stability and Ductility of Steel Structures, Figure 1*, 476–482.
- Henriques, J., Calado, L., Castiglioni, C. A., & Degée, H. (2019b). U-shaped steel plate dissipative connection for concentrically braced frames. In *Stability and Ductility of Steel Structures - Proceedings of the International Colloquia on Stability and Ductility of Steel Structures, 2019* (Vol. 17, Issue 11). Springer Netherlands. <https://doi.org/10.1007/s10518-019-00689-y>
- Housner, G. W. (1963). The Behavior of Inverted Pendulum Structure During Earthquakes. *Building of the Seismology Society of America*, 53(2), 403–417.
- Hwang, S.-H., & Lignos, D. G. (2017). Effect of Modeling Assumptions on the Earthquake-Induced Losses and Collapse Risk of Steel-Frame Buildings with Special Concentrically Braced Frames. *Journal of Structural Engineering*, 143(9), 1–16.
[https://doi.org/10.1061/\(asce\)st.1943-541x.0001851](https://doi.org/10.1061/(asce)st.1943-541x.0001851)
- Iqbal, a, Pampanin, S., & Buchanan, a. (2010). Seismic Performance of Prestressed Timber Beam-Column Sub-Assemblies. *New Zealand Society for Earthquake Engineering*, 27.
- Iqbal, A. (2016). Prestressed timber structures for multi-storied buildings: From theory to practice. *Proceedings, Annual Conference - Canadian Society for Civil Engineering*, 4,

2903–2913.

Iqbal, A., Pampanin, S., & Buchanan, A. (2007). Improved Seismic Performance of LVL Post-tensioned Walls Coupled with UFP devices. *Program, Xxx*.

Iqbal, A., Pampanin, S., Palermo, A., & Buchanan, A. H. (2015). Performance and design of LVL walls coupled with UFP dissipaters. *Journal of Earthquake Engineering, 19*(3), 383–409. <https://doi.org/10.1080/13632469.2014.987406>

Jensen, H., Valdebenito, M., Sepúlveda, J., & Becerra, L. (2012). Discrete variable structural optimization of systems under stochastic earthquake excitation. In *Structural seismic design optimization and earthquake engineering: formulations and applications* (pp. 51–75). IGI Global.

Jorissen, A., & Fragiacomio, M. (2011). General notes on ductility in timber structures. *Engineering Structures, 33*(11), 2987–2997. <https://doi.org/10.1016/j.engstruct.2011.07.024>

Kato, S., Kim, Y. B., Nakazawa, S., & Ohya, T. (2005). Simulation of the cyclic behavior of J-shaped steel hysteresis devices and study on the efficiency for reducing earthquake responses of space structures. *Journal of Constructional Steel Research, 61*(10), 1457–1473. <https://doi.org/10.1016/j.jcsr.2005.03.006>

Kelly, J. M., Skinner, R. I., & Heine, A. J. (1972). Mechanisms of Energy Absorption in Special Devices for Use in Earthquake Resistant Structures. *Bulletin of the New Zealand Society for Earthquake Engineering, 5*(3), 63–73. <https://doi.org/10.5459/bnzsee.5.3.63-88>

KHATIB, I. F., MAHIN, S. A., & PISTER, K. S. (1988). SEISMIC BEHAVIOR OF

CONCENTRICALLY BRACED STEEL FRAMES. In *EARTHQUAKE ENGINEERING RESEARCH CENTER*. the National Technical Information Service, U.S.

Kovacs, M., & Wiebe, L. (2016). CONTROLLED ROCKING CROSS-LAMINATED TIMBER WALLS FOR REGIONS OF LOW-TO-MODERATE SEISMICITY. In *WCTE 2016*.

Lam, F., Gehloff, M., & Closen, M. (2010). Moment-resisting bolted timber connections. *Proceedings of the Institution of Civil Engineers: Structures and Buildings*, 163(4), 267–274. <https://doi.org/10.1680/stbu.2010.163.4.267>

Landolfo, R., Mazzolani, F. M., Dubina, D., da Silva, L. S., & d’Aniello, M. (2017). *Design of Steel Structures for Buildings in Seismic Areas: Eurocode 8: Design of Steel Structures in Seismic Areas. General Rules and Rules for Buildings*.

Li, H. N., & Li, G. (2007). Experimental study of structure with “dual function” metallic dampers. *Engineering Structures*, 29(8), 1917–1928. <https://doi.org/10.1016/j.engstruct.2006.10.007>

Lu, Y. (2004). Inelastic behaviour of RC wall-frame with a rocking wall and its analysis INCORPORATING 3-D EFFECT. *THE STRUCTURAL DESIGN OF TALL AND SPECIAL BUILDINGS*.

Ma, X. (2010). *Seismic Design and Behaviour of Self-Centering Braced Frame with Controlled Rocking and Energy-Dissipating Fuses*. Stanford University.

Ma, X., Borchers, E., Pena, A., Krawinkler, H., & Deierlein, G. (2010). Design and behavior of steel shear plates with openings as energy-dissipating fuses. *John A. Blume Earthquake*

Engineering Center Technical Report,(173).

Maleki, S., & Mahjoubi, S. (2013). Dual-pipe damper. *Journal of Constructional Steel Research*, 85, 81–91. <https://doi.org/10.1016/j.jcsr.2013.03.004>

Mashal, M., Palermo, A., & Keats, G. (2019). Innovative metallic dissipaters for earthquake protection of structural and non-structural components. *Soil Dynamics and Earthquake Engineering*, 116(September 2018), 31–42. <https://doi.org/10.1016/j.soildyn.2018.10.002>

McKenna, F., Scott, M. H., & Fenves, G. L. (2010). Nonlinear Finite-Element Analysis Software Architecture Using Object Composition. *Journal of Computing in Civil Engineering*, 24(1), 95–107. [https://doi.org/10.1061/\(asce\)cp.1943-5487.0000002](https://doi.org/10.1061/(asce)cp.1943-5487.0000002)

Moen, C. D., Igusa, T., & Schafer, B. W. (2008). Prediction of residual stresses and strains in cold-formed steel members. *Thin-Walled Structures*, 46(11), 1274–1289. <https://doi.org/10.1016/j.tws.2008.02.002>

Motamedi, M., & Nateghi-A., F. (2018). Study on mechanical characteristics of accordion metallic damper. *Journal of Constructional Steel Research*, 142, 68–77. <https://doi.org/10.1016/j.jcsr.2017.12.010>

Mottier, P., Tremblay, R., & Rogers, C. (2018). Seismic retrofit of low-rise steel buildings in Canada using rocking steel braced frames. *Earthquake Engineering & Structural Dynamics*, 47(2), 333–355.

Mottier, P., Wiebe, L., Steele, T., Tremblay, R., & Rogers, C. (2019). *Performance evaluation of gravity-controlled rocking braced frames for low-rise steel buildings.*

Mowafy, A., Imanpor, A., Chui, Y. H., & Daneshvar, H. (2023). Cyclic Behaviour and Plastic Mechanism of a U-shaped Steel Seismic Fuse. [Manuscript submitted for publication].

Engineering Structures.

Mowafy, A., Imanpour, A., & Chui, Y. H. (2021). Evaluation of the Seismic Response of an Innovative Hybrid Steel-Timber Structure. *Ce/Papers*, 4(2–4), 1864–1873.

<https://doi.org/10.1002/cepa.1497>

Multiphysics, C. (2015). The COMSOL Multiphysics Reference Manual. *Manual*, 1–1336.

www.comsol.com/blogs

Nakashima, M., Iwai, S., Iwata, M., Takeuchi, T., Konomi, S., Akazawa, T., & Saburi, K.

(1994). Energy dissipation behaviour of shear panels made of low yield steel. *Earthquake Engineering & Structural Dynamics*, 23(12), 1299–1313.

<https://doi.org/10.1002/eqe.4290231203>

National Research Council of Canada, [NRC]. (2010). *National Building Code of Canada (NBCC)*.

Newcombe, M. P., Pampanin, S., & Buchanan, A. H. (2010). Global response of a two storey Pres-Lam timber building. *New Zealand Society for Earthquake Engineering Conference*, 8(28), 8.

Ottenhaus, L. M., Jockwer, R., van Drimmelen, D., & Crews, K. (2021). Designing timber connections for ductility – A review and discussion. *Construction and Building Materials*, 304(August), 124621. <https://doi.org/10.1016/j.conbuildmat.2021.124621>

- Pampanin, S. (2012). Reality-check and renewed challenges in earthquake engineering: Implementing low-damage systems - From theory to practice. *Bulletin of the New Zealand Society for Earthquake Engineering*, 45(4), 137–160.
<https://doi.org/10.5459/bnzsee.45.4.137-160>
- Pampanin, S., Kam, W. Y., Tasligedik, A. S., Quintana-Gallo, P., & Akguzel, U. (2011). Considerations on the seismic performance of pre-1970s RC buildings in the Christchurch CBD during the 4th Sept 2010 Canterbury earthquake: was that really a big one? *Proceedings of the Ninth Pacific Conference on Earthquake Engineering-Building an Earthquake-Resilient Society, March 2015*.
- Panagiotou, M., & Jos'e I. Restrepo. (2007). Dual-plastic hinge design concept for reducing higher-mode effects on high-rise cantilever wall buildings. *Pacific Conference on Earthquake Engineering*, 056, 1–6. <https://doi.org/10.1002/eqe>
- Paul, S., Murty, C., & Jain, S. K. (2000). State-of-the-art Review of Seismic Design of Steel Moment Resisting Frames—Part I: General Considerations and Stability Provisions. *Journal of Structural Engineering*, 27(1), 23–32.
- Pollino, M. (2015). Seismic design for enhanced building performance using rocking steel braced frames. *Engineering Structures*, 83, 129–139.
- Pollino, M., & Bruneau, M. (2004). Controlled Rocking System for Seismic Retrofit of Steel Truss Bridge Piers. In *Technical Rep.MCEER-04-0011*.
- Popov, E. P., & Engelhardt, M. D. (1988). Seismic eccentrically braced frames. *Journal of Constructional Steel Research*, 10, 321–354.

- Popovski, M., & Gavric, I. (2016). Performance of a 2-Story CLT House Subjected to Lateral Loads. *Journal of Structural Engineering*, 142(4). [https://doi.org/10.1061/\(ASCE\)ST.1943-541X.0001315](https://doi.org/10.1061/(ASCE)ST.1943-541X.0001315)
- Priestley, M. J. N. (1996). The PRESSS program - Current status and proposed plans for Phase III. *PCI Journal*, 41(2), 22–40. <https://doi.org/10.15554/pcij.03011996.22.40>
- Qu, B., Dai, C., Qiu, J., Hou, H., & Qiu, C. (2019). Testing of seismic dampers with replaceable U-shaped steel plates. *Engineering Structures*, 179(August 2018), 625–639. <https://doi.org/10.1016/j.engstruct.2018.11.016>
- Roke, D., Sause, R., Ricles, J. M., & Gonner, N. (2009a). Damage-free seismic-resistant self-centering steel concentrically-braced frames. *Stessa 2009 – Mazzolani, Ricles & Sause (Eds)*, 3–10.
- Roke, D., Sause, R., Ricles, J. M., & Gonner, N. (2009b). Design concepts for damage-free seismic-resistant self-centering steel concentrically braced frames. *Structures Congress 2009: Don't Mess with Structural Engineers: Expanding Our Role*, 1–10.
- Rothoblaas. (2022). *Full threaded screw with cylindrical head*.
- RothoBlass. (2022a). *SBD-Technical data sheet* (p. 6).
- RothoBlass. (2022b). *Technical Data Sheet for Self-drilling dowels*. <https://www.rothoblaas.com/products/fastening/screws/screws-structures/sbd>
- Sarti, F., Palermo, A., & Pampanin, S. (2014). Quasi static cyclic tests of 2 / 3 scale post-tensioned timber wall and column-wall-column (CWC) systems. *Bulletin of the New*

Zealand Society for Earthquake Engineering, NZSEE, 1–9.

Sause, R., Ricles, J. M., Roke, D. ., Chancellor, N. ., & Gonner, N. P. (2010). SEISMIC PERFORMANCE OF A SELF-CENTERING ROCKING CONCENTRICALLY-BRACED FRAME. *The 9th U.S. National and 10th Canadian Conference on Earthquake Engineering, 1827, 1–10.*

Sirumbal-Zapata, L. F., Málaga-Chuquitaype, C., & Elghazouli, A. Y. (2019). Experimental assessment and damage modelling of hybrid timber beam-to-steel column connections under cyclic loads. *Engineering Structures, 200*(August), 109682.
<https://doi.org/10.1016/j.engstruct.2019.109682>

Smith, I., Asiz, A., Snow, M., & Chui, Y. . (2006). Possible Canadian/ISO Approach to Deriving Design Values from Test Data. *The CIB-W18 Meeting.*

Structural Commentaries. (2015). *NRC-Commentaries, User's Guide – NBC 2015.*

Suzuki, K., Watanabe, A., & Saeki, E. (2005). Development of U-shaped steel damper for seismic isolation system. *Nippon Steel Technical Report, 92, 56–61.*

Taiyari, F., Mazzolani, F. M., & Bagheri, S. (2019). A proposal for energy dissipative braces with U-shaped steel strips. *Journal of Constructional Steel Research, 154, 110–122.*
<https://doi.org/10.1016/j.jcsr.2018.11.031>

Tasi, K.-C., EERI, M., Hong, C.-P., & Su, Y.-F. (1993). Design of steel triangular plate energy absorbers for seismic-resistant construction. *Earthquake Spectra.*

Ted Belytschko, Liu, W. K., Moran, B., & Elkhodary, K. (2014). *Nonlinear Finite Elements for*

Continua and Structures Second Edition (Issue 1). Wiley Online Library.

<https://www.wiley.com/en->

[us/Nonlinear+Finite+Elements+for+Continua+and+Structures%2C+2nd+Edition-p-](https://www.wiley.com/en-us/Nonlinear+Finite+Elements+for+Continua+and+Structures%2C+2nd+Edition-p-9781118632703)

[9781118632703](https://www.wiley.com/en-us/Nonlinear+Finite+Elements+for+Continua+and+Structures%2C+2nd+Edition-p-9781118632703)

Tesfamariam, S., Stiemer, S. F., Dickof, C., & Bezabeh, M. A. (2014a). Seismic vulnerability assessment of hybrid Steel-Timber structure: Steel moment-Resisting frames with clt infill. *Journal of Earthquake Engineering*, *18*(6), 929–944.
<https://doi.org/10.1080/13632469.2014.916240>

Tesfamariam, S., Stiemer, S. F., Dickof, C., & Bezabeh, M. A. (2014b). Seismic Vulnerability Assessment of Hybrid Steel-Timber Structure: Steel Moment-Resisting Frames with CLT Infill. *Journal of Earthquake Engineering*, *18*(6), 929–944.
<https://doi.org/10.1080/13632469.2014.916240>

Tremblay, R. (2001). Seismic behavior and design of concentrically braced steel frames. *Engineering Journal*, *38*(3), 148–160.

Tremblay, R., Poirier, L., Bouaanani, N., Leclerc, M., Rene, V., Fronteddu, L., & Rivest, S. (2008). Innovative viscously damped rocking braced steel frames. *The 14th World Conference on Earthquake Engineering*, 12–17.

Uang, C.-M., & Bruneau, M. (2018). State-of-the-Art Review on Seismic Design of Steel Structures. *Journal of Structural Engineering*, *144*(4), 3118002.
[https://doi.org/10.1061/\(ASCE\)ST.1943-541X.0001973](https://doi.org/10.1061/(ASCE)ST.1943-541X.0001973)

Verna, J. R., Graham, J. F., Shannon, J. M., & Sanders, P. H. (1984). Timber Bridges: Benefits

- and Costs. *Journal of Structural Engineering*, 110(7), 1563–1571.
[https://doi.org/10.1061/\(ASCE\)0733-9445\(1984\)110:7\(1563\)](https://doi.org/10.1061/(ASCE)0733-9445(1984)110:7(1563))
- Wang, M., Song, X., Gu, X., Zhang, Y., & Luo, L. (2015). Rotational Behavior of Bolted Beam-to-Column Connections with Locally Cross-Laminated Glulam. *Journal of Structural Engineering*, 141(4), 1–7. [https://doi.org/10.1061/\(asce\)st.1943-541x.0001035](https://doi.org/10.1061/(asce)st.1943-541x.0001035)
- Wiebe, L., & Christopoulos, C. (2009). Mitigation of higher mode effects in base-rocking systems by using multiple rocking sections. *Journal of Earthquake Engineering*, 13(S1), 83–108.
- Wiebe, L., & Christopoulos, C. (2015a). Performance-Based Seismic Design of Controlled Rocking Steel Braced Frames. I: Methodological Framework and Design of Base Rocking Joint. *Journal of Structural Engineering*, 141(9), 1–11.
[https://doi.org/10.1061/\(asce\)st.1943-541x.0001202](https://doi.org/10.1061/(asce)st.1943-541x.0001202)
- Wiebe, L., & Christopoulos, C. (2015b). Performance-Based Seismic Design of Controlled Rocking Steel Braced Frames. II: Design of Capacity-Protected Elements. *Journal of Structural Engineering*, 141(9), 1–11. [https://doi.org/10.1061/\(asce\)st.1943-541x.0001201](https://doi.org/10.1061/(asce)st.1943-541x.0001201)
- Wiebe, L., Christopoulos, C., Tremblay, R., & Leclerc, M. (2012). Mechanisms to limit higher mode effects in a controlled rocking steel frame. 1: Concept, modelling, and low-amplitude shake table testing. *Pacific Conference on Earthquake Engineering*, 056, 1–6.
<https://doi.org/10.1002/eqe>
- Xie, Q. (2005). State of the art of buckling-restrained braces in Asia. *Journal of Constructional Steel Research*, 61(6), 727–748.

- Xinxian, Z., Xiaolei, H., Jing, J., Yongle, Q., & Chao, H. (2016). Component-level Performance-based Seismic Assessment and Design Approach for Concrete Moment Frames. *The Open Civil Engineering Journal*, 10(1), 25–39. <https://doi.org/10.2174/1874149501610010025>
- Yang, H., Liu, W., & Ren, X. (2016). A component method for moment-resistant glulam beam-column connections with glued-in steel rods. *Engineering Structures*, 115, 42–54. <https://doi.org/10.1016/j.engstruct.2016.02.024>
- Yousef Bozorgnia, & Vitelmo V. Bertero. (2004). *Earthquake Engineering From Engineering Seismology to Performance-Based Engineering* (1st Edition (ed.)).
- Zhang, X., Fairhurst, M., & Tannert, T. (2016). Ductility Estimation for a Novel Timber–Steel Hybrid System. *Journal of Structural Engineering*, 142(4). [https://doi.org/10.1061/\(ASCE\)ST.1943-541X.0001296](https://doi.org/10.1061/(ASCE)ST.1943-541X.0001296)
- Zhang, X., Popovski, M., & Tannert, T. (2018). High-capacity hold-down for mass-timber buildings. *Construction and Building Materials*, 164, 688–703. <https://doi.org/10.1016/j.conbuildmat.2018.01.019>
- Zhang, Y., Fung, J. F., Johnson, K. J., & Sattar, S. (2022). Review of Seismic Risk Mitigation Policies in Earthquake-Prone Countries: Lessons for Earthquake Resilience in the United States. *Journal of Earthquake Engineering*, 26(12), 6208–6235. <https://doi.org/10.1080/13632469.2021.1911889>
- Zhong, C., & Christopoulos, C. (2022). Self-centering seismic-resistant structures: Historical overview and state-of-the-art. *Earthquake Spectra*, 38(2), 1321–1356. <https://doi.org/10.1177/87552930211057581>

Appendices

Appendix A – Coupon Test

Eight coupon standard ASTM E8 specimens were taken from the blank flat plates used in the bending process with two specimens per thickness (Figure A1a). The results of the tests are shown in Table A1, and Figure A1.b illustrates the failure shapes of the coupons. Figure A1.c illustrates that the yielding stress is always higher than the nominal stress of the material, but it did not go beyond a 20% increase from the nominal one. Figure A1.d shows the engineering and actual stress-strain curve of specimen 1. The results would be used to define the material parameters and develop kinematic hardening parameters in the finite element model.

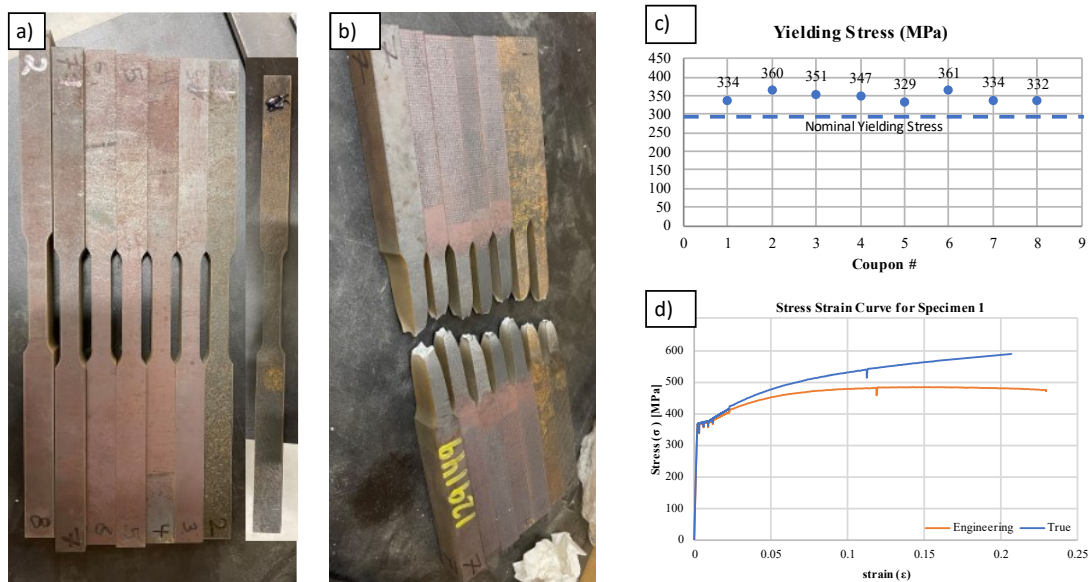


Figure A1. a) Coupons Specimens; b) Coupons failure shape; c) Yielding Stress for each specimen; d) Sample stress-strain curve for specimen 1.

Table A1 Coupon Tensile Test results

Coupon	Thickness (in)	Yield Stress (MPa)	Tensile Stress (MPa)	Young's Modulus (GPa)
1	0.5	334	587	180
2	0.5	360	602	180
3	5/8	351	578	202
4	5/8	347	571	197
5	0.75	329	590	203
6	0.75	361	588	203
7	7/8	334	604	184
8	7/8	332	617	195

Appendix B – U-shaped Fuses Bending Process

Since the U-shaped plates were thick, a custom bender with a Triple-shaft system was manufactured (Figure B1). The plate was positioned on the two stationary shafts, and the central one applied the load through a jack (Figure B2b). The blank profile (Figure B2a) deforms gradually into a V shape and then is extruded as a U shape (Figure B2d) from the open end of the machine. The bending load applied was 250 to 700 kN, and no heat treatment was applied.

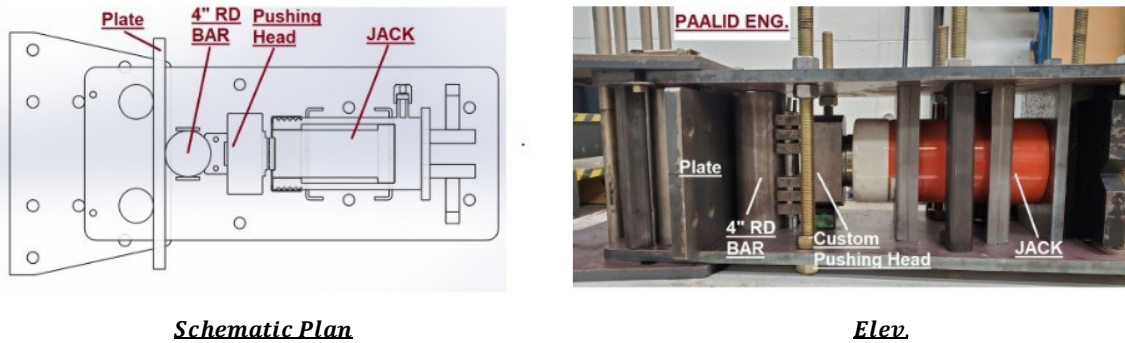


Figure B1. Custom Developed Bender

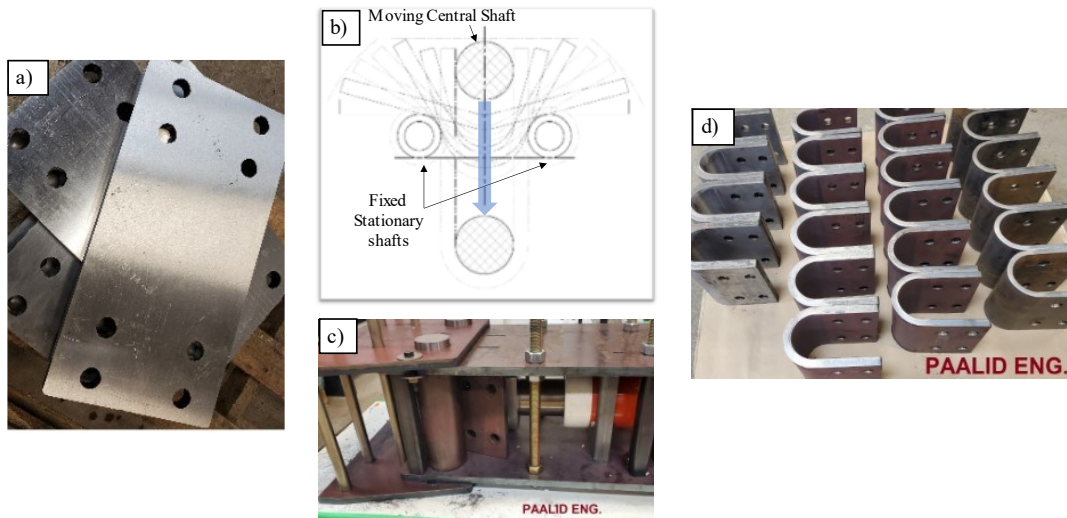


Figure B2. Bending Process: a) Blank Profile; b) Bending Mechanism; c) Plate during Bending; d) Final Product.

Appendix C – Self Drilling Dowels Installation

One of the primary objectives of the proposed connection is to facilitate the easy replacement of fuses after a seismic event. To achieve this, self-drilling dowels and T-end plate connectors were installed in a workshop of InnoTech Alberta to simplify the installation process and eliminate alignment issues on site. A temporary guided end plate was used to ensure proper alignment with the fuse bolt location for on-site installation (Figure C2a). Installing self-drilling dowels with hand drills can be challenging and may damage the dowel's self-perforating tip (Figure C2b). As a solution, it is recommended to use a radio pressing machine for installation, as shown in Figure C2c. This method allows for better control of the insertion depth rate and prevents dowel damage. Predrilled holes were made before using the machine, and the self-drilling dowels were partially installed until they touched the first knife plate to ensure proper perpendicular direction (Figure C2d).

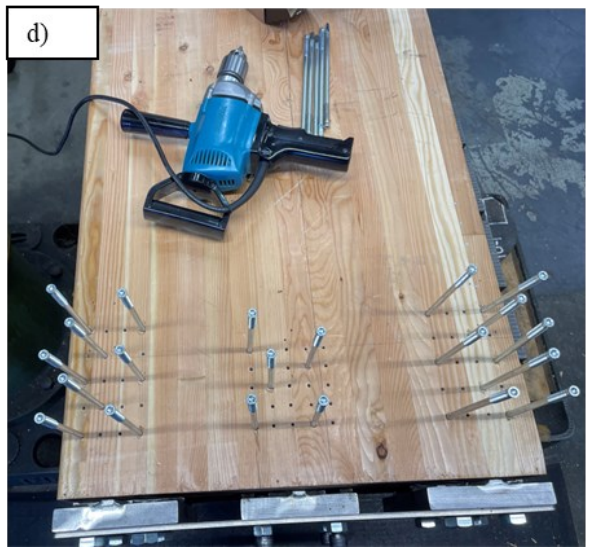
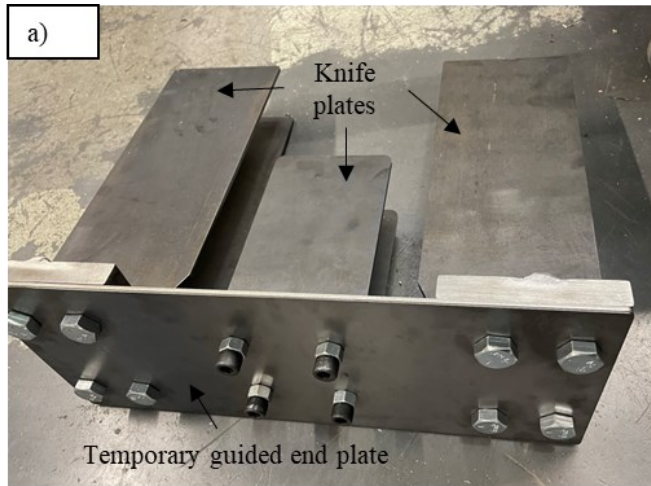


Figure C2. SDDs installation Process: a) Temporary Guided plate; b) Damage in the SDD self-perforating tip; c) Radio Pressing Machine at InnoTech Alberta; d) partially installation of the SDDs.

Appendix D – Structural Drawings of The Glulam Beam Specimens

Figures D1-D4 display the detailed dimensions of Glulam beams 1-4 highlighting the distribution of Self-Drilling Dowels used in the connection testing.

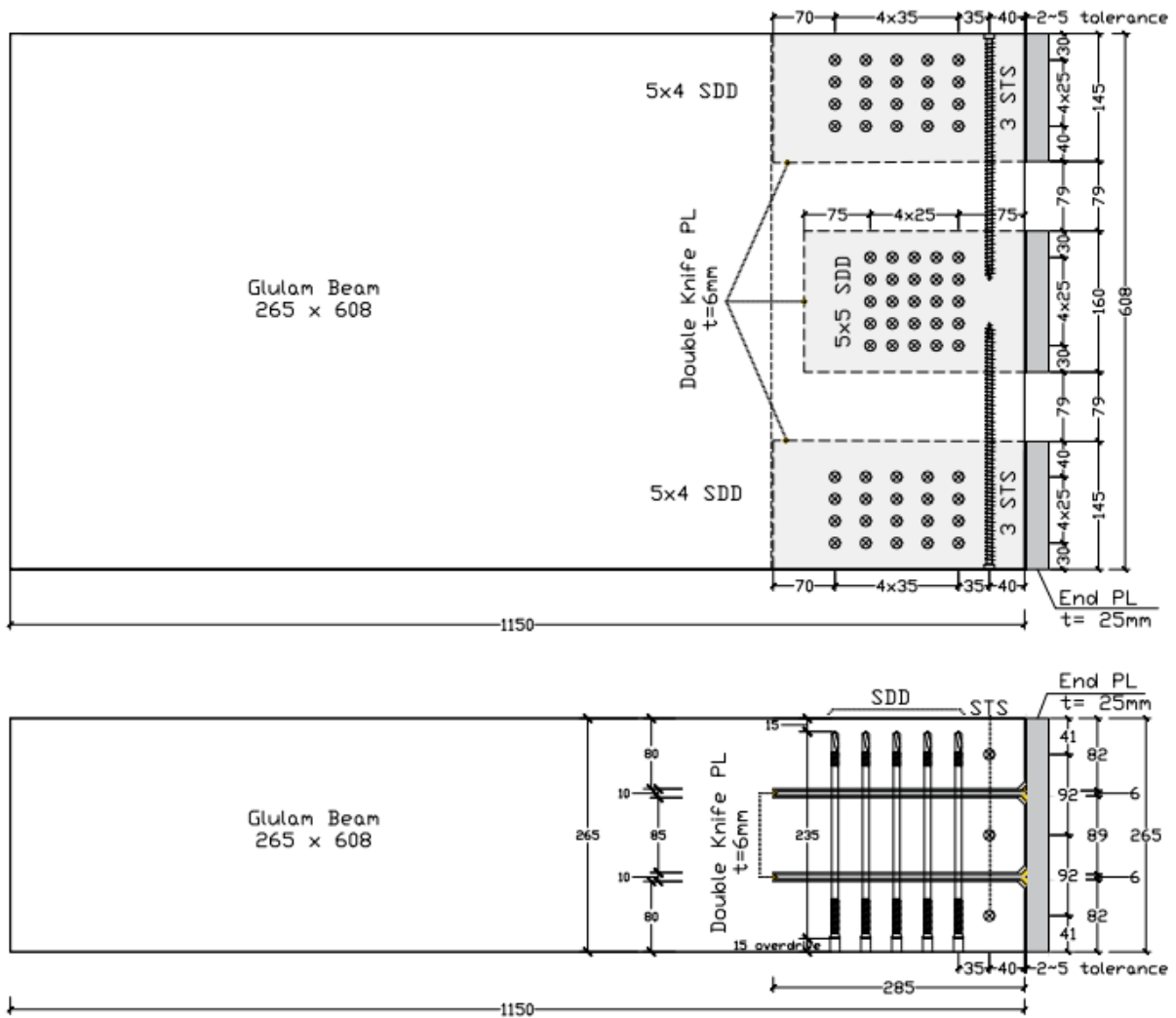


Figure D1. Glulam Beam 1 Specimen Dimensions

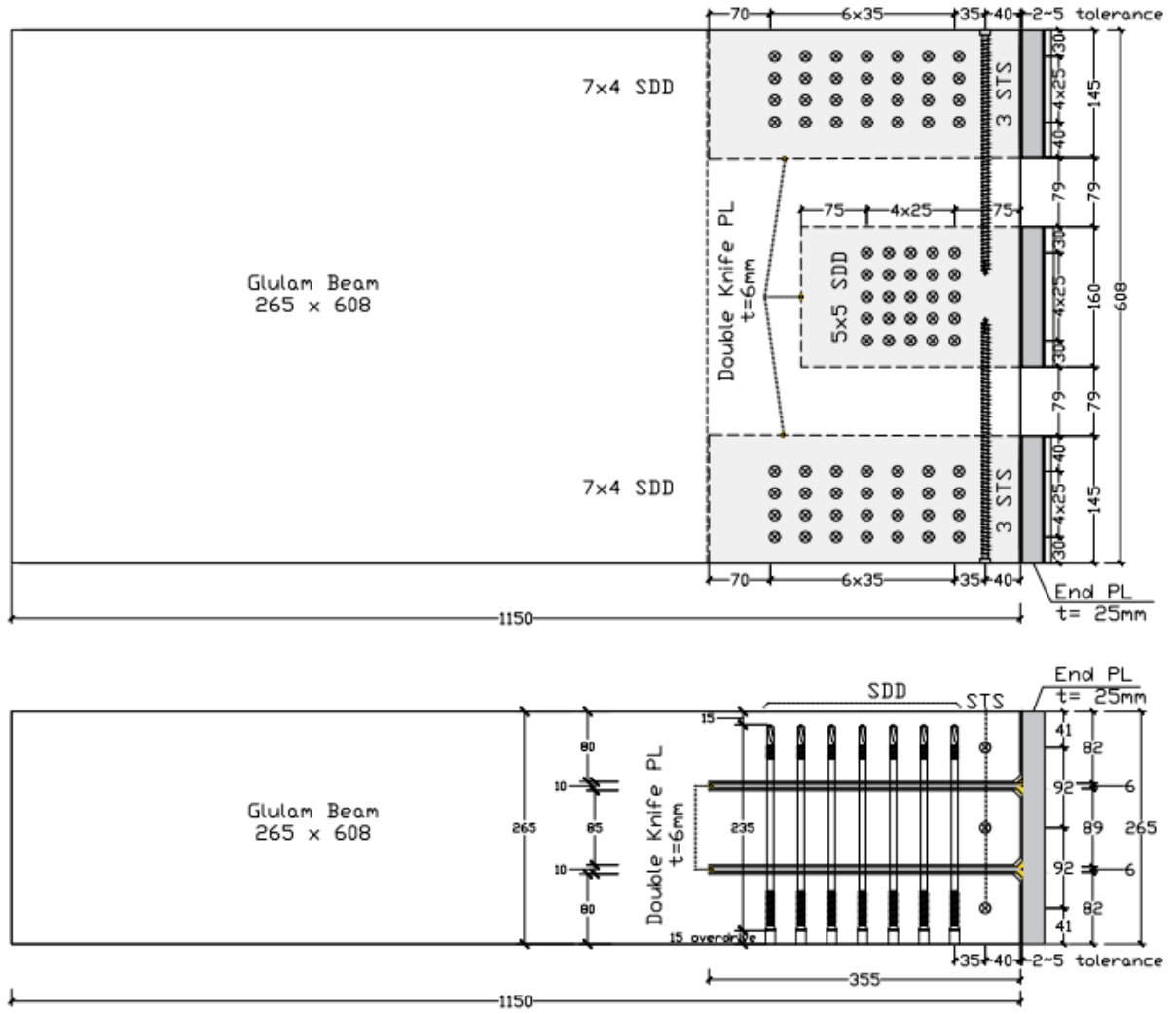


Figure D2. Glulam Beam 2 Specimen Dimensions

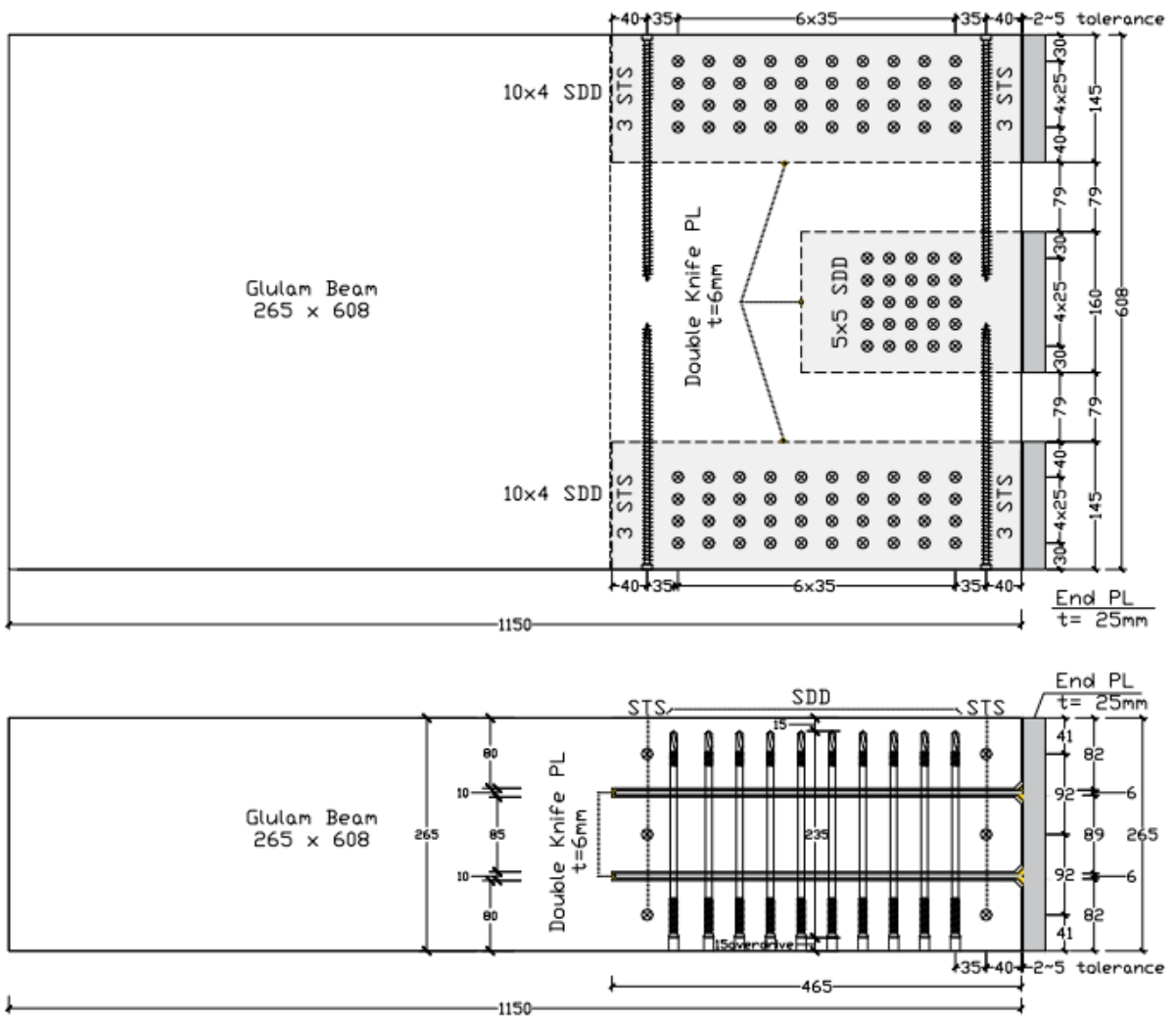


Figure D3. Glulam Beam 3 Specimen Dimensions

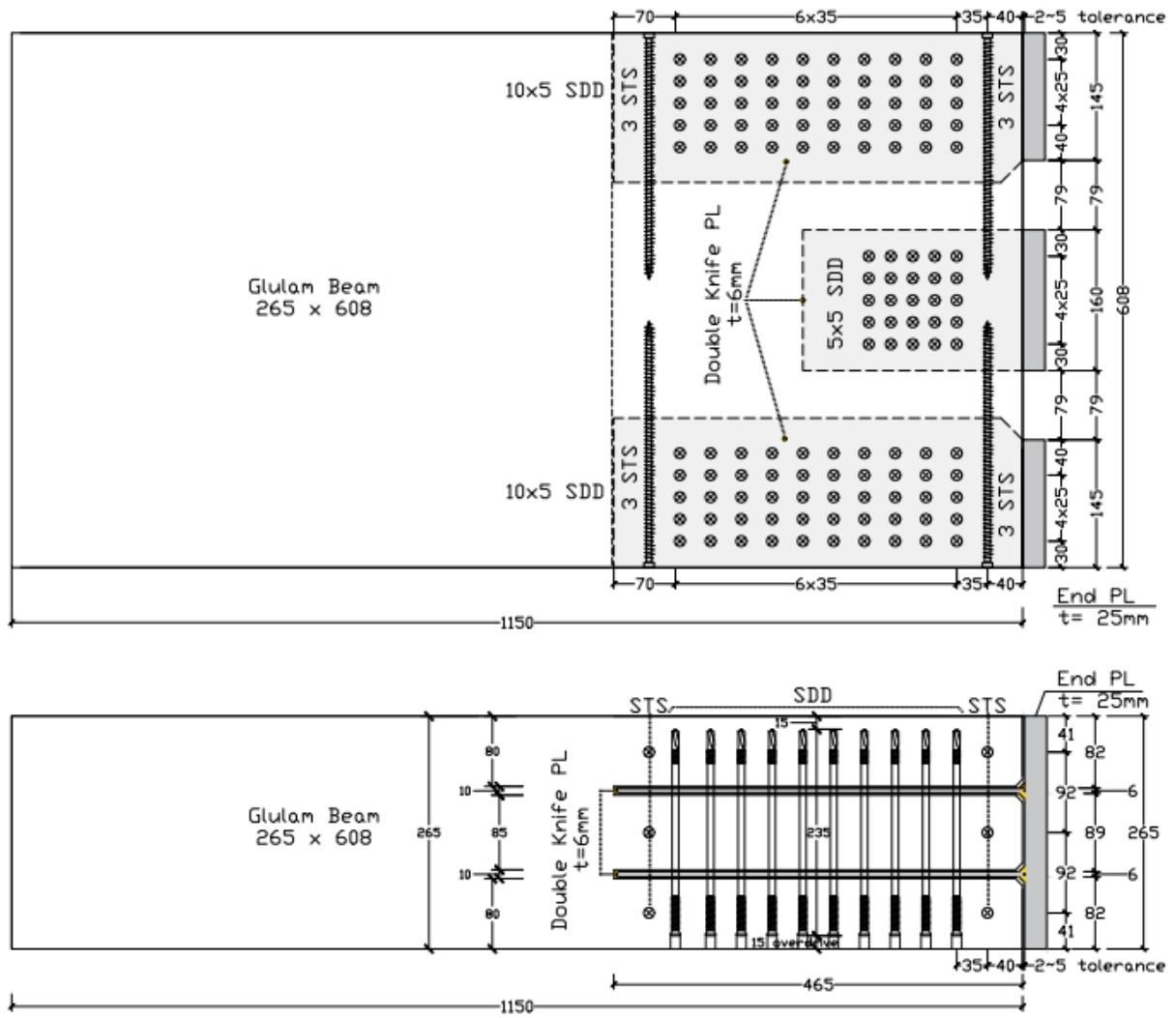


Figure D4. Glulam Beam 4 Specimen Dimensions